The Dissertation Committee for Wenyuan Li
certifies that this is the approved version of the following dissertation:

PHASE-FIELD MODELING OF PIEZOELECTRICS AND INSTABILITIES IN DIELECTRIC ELASTOMER COMPOSITES

Committee:

Chad M. Landis, Supervisor

Rui Huang

Mark Mear

K. Ravi-Chandar

John L. Tassoulas

PHASE-FIELD MODELING OF PIEZOELECTRICS AND INSTABILITIES IN DIELECTRIC ELASTOMER COMPOSITES

by

Wenyuan Li, B.S.; M.S.

Dissertation

Presented to the Faculty of the Graduate School of

The University of Texas at Austin

in Partial Fulfillment

of the Requirements

for the Degree of

Doctor of Philosophy

The University of Texas at Austin

December 2011

DEDICATED

TO THE MEMORY OF

HUANG XIANHUI

AND TO MY FAMILY

ACKNOWLEDGEMENTS

First and foremost I would like to present my sincere appreciation to my advisor Dr. Chad M. Landis for his invaluable guidance, insightful advice and patient encouragement during my graduate program all these years. His broad and in-depth knowledge and his enthusiasm in research have inspired me and broadened my vision. Also, he is an excellent life model for someone who knows how to balance research, teaching and family. It has been an incredible journey learning from and working with him. I am grateful for his time, effort and care greatly.

The members of my dissertation committee, Dr. Rui Huang, Dr. Mark Mear, Dr. K. Ravi-Chandar, and Dr. John L. Tassoulas have generously given their name and expertise to better my work. I truly appreciate their contribution and kind support.

A special thanks to all of my colleagues, especially Yong Zhu, Dorina Maria Carka, Suk-Kyu Ryu, Seung Ryul Na, Qinqin Li, Haixia Mei, Rong Jiao and Kaimin Yue, who provided me with technical advice and friendship throughout my studies.

My time at University of Texas was made enjoyable in large part due to the many friends that became a part of my life. I wish to acknowledge some of them: Shengyuan Yang, Xinran Li, Yiyi Chu, Ligang Long, Ling Huang, Zhan Shi, Fei Yan, Yumin Li, Mingfeng Wu, Changhai Xu.

Finally, I would like to express my deepest gratitude to my family for all their love and encouragement. To my parents LiYuqiang and CaoJiling who raised me with the best and the most they could and supported me in all my pursuits. To my husband Jun Shen for being always with me and for his profound understanding. To my younger sister LvLina and younger brother LiHao for their consistent love and support.

PHASE-FIELD MODELING OF PIEZOELECTRICS AND INSTABILITIES IN DIELECTRIC ELASTOMER COMPOSITES

Wenyuan Li, Ph.D.

The University of Texas at Austin, 2011

Supervisor: Chad M. Landis

Ferroelectric ceramics are broadly used in applications including actuators, sensors and information storage. An understanding of the microstructual evolution and domain dynamics is vital for predicting the performance and reliability of such devices. The underlying mechanism responsible for ferroelectric constitutive response is ferroelectric domain wall motion, domain switching and the interactions of domain walls with other material defects.

In this work, a combined theoretical and numerical modeling framework is developed to investigate the nucleation and growth of domains in a single crystal of ferroelectric material. The phase-field approach, applying the material electrical polarization as the order parameter, is used as the theoretical modeling framework to allow for a detailed accounting of the electromechanical processes. The finite element method is used for the numerical solution technique. In order to obtain a better understanding of the energetics of fracture within the phase-field setting, the J-integral is modified to include the energies associated with the order parameter. Also, the J-integral is applied to determine the crack-tip energy release rate for common sets of electromechanical crack-face boundary conditions. The calculations confirm that only true equilibrium states exhibit path-independence of J, and that domain structures near

crack tips may be responsible for allowing positive energy release rate during purely electrical loading.

The small deformation assumption is prevalent in the phase-field modeling approach, and is used in the previously described calculations. The analysis of large deformations will introduce the concept of Maxwell stresses, which are assumed to be higher order effects that can be neglected in the small deformation theory. However, in order to investigate the material response of soft dielectric elastomers undergoing large mechanical deformation and electric field, which are employed in electrically driven actuator devices, manipulators and energy harvesters, a finite deformation theory is incorporated in the phase-field model. To describe the material free energy, compressible Neo-Hookean and Gent models are used. The Jaumann rate of the polarization is used as the objective polarization rate to make the description of the dissipation frame indifferent. To illustrate the theory, electromechanical instabilities in composite materials with different inclusions will be studied using the finite element methods.

Table of Contents

List of Figures

xvii

Chapter I   Introduction

Ferroelectric materials are used in a broad range of applications due to their extraordinary dielectric properties and strong electro-mechanical coupling performance. The main applications of ferroelectric ceramics have been for capacitors; ferroelectric thin films for nonvolatile memories, pyroelectric sensors, surface acoustic wave substrates; and piezoelectric ceramics for medical ultrasound applications. Ferroelectric materials can be categorized into (Kaltenbacher et al., 2011): single crystals; ferroelectric ceramics, such as barium titanate ($BaTiO_3$) and lead zirconate titanate (PZT); and polymers, such as polyvinylidenfluoride (PVDF). The piezoelectric effects in quartz and polymers are normally weak in comparison with perovskite structural ferroelectrics, which are often used in sensor applications. Ferroelectric ceramics has strong electromechanical coupling performance that is used in actuator applications. For further development of the micro ferroelectric device technology and improvement of their performance and reliability, a fundamental understanding of the mechanics and physics governing the ferroelectric materials response is vital.

In general there are four distinct size scales existing in a ferroelectric ceramic: atomic, domain, grain and polycrystal. At the smallest scale, the atomic or lattice scale, essentially no phenomenological assumptions need to be made and electronic structure calculations have been applied to predict the properties of ferroelectric material (Cohen and Krakauer, 1992; Belliache et al., 2000). Single crystal grains contain many domains and are generally larger than one micron, and polycrystals contain many grains and are usually hundreds of microns or larger. At the single crystal grain and polycrystal size scales, phenomenological models dominate the constitutive descriptions (Hwang et al., 1995 and 1998; Chen and Lynch, 1998; Chan and Hagood, 1994; Kamlah and

1

Tsakmakis, 1999; Kamlah and Jiang, 1999; Huber et al., 1999; Landis 2002a and 2003), and the effect of domain switching is accounted for in an averaged sense. Between these scales, to simulate the microstructural evolution and domain dynamics, two models of domain evolution are usually used: sharp interface models and diffuse interface models. The diffuse interface approach is also called the phase-field modeling approach, which allows for a detailed accounting of the electromechanical processes that occur during domain nucleation and growth.

In this dissertation, the phase-field modeling approach is applied to investigate the nucleation and growth of domains in a single crystal of ferroelectric material. In order to obtain a better understanding of the energetics of fracture within the phase-field setting, we propose a modified J-integral form to include the energies associated with the polarization order parameter, and also demonstrate how the J-integral can be applied to determine the crack-tip energy release rate for common sets of electromechanical crack-face boundary conditions.

The small deformation assumption is prevalent in the phase-field modeling approach. The analysis of large deformations will introduce the concept of Maxwell stresses, which are assumed to be higher order effects that are often neglected. However, in order to investigate the material response of soft dielectric elastomers undergoing large mechanical deformations, which are widely employed to manufacture devices as electrically driven actuators, manipulators and energy harvesters, the finite deformation theory will be incorporated in the phase-field model. First we develop finite deformation phase-field theory, and then we investigate the instabilities in dielectric elastomer composites.

Some background and features of ferroelectric materials will be introduced in the next sections, and then the outline of this dissertation will be listed.

2

1.1 BACKGROUND

Ferroelectrics are the materials which possess a spontaneous electric polarization which can be reversed in direction or reoriented by applying an external electric field that is larger than the coercive field. This process is known as "switching", and is accompanied by hysteresis. This behavior is mainly observed below the transition temperature or Curie point, and above this critical point the material will show normal dielectric/paraelectric behavior. The name "ferroelectrics" is due to a formal analogy between ferroelectric phenomenon and ferromagnetism, however, there is no iron in ferroelectrics as the prefix "ferro-" might seem to imply. The phenomenological similarity is, ferroelectric materials show a spontaneous electric polarization and hysteresis effects in the relation between electric polarization and electric field, just as ferromagnetic materials exhibit a spontaneous magnetization and hysteresis in the relationship between magnetization and magnetic field. Ferroelectric materials have properties that are an indirect consequence of ferroelectricity, such as piezoelectric and pyroelectric properties.

In 1824, Brewster observed the pyroelectric effect from various kinds of crystals. Pyroelectric crystals show a spontaneous polarization in a certain temperature range. The value of the spontaneous polarization depends on the temperature, and this phenomenon is called the pyroelectric effect. All single crystals and successfully poled ceramics which show ferroelectric behavior are pyroelectric, but not necessarily vice versa.

In 1880, Pierre and Jacques Curie discovered the piezoelectric effect by showing that Rochelle salt crystals demonstrate electric polarization when mechanically compressed and change shape when an electric field is applied. The name "piezoelectricity" was proposed by Hankel. Piezoelectricity is a linear interaction

between mechanical and electrical behaviors. The direct piezoelectric effect is where electric polarization is produced by mechanical stress, and the converse effect is when mechanical strain is generated by the application of a voltage. The direct piezoelectric effect is used to make sensors, and the converse piezoelectric effect is used for actuation.

In 1921, ferroelectricity was first discovered by Joseph Valsek in the investigation of the Rochelle salt. Seignette or Rochelle Salt was the first material found to show ferroelectric properties such as a spontaneous electric polarization, ferroelectric domains and a ferroelectric hysteresis loop (Valasek, 1921). The spontaneous electric polarization is defined by the value of the dipole moment per unit volume or by the value of the charge per unit area on the surface perpendicular to the axis of polarization. Ferroelectric materials are piezoelectric and have an intrinsic dipole moment or remanent polarization (Jona and Shirane, 1962; Lines and Glass, 1977).

In the 1950's, a large amount of research was done on ferroelectric materials, leading to a widespread use of barium titanate ($BaTiO_3$) based ceramics in capacitor and transducer devices. Since then, many other ferroelectric ceramics including lead titanate ($PbTiO_3$), lead zirconate titanate (PZT) and lead lanthanum zirconate titanate (PLZT) have been developed and utilized for a variety of applications (Buchanan, 1986).

1.2 FEATURES OF FERROELECTRICITY

Perovskite ceramics, such as lead and barium titanate, exhibit ferroelectricity below a Curie temperature T_c. Above this critical temperature, the material has a cubic structure and is paraelectric, while below T_c the structure is tetragonal and the material is ferroelectric. The chemistry of a material can be manipulated such that other structures, e.g. rhombohedral or orthorhombic, may also be present. To better

4

understand the material properties of ferroelectrics, such as remanent electric polarization, piezoelectricity, ferroelectricity, and ferroelasticity, a simplified and exaggerated schematic of the microscopic crystal structure of barium titanate is illustrated in Figure 1.2.1.
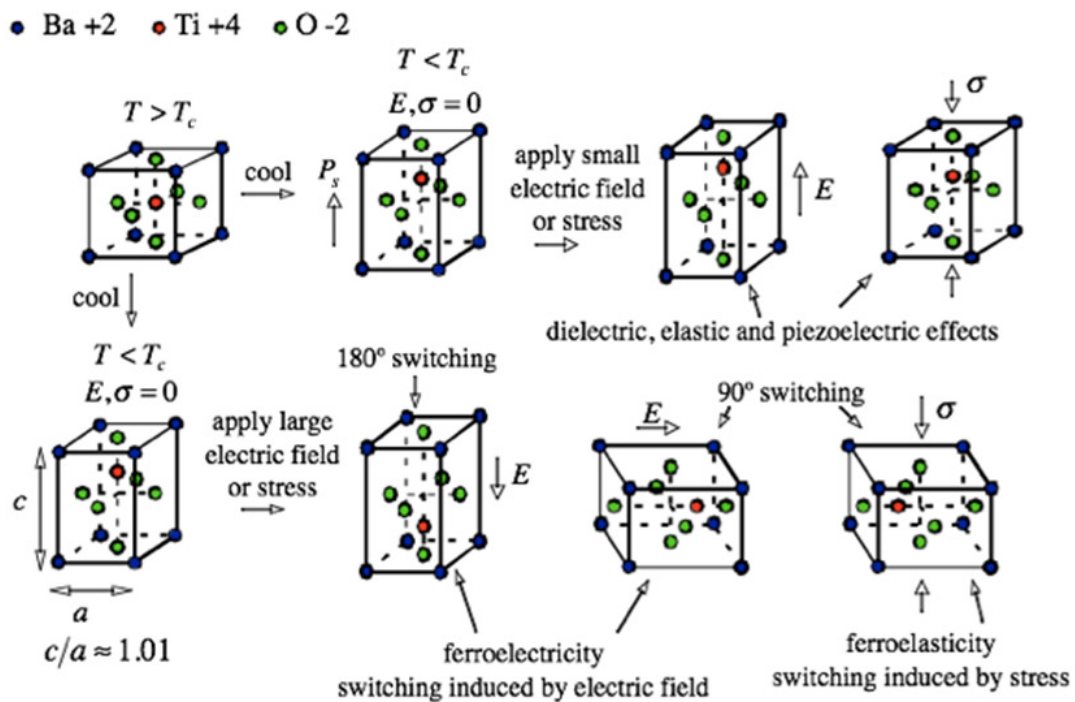
Figure 1.2.1: A simplified schematic of the crystal structure of barium titanate is illustrated above. The crystal illustrations include lead or barium ions (+2,blue), oxygen ions (-2, green), and a titanium ion (+4, red). As in other ferroelectric materials, this material demonstrates interesting physical behaviors including temperature, stress and electric field induced phase transitions, pyroelectricity, and domain switching. (Adapted from Landis: http://www.ae.utexas.edu/~landis/Landis/Research.html)

As shown in the figure, when the temperature is higher than the Curie point, the unit cell is cubic. The positively charged titanium ion (Ti, +4) is in the center of the cell, eight positively charged barium ions (Ba, +2) are at the cube corners, and six

negatively charged oxygen ions (O, -2) are in the center of the cube faces. In this cubic state, the center of the positive charges and negative charges coincide with each other, such that the unit cell possesses no polarization. In this state called the paraelectric phase, no ferroelectricity exists in the material. When the material is cooled down below the Curie temperature T_c, the cubic configuration becomes unstable, and the crystal undergoes a phase transition from the paraelectric phase to a ferroelectric phase, and the unit cell changes from high symmetry to a lower symmetry. For a tetragonal cell the central ion is displaced parallel to one of the edges, such that the titanium ion will shift away from the center of the unit cell. The positions of the centers of the positive and negative charges no longer overlap, which leads to a polarization dipole. Now the unit cell possesses spontaneous polarization, and consequently piezoelectric properties.

When a relatively small electric field is applied to the unit cell with spontaneous electric polarization, the ions tend to move along with the electric field, which changes the relative position of the centers of positive charges and negative charges. The movement gives rise to the change of electric polarization, and this is cause of the dielectric effect in ferroelectric materials. At the same time, when the ions change their position, the unit cell is elongated or shortened, which leads to mechanical strain. This is called the converse piezoelectric effect. Similarly, when a small stress is applied, the unit cell is elongated or shortened, which changes the relative positions of the centers of positively and negatively charged ions, giving rise to the change of the electric polarization. This effect is called the direct piezoelectric effect. Finally the geometric change of the unit cell induced by the stress field is observed as mechanical strain, and this effect is the elastic material response.
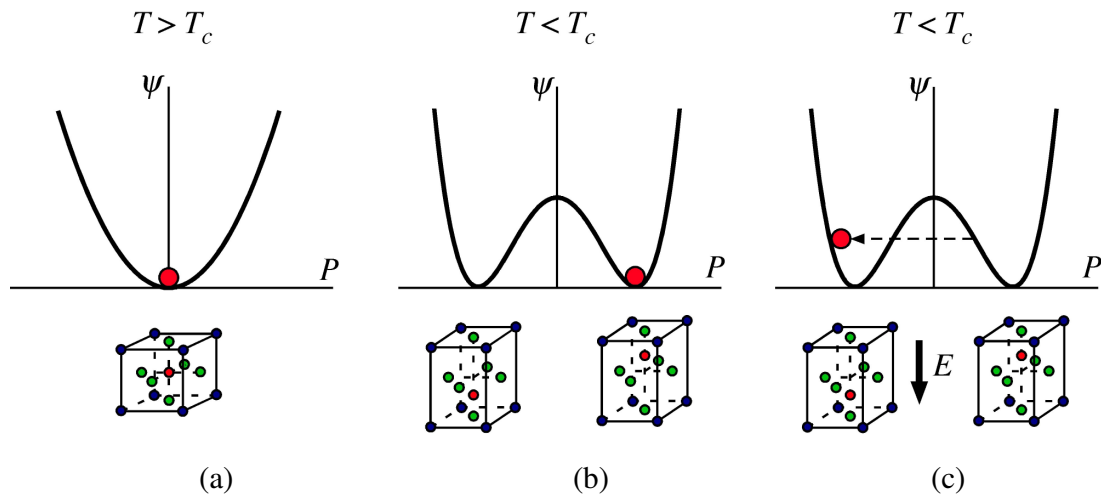
Figure 1.2.2:   The perovskite crystal structure of lead or barium titanate and a schematic of the free energy of the material associated with the high temperature cubic phase (a) and the low temperature tetragonal phase (b) and (c).   The crystal illustrations include lead or barium ions (+2, blue), oxygen ions (-2, green), and a titanium ion (+4, red).   (a) Above the Curie temperature T_c the material resides in the cubic phase and the material free energy ψ is convex with a single well at zero polarization.   (b) Below T_c a cubic to tetragonal phase transition occurs and the material free energy becomes non-convex with multiple wells associated with the possible spontaneous polarization states.   (c) Under the application of a strong electric field, the material energy barrier can be overcome and the polarization can switch to another variant.

If a large electric field or stress field larger than the coercive strength is applied, the material response is nonlinear.   For example, when a large electric field with the direction opposite to the material spontaneous electric polarization is applied, the central titanium ion will move back towards the center of the cell and eventually shift towards the opposite direction to the initial polarization.   This phenomenon is called 180° switching, since the direction of electric polarization is reversed with the application of the large electric field.   This switching behavior is the fundamental mechanism associated with ferroelectricity.   When the direction of applied electric field is perpendicular to the initial electric polarization, and the electric field is large enough, the

7

titanium ion will ultimately shift toward in the direction of the electric field. In this case, the direction of polarization changes by 90° and is called 90° switching. When a large stress field is applied in a direction aligned with the initial polarization, 90° switching can also occur, and the switching is equally likely to occur in each of the four directions perpendicular to the original polarization. This behavior is called ferroelasticity since the switching is induced by stress.

If one considers of the material free energy, the spontaneous polarization and 180° switching can be explained from the illustrations in Figure 1.2.2. In Figure 1.2.2(a), the temperature is above the Curie temperature T_c, where the material resides in the cubic phase and the material free energy ψ is convex with a single well at zero polarization. Here, the cubic state is the stable state. When the temperature is below the Curie temperature, a cubic to tetragonal phase transition occurs and the material free-energy becomes non-convex with multiple wells associated with the possible spontaneous polarization states as in Figure 1.2.2(b). The zero-polarization state is still an equilibrium state but it is no longer stable, and the phase transition will occur due to any small perturbation. If a ferroelectric state, as shown in Figure 1.2.2(b), is under the application of a strong electric field, the energy barrier between equilibrium states can be overcome and the polarization can switch to another variant, which means, switching from one energy well to another. Such 180° switching is depicted in Figure 1.2.2(c).
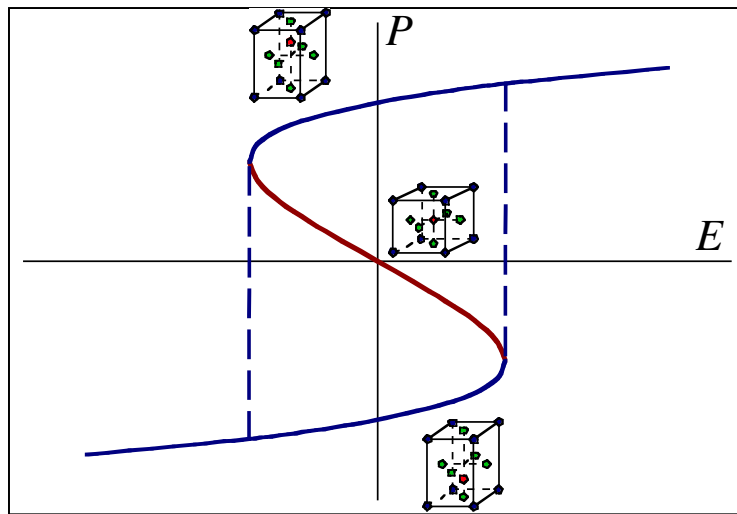
(a)
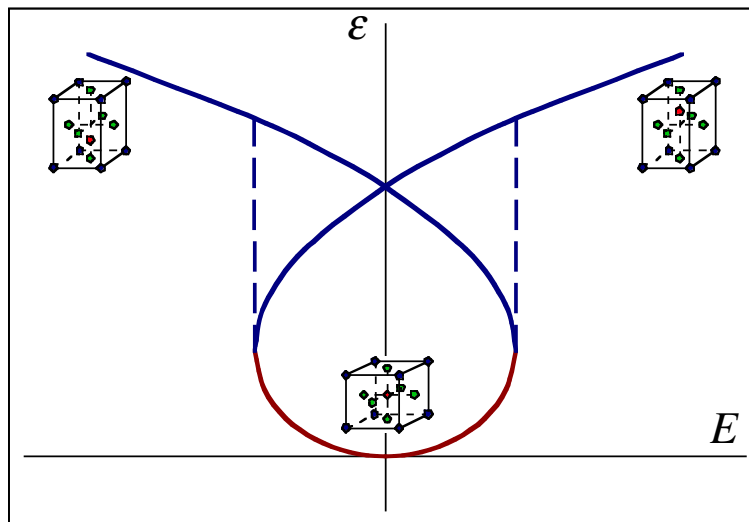
(b)

Figure 1.2.3:   The polarization and strain as the function of the electric field below the Curie temperature T_c.   The red portions of the curves correspond to unstable states, and the crystal jumps directly along the dashed line.

Figure 1.2.3 illustrates the polarization and strain derived from the free-energy as the function of electric field below the Curie temperature T_c.   The polarization versus electric field curve is obtained as $E = \partial\psi/\partial P$, and the strain is obtained from the

electrostrictive relationship $\varepsilon \propto P^2$. For the two the curves the portions marked as red correspond to the unstable states that are "passed over" during the switching process. These curves represent the fundamental dielectric hysteresis and the electromechanical "butterfly" loops for the unit cell.

1.3 DOMAIN STRUCTURE IN FERROELECTRIC MATERIALS

In the previous section, the electromechanical properties of an individual unit cell are discussed. However, typical materials such as barium titanate ($BaTiO_3$) and lead zironate titanate (PZT) are usually not produced as ideal single crystals. Instead, a polycrystalline structure of single crystal grains with different orientation is usually generated using ceramics processing techniques. The direction of the lattice axes are fixed within a grain, however, the orientation of the spontaneous polarization within a given grain is not necessarily unique. Instead, each grain may be divided into domains. Domains are regions with uniform spontaneous polarization, which means that the individual electric dipoles of the unit cells are pointing in the same direction within a single domain. The existence of grains and domains enriches the material constitutive response and integrates the properties arising from the unit cell. A set of domains with different polarization direction represents the domain structure. The non-linear ferroelectric material response and switching processes, as well as other properties are determined to a large degree by the state and mobility of the domain structure.

The change of material polarization in ferroelectric materials takes place by means of the displacement of boundaries between domains. The interface separating different domains is called a domain wall. The primary mechanism responsible for nonlinear ferroelectric constitutive response is the motion of domain walls. The

attractive and useful linear properties of many ferroelectrics, such as high piezoelectric constants and large dielectric constants, are primarily due to anelastic (i.e. recoverable) domain wall motion (Xu et al., 2005). The nature of domain walls and their interactions with other material defects is crucial for the understanding of the physical phenomena associated with the finite coercive strength of ferroelectrics, fracture toughening associated with domain switching (Wang and Landis, 2004), and electrical fatigue associated with pining of domain walls by migrating charge carriers (Warren et al., 1994; Xiao et al., 2005).
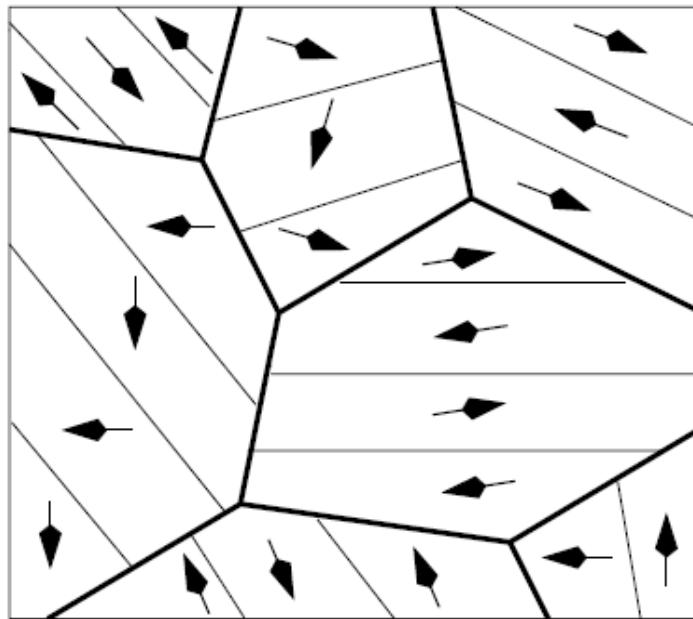
Figure 1.3.1: Plane view of a crystal aggregate with domains as subregions of equal spontaneous polarization after cooling below the Curie temperature T_c. The bold black lines represent the boundaries of different grains. And the fine grey lines inside each grain represent the boundary of different domains, which are also called domain walls. (Adapted from Kamlah, 2001)

A plane view of a crystal aggregated with domains as subregions of equal spontaneous polarization after cooling below the Curie temperature T_c is shown in Figure 1.3.1. The bold black lines represent the boundaries of different grains. And the fine grey lines inside each grain represent the boundary of different domains, which are also called domain walls.

As Figure 1.3.2 indicates, when the strength of applied electric field increases, the formerly random polarization orientation state becomes aligned towards the direction of the poling field. When the applied electric field becomes very high, the polarization reaches a saturation value when the unit cells that are able to switch is exhausted. After the external field is removed, the polarization does not return to zero, and the macroscopic average of the spontaneous polarization of the unit cells remains finite and is called the remanent polarization.
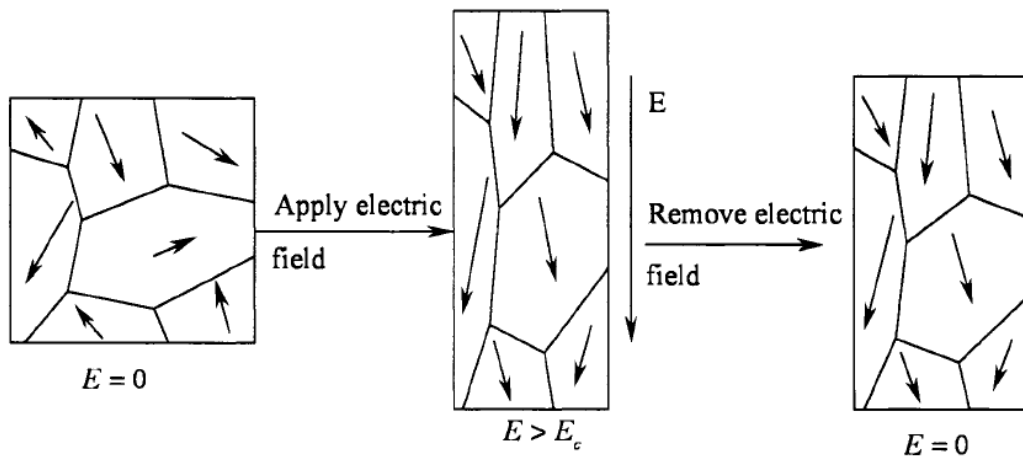
Figure 1.3.2: After unloading, the domain structure remains in the switched state, now possessing a resultant macroscopic polarization and thus, a macroscopic piezoelectric effect (Adapted from Kamlah, 2001).

Within a crystal, models of domain evolution at sub-micron size scales can be classified as sharp interface or diffuse interface (also called phase-field modeling) approaches. A schematic representation of these two different modeling approaches is shown in Figure 1.3.3.

Sharp Interface Model   Diffuse Interface Model
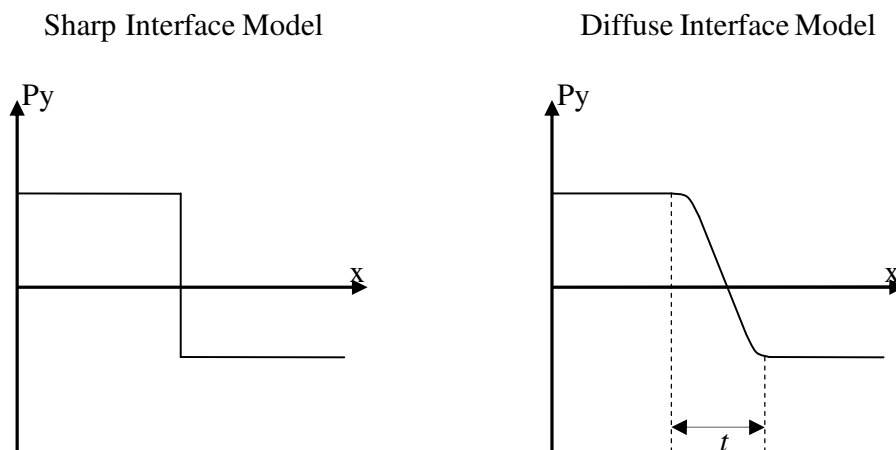
Figure 1.3.3: A schematic diagram of two different modeling approaches for 180° domain walls: the sharp interface model, and the diffuse interface model (or phase-field model). P_y represents the y-component of material polarization, and x represents dimension along the x-direction. In the diffuse interface model, t is the thickness of domain wall. The sharp interface model assumes zero thickness of the domain wall.

The sharp interface approach assumes the thickness of domain wall is zero, and the domain wall can move throughout the material. Given the location of the domain walls, the electromechanical fields in the material can be computed using linear piezoelectric theory. Essentially, the structure can be thought of as a composite where each domain is a different piezoelectric phase. Then the computation of thermodynamic driving forces on the domain walls is obtained by computing the jump in the Eshelby energy-momentum tensor across the domain wall interfaces (Loge and Suo, 1996; Jiang, 1994). The evolution of the domain structure is then carried out using a

13

phenomenological kinetic law which accounts for the dissipation that occurs as the domain wall traverses through the material. However, the sharp interface approach has to assume ad-hoc rules for the nucleation of new domains and disappearance of existing domains, and there are also some numerical issues associated with the changes in topology due to the merging of domains. On the contrary, diffuse interface or phase-field approaches allow for the nucleation of domains naturally without any specific rules, which is accomplished by defining a material free energy that depends on the mechanical strain, the electric field and the electric polarization in the material (such a free-energy is shown schematically in Figure 1.2.2). Employing the material polarization as the order parameter, the phase-field approach allows for a detailed accounting of the electromechanical processes that occur during the nucleation and growth of domains. Such approaches are useful in uncovering the coupled processes that occur during the fracture of ferroelectric crystals.

1.4 FRACTURE STUDIES OF FERROELECTRIC MATERIALS

Most ferroelectric ceramics exhibit a fracture toughness on the order of 1 MPa$\sqrt{m}$. This brittleness makes fracture an important consideration in the design of ferroelectric devices. Due to the strong electro-mechanical coupling properties of ferroelectric materials, it is a challenge to understand the details of the fracture process in these materials, especially when domain switching occurs near the crack tip.

One step in understanding the fracture of ferroelectrics is to investigate the details of the energy release rate for different loading scenarios. The energy release rate is the reduction in the potential energy per unit increase in the crack area, and can be interpreted as the energy flux to the crack front in a reversible system. In fracture

mechanics, understanding the energy release rate is important since it can provide a simple picture of the energetics of crack growth. Many researchers have investigated the energy release rate for cracks within the context of linear piezoelectricity, e.g. (Suo et al., 1992; McMeeking, 1999; Landis, 2004a; Landis, 2004b). These studies have shown that the evaluation of the energy release rate can be significantly affected by different electrical boundary conditions on the crack faces. These boundary conditions can be classified into three categories:

(1) Permeable boundary conditions, first proposed by Parton (Parton, 1976). This model assumes there is no distinction between deformed and undeformed configurations of the material within the assumptions of linear piezoelectricity. The electric potential and the normal component of the electric displacement are then continuous across the crack.

(2) Impermeable boundary conditions, proposed by Deeg (Deeg, 1980). Due to the fact that the permittivity of the medium within the crack gap is usually much lower than that of material, it is assumed that the permittivity of the medium can be approximated as zero. This assumption then implies that the normal components of electric displacement on both crack faces are zero.

(3) Semi-permeable boundary conditions, proposed by Hao and Shen (Hao and Shen, 1994). In order to address the facts that cracks are actually open and electric fields can permeate the crack gap, the crack faces are treated as an aggregate of tiny parallel plate capacitors.

All of these models assume traction free conditions on the crack faces, however, McMeeking (McMeeking, 2004) showed that this assumption can lead to a discrepancy between local and global energy release rates. To address this discrepancy, Landis (Landis, 2004b) proposed the so-called energetically consistent boundary conditions.

From his derivation, an additional closing traction is added to the semi-permeable boundary conditions in order to make the crack tip energy release rate and the total energy release rate equivalent to one another.

In addition to these, in this dissertation a modified impermeable boundary conditions is used when the direction of the initial polarization is perpendicular to the crack faces. The impermeable boundary conditions are generally too strong in situations where the single crystal has some initial polarization with a component normal to the crack faces. In such situations, a modified form of the impermeable boundary conditions will allows for a charge layer to reside on the crack faces to balance the normal component of the polarization.

1.5 OUTLINE

In Chapter 2, the governing equations for the phase-field modeling will be presented within a thermodynamically consistent framework, including a micro-force balance. Then a numerical method to solve the governing partial differential equations of the theory is presented. Here, the finite element method will be implemented using mechanical displacements, electric potential, and polarization components as nodal degrees of freedom. Some simulation results for the nucleation and growth of a domain from a crack tip will be given under different combinations of electrical and mechanical boundary conditions. In Chapter 3, a finite deformation theory of the phase-field model will be given. Here, the Jaumann rate of the polarization is used as the objective rate to make the description of the dissipation frame indifferent. Lastly, some electromechanical instabilities in dielectric elastomer composites are studied in Chapter 4.

16

Chapter II   Phase-Field Modeling of Domain Evolution

In this chapter, a thermodynamic framework based on a modern continuum mechanics approach that distinguishes the fundamental balance laws which are universal from the material constitutive response will be devised for a phase-field model of domain structure evolution in ferroelectrics.   Next, in order to solve the governing partial differential equations, a finite element method for the solution of the theory will be formulated and implemented using mechanical displacements, electric potential and electric polarization components as nodal degrees of freedom.   Then, for the study of fracture problems the electromechanical form of the J-integral is modified to account for the polarization gradient energy terms, and analyzed to illustrate the amount of shielding, or lack thereof, due to domain switching at the crack tip.   Finally the simulation results for the nucleation and growth of domains in ferroelectrics under different combinations of electrical and mechanical loading conditions will be presented and discussed.

2.1 PHASE-FIELD THEORY

Given a static domain structure, the equations governing the distributions of electromechanical fields in materials based on linear piezoelectricity are well established (Xu, 1991; Jona and Shirane, 1962; Lines and Glass, 1977), and there exists several different techniques that can be applied to solve for these fields (Allik and Hughes, 1970; Landis, 2002b).   However, we are not only interested in the distribution of the fields, but also in how these fields cause the domain structure to evolve.   Hence, this problem falls into a broader class of free boundary problems where the locations of the interfaces must also be determined as part of the solution.   Two modeling approaches can be applied: the sharp interface approach or the diffuse interface approach.   A sharp interface

approach includes physical questions associated with rules for domain nucleation, and numerical concerns associated with how to handle changes in topology of the domain structure.   In order to avoid these challenges, we choose to implement a diffuse interface or phase-field approach.

Historically, the phase-field equations governing the evolution of the domain configurations have been derived from a simple and physically justifiable set of assumptions based on energy minimization/reduction concepts.   While this approach is certainly sound, it obscures the modern continuum physics distinction between fundamental balance laws, which are applicable to a wide range of materials, and the constitutive equations that are valid for a specific material (Fried and Gurtin, 1993; Fried and Gurtin, 1994; Gurtin, 1996).   Next the fundamental governing phase-field equations are reviewed (Su and Landis, 2007).

Here, a small deformation non-equilibrium thermodynamics framework for ferroelectric domain evolution is presented.   The small deformation assumption is prevalent throughout most phase-field modeling studies.   The analysis of large deformation would introduce the concept of Maxwell stresses (McMeeking and Landis, 2005), which are assumed to be higher order effects that can be neglected.   In the next chapter the effect of large deformations will be considered and incorporated within the phase-field theory.   Now we begin with the fundamental equations governing the electromechanical fields under the assumption of small deformations and rotations.   It is also assumed that the fields vary very slowly with respect to the speed of light in the material, i.e. the quasi-static field approximation, but not necessarily with respect to the speed of sound, i.e. inertial effects are considered within the general derivation. Standard index notation is used with summation implied over repeated indices, the single

and double overdots represent first and second derivatives with respect to time, and $,j$ represents partial differentiation with respect to the x_j coordinate direction.

Balances of linear and angular momentum in any arbitrary volume V and its bounding surfaces S yield

$$\sigma_{ji,j} + b_i = \rho \ddot{u}_i \quad in \quad V, \tag{2.1}$$

$$\sigma_{ji} = \sigma_{ij} \quad in \quad V, \tag{2.2}$$

$$\sigma_{ji} n_j = t_i \quad on \quad S, \tag{2.3}$$

where σ_{ji} are the Cartesian components of the Cauchy stress, b_i the components of a body force per unit volume, ρ the mass density, u_i the mechanical displacements, n_i the components of a unit vector normal to a surface element, and t_i the tractions applied to the surface.

Under the assumptions of linear kinematics, the strain components ε_{ij} are related to the displacements as

$$\varepsilon_{ij} = \frac{1}{2}(u_{i,j} + u_{j,i}) \quad in \quad V, \tag{2.4}$$

The electrical quantities of electric field, E_i, electric potential, ϕ, electric displacement, D_i, volume charge density, q, and surface charge density, ω, are governed by the quasi-static forms of Maxwell's equations. Specifically, in any arbitrary volume V (including the region of free space) and its bounding surface S,

$$D_{i,i} - q = 0 \quad in \quad V, \tag{2.5}$$

19

$$D_i n_i = -\omega \quad on \quad S, \tag{2.6}$$

$$E_i = -\phi_{,i} \quad in \quad V, \tag{2.7}$$

Within the theory of linear piezoelectricity, the equations above (2.1)-(2.7) represent the fundamental balance laws and kinematic relationships, and the constitutive laws required to close the loop on the equations relate the stress and electric field to the strain and electric displacement. Such constitutive relationships can be derived from thermodynamic considerations using a material free energy that depends on the components of the strain and electric displacement (Nye, 1957). However, within the phase-field modeling approach the free energy will also be required to depend on an order parameter and its gradient. Mathematically, the order parameter is used to describe the different material variant types, i.e. the spontaneous states that are possible in a crystal. For the case of ferroelectrics, the physically natural order parameter is the electric polarization P_i.

The relationship between electric field, electric displacement and material polarization is given as

$$D_i = P_i + \kappa_0 E_i \quad in \quad V, \tag{2.8}$$

Here κ_0 is the permittivity of free space. The full forms of linear piezoelectric constitutive law about a fixed remanent strain and polarization state can be found in Appendix A.

Given that the free energy is permitted to depend on a new order parameter, a set of micro-forces are introduced that are work-conjugate to the order parameter and its gradient. Following the work of Fried and Gurtin (Fried and Gurtin, 1993; Fried and

Gurtin, 1994; Gurtin, 1996) we introduce a micro-force tensor ξ_{ji} such that $\xi_{ji}n_j\dot{P}_i$ represents the power density expended across surfaces by neighboring configurations, an internal micro-force vector π_i such that $\pi_i\dot{P}_i$ is the power density expended by the material internally, e.g. in the ordering of atoms within unit cells of the lattice (this micro-force accounts for dissipation in the material), and an external micro-force vector γ_i such that $\gamma_i\dot{P}_i$ is the power density expended by external sources. This micro-force is akin to the mechanical body force b_i and the electrical charge density q. The integral balance of this set of configurational forces leads to the differential balance law

$$\int_S \xi_{ji}n_j dS + \int_V \pi_i dV + \int_V \gamma_i dV = 0$$
$$\Rightarrow \xi_{ji,j} + \pi_i + \gamma_i = 0 \ \ in \ \ V.$$
(2.9)

The Helmholtz free energy of the material including the free space occupied by the material is assumed to take the general form:

$$\psi = \psi(\varepsilon_{ij}, D_i, P_i, P_{i,j}, \dot{P}_i)$$
(2.10)

We note that near Curie temperature, where ferroelectric phase transitions happen, temperature plays a key role. However, for isothermal behavior, the Helmholtz free energy remains the appropriate energy functional with the additional complication that the material parameters of free energy are temperature dependent (Devonshire, 1985; Jona and Shirane, 1962). Here we will deal only with isothermal behavior below the Curie temperature, but recognize that the extension to spatially homogeneous temperature dependent behavior can be readily included within the present framework by specifying the temperature at which the material properties must be evaluated. The inclusion of

21

inhomogeneous temperature dependent behavior and the associated heat transfer will requires an analysis of the second law of thermodynamics including such effects. In the following, we will only deal with the isothermal case.

Considering isothermal processes below the Curie temperature, the second law of thermodynamics is written as the Clausius-Duhem inequality as

$$\int_V \dot{\psi}\, dV + \int_V \frac{1}{2}\rho \dot{u}_i \dot{u}_i\, dV \le \int_V (b_i \dot{u}_i + \phi \dot{q} + \gamma_i \dot{P}_i)\, dV + \int_S (t_i \dot{u}_i + \phi \dot{\omega} + \xi_{ji} n_j \dot{P}_i)\, dS \quad (2.11)$$

Here the left hand side represents the rate of stored plus kinetic energy in the material and the right hand side represents the power expended by external sources on the body. Note that the internal micro-force π_i does not contribute to this external power term. Substitution into (2.11) of the balance laws of Equations (2.1)-(2.9), along with a liberal application of the divergence theorem yields

$$\int_V \frac{\partial \psi}{\partial \varepsilon_{ij}} \dot{\varepsilon}_{ij} + \frac{\partial \psi}{\partial D_i} \dot{D}_i + \frac{\partial \psi}{\partial P_i} \dot{P}_i + \frac{\partial \psi}{\partial P_{i,j}} \dot{P}_{i,j} + \frac{\partial \psi}{\partial \dot{P}_i} \ddot{P}_i\, dV$$
$$\le \int_V \sigma_{ji} \dot{\varepsilon}_{ij} + E_i \dot{D}_i + \xi_{ji} \dot{P}_{i,j} - \pi_i \dot{P}_i\, dV \qquad (2.12)$$

Note that the assumption implicit to Equation (2.10) is that the stress, electric field, micro-force tensor, and internal micro-force each are allowed to depend on $\varepsilon_{ij}, D_i, P_i, P_{i,j}$ and $\dot{P}_i$. The question is usually raised as to why the free energy must be allowed to depend on $\dot{P}_i$. The answer is that since the internal micro-force π_i is allowed to depend on $\dot{P}_i$, then all of the thermodynamic forces must also potentially have such dependence (Fried and Gurtin, 1993; Fried and Gurtin, 1994). It will be shown that the second law inequality ultimately allows only π_i to depend on $\dot{P}_i$ (see

Equations 2.13 and 2.14). For a given thermodynamic state, it is assumed that arbitrary levels of $\dot{\varepsilon}_{ij}, \dot{D}_i, \dot{P}_i, \dot{P}_{i,j}, and\ \ddot{P}_i$ are permissible through the appropriate control of the external sources b_i, q, and γ_i. Then, an analysis of the dissipation inequality of Equation (2.12) implies that

$$\frac{\partial \psi}{\partial \dot{P}_i} = 0 \Rightarrow \psi = \psi(\varepsilon_{ij}, D_i, P_i, P_{i,j}) \tag{2.13}$$

$$\sigma_{ji} = \frac{\partial \psi}{\partial \varepsilon_{ij}}, \ \ E_i = \frac{\partial \psi}{\partial D_i}, \ \text{and} \ \xi_{ji} = \frac{\partial \psi}{\partial P_{i,j}} \tag{2.14}$$

Finally, after defining $\eta_i \equiv \dfrac{\partial \psi}{\partial P_i}$, the internal micro-force π_i must satisfy

$$(\pi_i + \eta_i)\dot{P}_i \leq 0 \ \Rightarrow \pi_i = -\eta_i - \beta_{ij}\dot{P}_j$$

$$\text{with} \ \beta_{ij} = \beta_{ij}(\varepsilon_{kl}, D_k, P_k, P_{k,l}, \dot{P}_k) \ \text{positive definite} \tag{2.15}$$

If the tensor $\boldsymbol{\beta}$ is constant and the high-temperature phase is cubic then $\beta_{ij} = \beta\delta_{ij}$ where $\beta \geq 0$. This is the simplest and most widely applied form for β_{ij}.

Substitution of Equations (2.14c) and (2.15) into the micro-force balance of Equation (2.9) yields a generalized form of the Ginzburg-Landau equation governing the evolution of the material polarization in a ferroelectric material.

$$\left(\frac{\partial \psi}{\partial P_{i,j}}\right)_{,j} - \frac{\partial \psi}{\partial P_i} + \gamma_i = \beta_{ij}\dot{P}_j \ \ in \ V. \tag{2.16}$$

Therefore, our postulated set of micro-forces (2.9) is justified by the fact that their existence implies the accepted form of the phase-field equations. The primary differences between the present derivation of Equation (2.16) and the historical approach

is that a new balance law for micro-forces is introduced, and a distinction is made between the fundamental balance laws that must be applicable to all materials and the constitutive laws that are material specific.

Here, the Helmholtz free energy introduced in (2.10) and further constrained in (2.13) includes both energy stored in the material and the energy stored in the free space occupied by the material. Specifically, the free energy must be decomposed into the free energy of the material and the free energy of the free space such that

$$\psi(\varepsilon_{ij}, D_i, P_i, P_{i,j}) = \overline{\psi}(\varepsilon_{ij}, D_i, P_{i,j}) + \frac{1}{2\kappa_0}(D_i - P_i)(D_i - P_i) \qquad (2.17)$$

We now proceed to the specification of the material free energy. The goal for this task is that the general form of the free energy must contain a sufficient set of parameters such that for a given material these parameters can be fit to the spontaneous polarization, spontaneous strain, dielectric permittivity, piezoelectric coefficients and the elastic properties near the zero stress and zero electric field free spontaneous polarization and strain states. To accomplish this task we introduce the following form for the free energy,

$$
\begin{aligned}
\psi = {} & \frac{1}{2} a_{ijkl} P_{i,j} P_{k,l} \\
& + \frac{1}{2} \overline{a}_{ij} P_i P_j + \frac{1}{4} \overline{\overline{a}}_{ijkl} P_i P_j P_k P_l + \frac{1}{6} \overline{\overline{\overline{a}}}_{ijklmn} P_i P_j P_k P_l P_m P_n + \frac{1}{8} \overline{\overline{\overline{\overline{a}}}}_{ijklmnrs} P_i P_j P_k P_l P_m P_n P_r P_s \\
& + b_{ijkl} \varepsilon_{ij} P_k P_l + \frac{1}{2} c_{ijkl} \varepsilon_{ij} \varepsilon_{kl} + f_{ijklmn} \varepsilon_{ij} \varepsilon_{kl} P_m P_n + g_{ijklmn} \varepsilon_{ij} P_k P_l P_m P_n \\
& + \frac{1}{2\kappa_0}(D_i - P_i)(D_i - P_i)
\end{aligned}
$$

$$(2.18)$$

First note that each of the newly introduced material tensors must contain the symmetry of the high temperature phase, which for most ferroelectrics of interest is cubic. The first term of the free energy penalizes large gradients of polarization and gives domain walls thickness within the model. The four terms on the second line are used to create the non-convex energy landscape of the free energy with minima located at the spontaneous polarization states. The four terms on the third line are then used to fit the material's spontaneous strain along with the dielectric, elastic and piezoelectric properties about the spontaneous state. Note that the elastic, dielectric and piezoelectric properties are nonlinear, and therefore the tensor components are fit to the tangent material properties at the spontaneously polarized state. The final term represents the energy stored within the free space occupied by the material, and according to equation (2.8) is equivalent to $\kappa_0 E_i E_i / 2$.

The eighth rank term on the second line was introduced in order to allow for adjustments of the dielectric properties and the energy barriers for 90° switching reference. The sixth rank terms introduced on the third line allow us to fit the elastic, piezoelectric and dielectric properties of the low symmetry phase in the spontaneous state. Without these terms the elastic properties of the material arise only from the c_{ijkl} tensor, which must have the symmetry of the high temperature phase. Hence, the phase-field modeling that has been performed to date assumes that the elastic properties of tetragonal phase perovskites are both cubic and homogeneous, when in fact the elastic properties have tetragonal symmetry and can have different orientations across a 90° domain wall, i.e. they are inhomogeneous. With regard to the piezoelectric coefficients, b_{ijkl} is used to fit the spontaneous strain components associated with the stress and electric field free spontaneous polarization state. By introducing the f_{ijklmn} and g_{ijklmn} tensors, this general form of the free energy will be able to fit the magnitudes of the

25

spontaneous polarization and strain components, and the elastic, piezoelectric and dielectric constants near the spontaneous state. This allows for a relatively accurate representation of material properties and comparison of the behaviors of different material compositions.

2.2 FINITE ELEMENT FORMULATION

The governing equations for the phase-field model include Equations (2.1)-(2.9), (2.14), (2.15) and (2.18). When formulating a finite element method to solve these equations we must first identify the field quantities that will be used as nodal degrees of freedom. The simplest formulation would implement the components of mechanical displacement from which strain is derived, the components of electric polarization from which the polarization gradient is derived, and the electric potential or voltage from which electric field is derived. In order to implement such a formulation, the constitutive equations must take $\varepsilon_{ij}, P_i, P_{i,j}$ and E_i as the independent variables. However, the Helmholtz free energy has D_i instead of E_i as the independent variable. To address this difficulty, the following Legendre transformation is required to derive the electrical enthalpy h,

$$h(\varepsilon_{ij}, P_i, P_{i,j}, E_i) = \psi - E_i D_i$$

$$= \frac{1}{2} a_{ijkl} P_{i,j} P_{k,l}$$

$$+ \frac{1}{2} \bar{a}_{ij} P_i P_j + \frac{1}{4} \bar{\bar{a}}_{ijkl} P_i P_j P_k P_l + \frac{1}{6} \bar{\bar{\bar{a}}}_{ijklmn} P_i P_j P_k P_l P_m P_n + \frac{1}{8} \bar{\bar{\bar{a}}}_{ijklmnrs} P_i P_j P_k P_l P_m P_n P_r P_s$$

$$+ b_{ijkl} \varepsilon_{ij} P_k P_l + \frac{1}{2} c_{ijkl} \varepsilon_{ij} \varepsilon_{kl} + f_{ijklmn} \varepsilon_{ij} \varepsilon_{kl} P_m P_n + g_{ijklmn} \varepsilon_{ij} P_k P_l P_m P_n$$

$$- \frac{1}{2} \kappa_0 E_i E_i - E_i P_i$$

$$(2.19)$$

where the stresses, electric displacements, micro-forces, ξ_{ij} and η_i, are derived as

$$\sigma_{ji} = \frac{\partial h}{\partial \varepsilon_{ij}}, \quad D_i = -\frac{\partial h}{\partial E_i}, \quad \xi_{ji} = \frac{\partial h}{\partial P_{i,j}}, \quad and \quad \eta_i = \frac{\partial h}{\partial P_i} \qquad (2.20)$$

Then, given Equations (2.2), (2.4), (2.7) and (2.15), Equations (2.1), (2.3), (2.5), (2.6) and (2.9) can be derived from the following variational statement or principle of virtual work

$$\int_V \beta_{ij} \dot{P}_j \delta P_i dV + \int_V \rho \ddot{u}_i \delta u_i dV + \int_V \sigma_{ji} \delta \varepsilon_{ij} - D_i \delta E_i + \eta_i \delta P_i + \xi_{ji} \delta P_{i,j} dV$$

$$= \int_V b_i \delta u_i - q \delta \phi + \gamma_i \delta P_i dV + \int_S t_i \delta u_i - \omega \delta \phi + \xi_{ji} n_j \delta P_i dS \qquad (2.21)$$

Equation (2.21) is the foundation for the derivation of the finite element equations for the phase-field model. Again, the components of mechanical displacement, electric polarization and the electric potential are used as nodal degrees of freedom. The strain, electric field and polarization gradient are derived within the elements, and finally the stress, electric displacement and micro-forces are computed via Equation (2.20). We note that even though polarization gradient appears in the free energy, C_0 continuous elements are in fact suitable for the solution. This is a fortuitous consequence of

Equation (2.8), given that both electric field and polarization can be taken as independent variables. Therefore, the polarization components take the same status as mechanical displacement and electric potential and the polarization gradient takes the same status as strain and electric field. If, for example, the electric field were the order parameter, then higher order elements would be required in the formulation.

Again, each node in the finite element mesh has mechanical displacement, polarization and electric potential degrees of freedom. Then, defining the array of degrees of freedom as **d**, each of the field quantities are interpolated from the nodal quantities with the same set of shape functions such that

$$\begin{Bmatrix} u_i \\ \phi \\ P_i \end{Bmatrix} = [\mathbf{N}]\{\mathbf{d}\} \tag{2.22}$$

The shape function matrix **N** must meet all of the requirements for standard C_0 continuous elements. Hence, the displacements, electric potential and polarization components are approximated by continuous functions throughout the mesh, but strains, electric fields, and polarization gradients will have jumps in certain components along element boundaries

$$\dot{P}_i = \frac{P_i^{t+\Delta t} - P_i^t}{\Delta t}, \tag{2.23}$$

$$u_i = \alpha u_i^{t+\Delta t} + (1-\alpha)u_i^t, \ \phi = \alpha \phi^{t+\Delta t} + (1-\alpha)\phi^t \ and \ P_i = \alpha P_i^{t+\Delta t} + (1-\alpha)P_i^t \tag{2.24}$$

Here, the superscript indicates the time step at which the field is evaluated and α is a parameter between 0 and 1 that describes how the solution fields are interpolated in

28

time during a given time step. When $\alpha = 0$ the first order accurate forward Euler integration scheme is recovered, $\alpha = 1$ represents the first order accurate backward Euler scheme that allows for enhanced numerical stability with larger time increments, and $\alpha = 0.5$ is the second order accurate Crank-Nicholson method.

Given a known set of nodal degrees of freedom at time t, when the finite element interpolations of Equation (2.2) and the time integration approximations of Equations (2.23) and (2.24) are substituted into Equation (2.21), a set of nonlinear algebraic equations results for the nodal degrees of freedom at $t + \Delta t$ that can be written in the form

$$\mathbf{B}\left(\mathbf{d}^{t+\Delta t}\right) = \mathbf{F} \tag{2.25}$$

These equations are solved with the Newton-Raphson method:

$$\left.\frac{\partial \mathbf{B}}{\partial \mathbf{d}}\right|_{\mathbf{d}_i^{t+\Delta t}} \Delta \mathbf{d}_i = \mathbf{F} - \mathbf{B}\left(\mathbf{d}_i^{t+\Delta t}\right) \tag{2.26}$$

where i is the current step counter in the Newton-Raphson sequence and $\Delta \mathbf{d}_i$ is the increment computed for $\mathbf{d}_i^{t+\Delta t}$ such that $\mathbf{d}_i^{t+\Delta t} = \mathbf{d}_{i-1}^{t+\Delta t} + \Delta \mathbf{d}_i$. The Newton-Raphson procedure is carried out until a suitable level of convergence is obtained yielding a solution for the displacement, electric potential, and polarization fields at time step $t + \Delta t$. With this new set of known nodal degrees of freedom in hand, the next time increment is computed by solving the updated form of Equation (2.25).

2.3 J-INTEGRAL

We now proceed to the specification of the *J*-integral (for two-dimensional crack problems) for materials described with this phase-field theory. J is given as,

$$J = \int_\Gamma (h n_1 - \sigma_{ji} n_j u_{i,1} + D_i n_i E_1 - \xi_{ji} n_j P_{i,1}) d\Gamma \qquad (2.27)$$
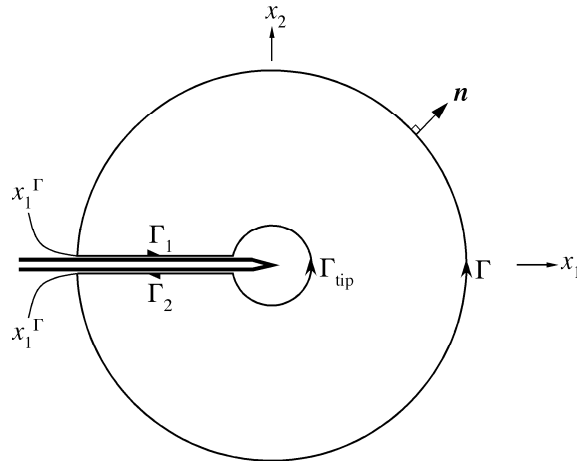
Figure 2.3.1: The closed contour used to evaluate the crack tip energy release rate.

Here we have introduced the electrical enthalpy h which can be related to the Helmholtz free energy through the Legendre transformation $h(\varepsilon_{ij}, P_i, P_{i,j}, E_i) = \psi - E_i D_i$. Recall that through h the constitutive relationships are,

$$\sigma_{ji} = \frac{\partial \psi}{\partial \varepsilon_{ij}}, \ \ D_i = -\frac{\partial \psi}{\partial E_i}, \ \xi_{ji} = \frac{\partial \psi}{\partial P_{i,j}}, \ \text{and} \ \eta_i = \frac{\partial h}{\partial P_i} \qquad (2.28)$$

We first demonstrate that J is equal to zero around any closed contour not enclosing a singularity,

30

$$J = \int_\Gamma (hn_1 - \sigma_{ji}n_j u_{i,1} + D_i n_i E_1 - \xi_{ji}n_j P_{i,1})d\Gamma$$

$$= \int_A \left(h_{,1} - \underbrace{\sigma_{ji,j}}_{-b_i} u_{i,1} - \sigma_{ji}u_{i,j1} + \underbrace{D_{i,i}}_{q} E_1 + D_i E_{i,1} - \underbrace{\xi_{ji,j}}_{\eta_i + \beta_{ij}\dot{P}_j} P_{i,1} - \xi_{ji}P_{i,j1} \right) dA$$

$$= \int_A (h_{,1} - \sigma_{ji}u_{i,j1} + D_i E_{i,1} - \eta_i P_{i,1} - \xi_{ji}P_{i,j1})\, dA$$

$$\text{if } b_i = 0, q = 0, \text{ and } \dot{P}_i = 0 \text{ in A.}$$

$$= \int_A \left(\underbrace{\frac{\partial h}{\partial \varepsilon_{ij}}}_{\sigma_{ji}}\varepsilon_{ij,1} + \underbrace{\frac{\partial h}{\partial E_i}}_{-D_i}E_{i,1} + \underbrace{\frac{\partial h}{\partial P_i}}_{\eta_i}P_{i,1} + \underbrace{\frac{\partial h}{\partial P_{i,j}}}_{\xi_{ji}}P_{i,j1} - \underbrace{\sigma_{ji}u_{i,j1}}_{\sigma_{ji}\varepsilon_{ij,1}} + D_i E_{i,1} - \eta_i P_{i,1} - \xi_{ji}P_{i,j1} \right) dA$$

$$= 0$$

$$(2.29)$$

Note that this result only holds under the conditions where $b_i = 0$, $q = 0$, and $\dot{P}_i = 0$ in A. Most notably this implies that the micro-force balance associated with the order parameter must be in equilibrium and specifically the "viscous" term $\beta_{ij}\dot{P}_j$ must vanish.

Next, we recognize and state without proof that the crack tip energy release rate G is equal to the J-integral for an infinitesimally small contour about the crack tip. This statement is supported by the fact that J provides the energy flux into the contour for a virtual motion of the contour in the x_1-direction. Then, by computing J about the contour illustrated in Figure 2.3.1, it can be shown that,

$$G = J_{\Gamma_{tip}} = J_\Gamma + J_{\Gamma_1} + J_{\Gamma_2} \tag{2.30}$$

$$J_\Gamma = \int_\Gamma (hn_1 - \sigma_{ji}n_j u_{i,1} + D_i n_i E_1 - \xi_{ji}n_j P_{i,1})d\Gamma \tag{2.31}$$

$$J_{\Gamma_1} = \int_{x_1^+}^0 (\sigma_{21}u_{1,1} + \sigma_{22}u_{2,1} - D_2 E_1)dx_1 \tag{2.32}$$

$$\text{assuming } \xi_{ji}n_j = 0 \text{ on the crack faces}$$

31

$$J_{\Gamma_2} = \int_{x_1^-}^{0} (-\sigma_{21} u_{1,1} - \sigma_{22} u_{2,1} + D_2 E_1) dx_1$$

$$\text{assuming } \xi_{ji} n_j = 0 \text{ on the crack faces}$$

(2.33)

The assumption of $\xi_{ji} n_j = 0$ is a reasonable assumption on any free surface as it assumes that no micro-forces are applied to the surface by external agencies. The remaining crack face boundary conditions are less well-defined. Two very popular sets of linear crack face boundary conditions are the permeable and impermeable boundary conditions. Both of these sets of boundary conditions assume that the crack faces are traction free. For the impermeable boundary conditions it is assumed that the normal component of the electric displacement is zero, and for the permeable boundary conditions it is assumed that both the electric potential and the normal component of the electric displacement are continuous across the crack. For the impermeable boundary conditions $J_{\Gamma_1} = J_{\Gamma_2} = 0$ and for the permeable boundary conditions $J_{\Gamma_1} + J_{\Gamma_2} = 0$ if $x_1^+ = x_1^- = x_1^\Gamma$. In either case the J-integral around any contour is equal to the crack tip energy release rate, $G = J_\Gamma$.

The impermeable boundary conditions are generally too strong in situations where the single crystal has some initial polarization with a component normal to the crack faces. In such situations it is possible and perhaps likely that charge layers will reside on the crack faces to balance the normal component of the polarization. Hence, a modified form of the impermeable boundary conditions would allow for these charge layers such that $D_2^\pm = \omega_0$, where $\omega_0 = P_2^S$ is the surface charge density required to balance the initial spontaneous polarization in the material. For the sake of simplicity we will assume that this spontaneous polarization is homogeneous throughout the crystal (or at least on the crack faces), although more complicated distributions could also be

envisioned and analyzed. We will also retain the traction free conditions. Under these conditions we can show that

$$J_{\Gamma_1} + J_{\Gamma_2} = \omega_0 \int_{x_1^+}^{0} \frac{\partial \phi}{\partial x_1} dx_1 - \omega_0 \int_{x_1^-}^{0} \frac{\partial \phi}{\partial x_1} dx_1 = -\omega_0 \left[\phi\left(x_1^+, 0\right) - \phi\left(x_1^-, 0\right) \right] \qquad (2.34)$$

Then, the crack tip energy release rate is,

$$G = J_\Gamma - \omega_0 \left[\phi\left(x_1^+, 0\right) - \phi\left(x_1^-, 0\right) \right] \qquad (2.35)$$

In addition to the types of linear boundary conditions, there have also been two sets of non-linear crack-face boundary conditions. The semi-permeable boundary conditions due to Hao and Shen (Hao and Shen, 1994; Dunn, 1994; McMeeking, 1999; McMeeking, 2004), and the energetically consistent boundary conditions due to Landis (Landis, 2004b; Li et al., 2008; Motola and Banks-Sills, 2009; Motola et al., 2009). Since it has been shown that the semi-permeable boundary conditions lead to a discrepancy between the total and crack-tip energy release rates (McMeeking, 2004; Landis, 2004b), we will focus only on the energetically consistent boundary conditions here. The energetically consistent boundary conditions postulate that the medium within the crack gap can be described by an electrical enthalpy $h_c = h_c(E_c)$, where E_c is the electric field within the crack gap. This approximation assumes that the crack gap can be treated as a one-dimensional capacitor where the tangential components of the electric field can be neglected. Then E_c is given as,

$$E_c = -\frac{\Delta \phi}{\Delta u_2} \qquad (2.36)$$

33

where $\Delta u_2 = u_2^+ - u_2^-$ is the crack opening displacement and $\Delta\phi = \phi^+ - \phi^-$ is the electric potential jump across the crack faces. The electric displacement and the stress within the crack gap are derived from the crack gap electrical enthalpy as,

$$D_c = -\frac{dh_c}{dE_c} \quad \text{and} \quad \sigma_c = h_c + E_c D_c \tag{2.37}$$

Allowing for the initial charge layers on the crack faces the energetically consistent crack-face boundary conditions become $\sigma_{21}^\pm = 0, \sigma_{22}^\pm = \sigma_c$, and $D_2^\pm = \omega_0 + D_c$. Then, using $x_1^+ = x_1^- = x_1^\Gamma$ the analysis of the crack-face J paths follows as,

$$
\begin{aligned}
J_{\Gamma_1} + J_{\Gamma_2} &= \int_{x_1^\Gamma}^0 \left[\sigma_c \Delta u_{2,1} + (\omega_0 + D_c)\Delta\phi_{,1}\right] dx_1 \\
&= \int_{x_1^\Gamma}^0 \left[(h_c + E_c D_c)\Delta u_{2,1} + (\omega_0 + D_c)\Delta\phi_{,1}\right] dx_1 \\
&= \int_{x_1^\Gamma}^0 \left[(h_c - \frac{\Delta\phi}{\Delta u_2} D_c)\Delta u_{2,1} + (\omega_0 + D_c)\Delta\phi_{,1}\right] dx_1 \\
&= \int_{x_1^\Gamma}^0 \left[(h_c \Delta u_2 - \Delta\phi D_c)_{,1} - h_{c,1}\Delta u_2 + \Delta\phi D_{c,1} + \Delta\phi_{,1} D_c \right. \\
&\qquad\quad \left. - \frac{\Delta\phi}{\Delta u_2} D_c \Delta u_{2,1} + (\omega_0\Delta\phi + D_c\Delta\phi)_{,1} - D_{c,1}\Delta\phi\right] dx_1 \\
&= \int_{x_1^\Gamma}^0 \left[(h_c \Delta u_2 + \omega_0\Delta\phi)_{,1} - \frac{dh_c}{dE_c} E_{c,1}\Delta u_2 + \Delta\phi D_{c,1} + \Delta\phi_{,1} D_c \right. \\
&\qquad\quad \left. + E_c D_c \Delta u_{2,1} - D_{c,1}\Delta\phi\right] dx_1 \\
&= \int_{x_1^\Gamma}^0 \left[(h_c \Delta u_2 + \omega_0\Delta\phi)_{,1} - D_c\left(\frac{\Delta\phi_{,1}}{\Delta u_2} - \frac{\Delta\phi \Delta u_{2,1}}{(\Delta u_2)^2}\right)\Delta u_2 + \Delta\phi D_{c,1} \right. \\
&\qquad\quad \left. + \Delta\phi_{,1} D_c + E_c D_c \Delta u_{2,1} - D_{c,1}\Delta\phi\right] dx_1 \\
&= \int_{x_1^\Gamma}^0 (h_c \Delta u_2 + \omega_0\Delta\phi)_{,1} dx_1 \\
&= -h_c^\Gamma \Delta u_2^\Gamma - \omega_0\Delta\phi^\Gamma
\end{aligned}
$$

Hence, the crack-tip energy release rate is,

$$G = J_\Gamma - h_c^\Gamma \Delta u_2^\Gamma - \omega_0 \Delta \phi^\Gamma \qquad (2.38)$$

We note that there are limiting representations of h_c that can be used to reproduce both the impermeable and permeable boundary conditions. Notably, when the dielectric breakdown strength of the crack gap medium is small (rigorously in the limit as this strength goes to zero) the permeable boundary conditions are recovered, giving a possible physical mechanism for this model of the crack-face boundary conditions.

2.4 SIMULATION RESULTS

In this section, first, we present the simulation results to demonstrate under what conditions a remote J path can be used to determine the crack tip energy release rate. The governing equations in Section 2.1 were solved using the finite element method described in Section 2.2 (Su and Landis, 2007). Next, the domain nucleation criteria at a crack tip under the combination of KI-KD fields are studied. Then, the nucleation and growth of domains during different combinations of mechanical and electrical loadings are simulated. Finally, the results are discussed. The material properties used here are characteristic of barium titanate ($BaTiO_3$) and are listed in Appendix B.

2.4.1 Energy Release Rate and J-integral

We studied two-dimensional square geometries, and the crack length equal to one half of the length of the side of this square region. The characteristic thickness of domain wall within the theory is $2 l_0$. Here we use the generalized impermeable

boundary conditions on the crack faces such that the crack faces are traction free and there is a fixed surface charge density on the crack faces that exactly balances the normal component of the initial spontaneous polarization.

The first simulation is for a material with initial spontaneous polarization P_0 normal to the crack faces in a $200\,l_0 \times 200\,l_0$ domain. The entire boundary of the square region is traction free, and the left and right sides of the region have no surface charge density. The top and bottom surfaces have an applied surface charge density of $\omega^\pm = \mp(P_0 - \omega_A)$ as shown in Figure 2.4.1. Note that when the surface charge increment ω_A is equal to zero, the stresses and electric fields in the sample are also equal to zero, and this is the initial state of this simulation with $\omega_A = 0$ and $\sigma_{ij} = 0$, $E_i = 0$, $P_y / P_0 = 1$ in the body.
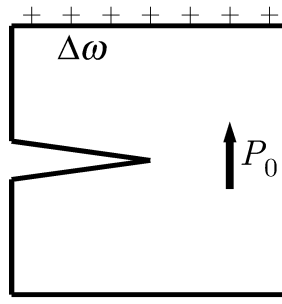
Figure 2.4.1: A schematic plot of the specimen. In this $200\,l_0 \times 200\,l_0$ domain, the entire boundary is traction free, and the left and right sides of the region have no surface charge density. The top and bottom surfaces have an applied surface charge density of $\omega^\pm = \mp(P_0 - \omega_A)$.

Here we increase ω_A to apply the charge loading on the top and bottom surfaces with different $\beta\dot{\omega}_A / E_0$ rates. For the tensor β_{ij}, we always take the form of $\beta_{ij} = \beta\delta_{ij}$. Note that $\beta\dot{\omega}_A / E_0 = 0$ corresponds to equilibrium calculations. The parameter E_0 used for normalization is the characteristic level of electric field required

36

to cause homogeneous 180° switching of a spontaneously polarized sample. Before any domain switching, we investigated the normalized rates of charge loading with $\beta\dot{\omega}_A / E_0 = 0, 0.1,$ and 1 at the same accumulated charge loading level, and the energy release rate is calculated from the J-integral and the results from different normalized rates of charge loading are compared.
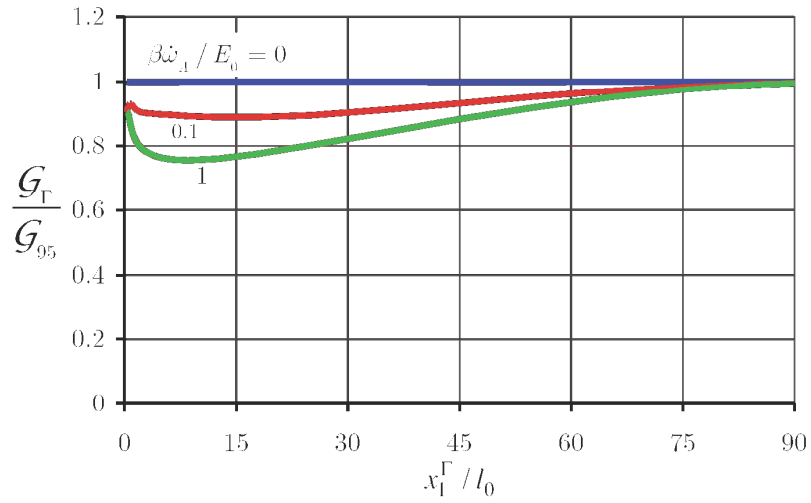
Figure 2.4.2: The apparent crack-tip energy release rate computed using $G_\Gamma = J_\Gamma - \omega_0\big[\phi(x_1^+,0) - \phi(x_1^-,0)\big]$ at a charge loading level of $\omega_A / P_0 = 0.05$. The J-contour used to compute G_Γ is a square contour with sides of length $2x_1^\Gamma$.

Figure 2.4.2 illustrates the path-dependence of the apparent energy release rate computed from $G_\Gamma = J_\Gamma - \omega_0\big[\phi(x_1^+,0) - \phi(x_1^-,0)\big]$ (Equation (2.35)) for a small charge load level $\omega_A / P_0 = 0.05$ for the three different loading rates $\beta\dot{\omega}_A / E_0 = 0, 0.1,$ and 1. The far-field value of G_Γ is $G_{95} / E_0 P_0 l_0 = $-1.8, -3.5 and -18.2 for $\beta\dot{\omega}_A / E_0 = 0, 0.1,$ and 1 respectively. Note that for the equilibrium case $\beta\dot{\omega}_A / E_0 = 0$, the calculation of G_Γ is path-independent and a valid result for the crack-tip energy release rate is obtained for

any path. For the two non-equilibrium cases $\beta\dot{\omega}_A / E_0 = 0.1$ and 1, the calculation is not path-independent and cannot be interpreted as the crack-tip energy release rate except in the limit as $x_1^\Gamma \to 0$. This path-dependent behavior in non-equilibrium cases cannot be interpreted as shielding due to domain switching since no domain switching has occurred in these calculations yet. The path-dependence is due to the dissipative behavior of the term $\beta\dot{P_i}$ in the micro-force balance.

In summary, the J-integral is only path-independent in the equilibrium case where $\beta\dot{\omega}_A / E_0 = 0$, and can be used to determine the crack-tip energy release rate from $G_\Gamma = J_\Gamma - \omega_0 \left[\phi(x_1^+, 0) - \phi(x_1^-, 0) \right]$, with the modified impermeable boundary conditions when the initial polarization is perpendicular to the crack surfaces.

2.4.2 Domain Nucleation with KI-KD Loading

Note that generating domain switching zones in these simulations for the equilibrium case with $\beta\dot{\omega}_A / E_0 = 0$ is not a trivial task. For the $200\,l_0 \times 200\,l_0$ region it is not possible to find equilibrium solutions for charge loading level $\omega_A / P_0 > 0.08$ by simply incrementing the electrical loading with $\beta = 0$. This suggests an instability in the solution which is due to a new domain structure nucleating at the crack tip. Such conditions for domain nucleation can be studied under small-scale-switching conditions where the material region near the crack tip experiences loadings of sufficient magnitude to cause considerable non-linear response is small in comparison to any other length scales associated with the specimen, such as crack or ligament length. For such situations, the electromechanical fields in a so-called K-annulus will be dominated by the linear piezoelectric $K_I - K_D$ fields. The $K_I - K_D$ fields are generated with the Stroh formalism (see Appendix C) and the mechanical

38

displacements and electric potential associated with these fields are applied to the outer boundary of the $200\,l_0 \times 200\,l_0$ region as sketched in Figure 2.4.3(a).

The electric displacement intensity factor K_D, is defined similarly as K_I,

$$K_I = \lim_{r \to 0} \sqrt{2\pi r}\, \sigma_{22}(r, \theta = 0)\,, K_D = \lim_{r \to 0} \sqrt{2\pi r}\, D_2(r, \theta = 0) \tag{2.39}$$

Here, r, θ are the distance from the crack tip and the angle from the positive x_1 axis respectively as shown in Figure 2.4.3(b).

(a)   (b)
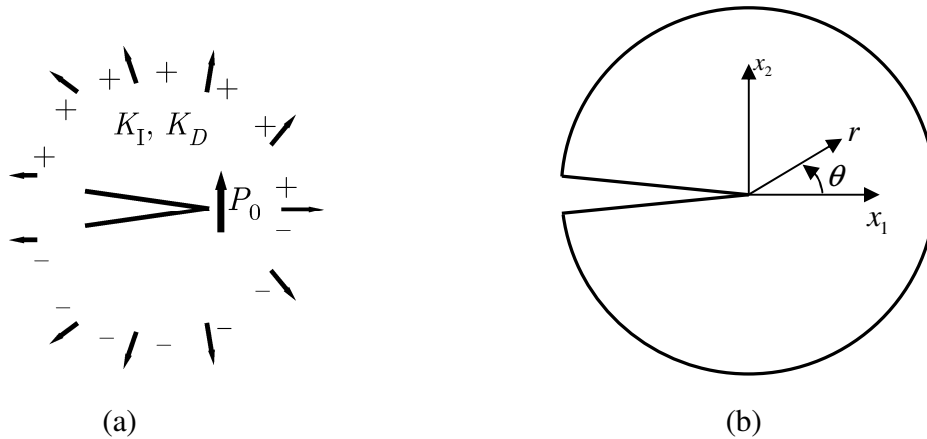
Figure 2.4.3:   (a) A schematic of the semi-infinite crack loaded by a combination of electrical and mechanical loads characterized by the mode I stress intensity factor, K_I, and the electric displacement mode intensity factor, K_D.   (b) A schematic of the semi-infinite crack. The mode I stress intensity factor, K_I, and the electric displacement mode intensity factor, K_D, are defined as $K_I = \lim_{r \to 0} \sqrt{2\pi r}\, \sigma_{22}(r, \theta = 0)$, $K_D = \lim_{r \to 0} \sqrt{2\pi r}\, D_2(r, \theta = 0)$.   Here, r, θ are the distance from the crack tip and the angle from the positive x_1 axis respectively.

In the simulation, the mode I stress intensity factor, K_I, and the electric displacement intensity factor, K_D, are increased proportionally until an instability in the

39

solution is found. This instability is associated with the nucleation of a new domain from the crack tip. The growth of such a domain will be presented in the next section. Figure 2.4.3(a) shows a schematic of the crack loaded by $K_I - K_D$ fields. A plot of the critical combinations of K_I and K_D required to nucleate a new domain in a material with initial polarization perpendicular to the crack faces is shown in Figure 2.4.4. The generalized impermeable crack-face boundary conditions are applied in these simulations.

First note that the orientation of the K_D fields plotted in Figure 2.4.4 is such that the initial spontaneous polarization in the sample tends to be reversed. Also note that the intensity factors are normalized by material specific properties including the domain wall length scale l_0.
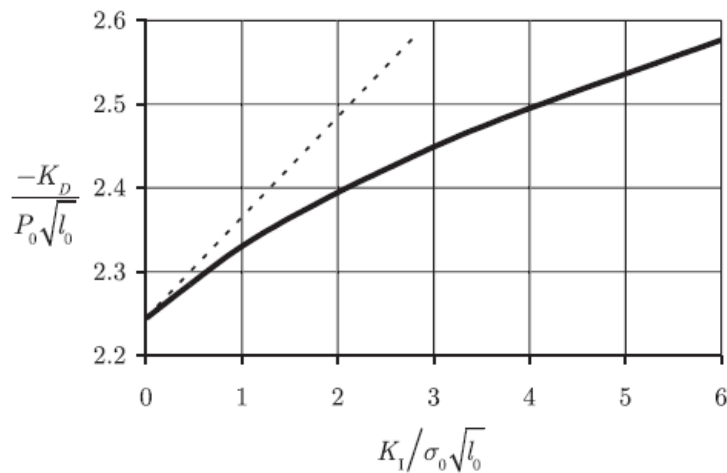
Figure 2.4.4: The graph plots the critical combination of mode I stress intensity factor and electric displacement intensity factor required to nucleate a new domain at the crack tip. The solid line is calculated from the full model equations and the dashed line is from equation (2.39) with the numerical constant fit to the point at $K_I = 0$. Note that the mechanical stress intensity has a mild effect on the nucleation process for this configuration of crack orientation and spontaneous polarization orientation.

The results displayed in Figure 2.4.4 show that the mechanical loading plays a limited role in the nucleation of a new domain from the crack tip for these material properties. These results are in qualitative agreement with theories based upon energetic considerations which postulate that 90° switching occurs when the work due to the applied stresses and electric fields on the switching process attain a critical level. Roughly, without accounting for all of the details of the near-tip fields, such an approximation yields,

$$\frac{K_I}{\sigma_0 \sqrt{l_0}} + \frac{K_D}{P_0 \sqrt{l_0}} \frac{P_0}{\kappa E_0} = \text{constant.} \tag{2.40}$$

The dashed line in Figure 2.4.4 shows this approximation when the constant is fit to the point when $K_I = 0$. When considering equation (2.40), note that E_0 is the critical field for homogeneous 180° switching, not the field required to move existing domain walls which is considerably smaller.
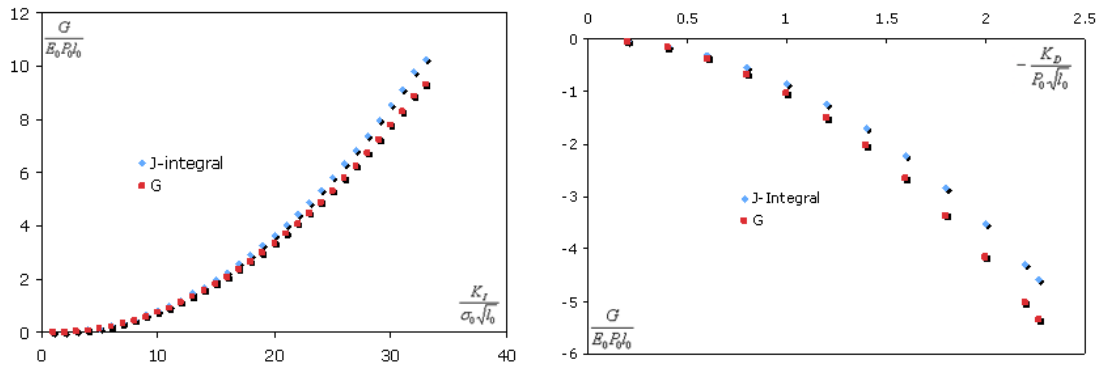
Figure 2.4.5: The energy release rate G calculated from applied $K_I - K_D$ loading using the Irwin matrix as shown in Appendix C, is compared to J-integral which is path-independent for the equilibrium states. The left figure is for pure K_I loading and the right figure is for pure K_D loading.

41

In Figure 2.4.5, the applied energy release rate G_{app} calculated from applied K_D loading using the Irwin matrix as shown in Appendix C, is compared to the J-integral which is path-independent for these equilibrium states. The left figure is for pure K_I loading and the right figure is for pure K_D loading. The crack-tip energy release rate with pure electrical loading is negative for impermeable crack-face boundary conditions, which is accordance with linear piezoelectric fracture mechanics.

Figure 2.4.6: Two contour plots of the x and y-components of the polarization normalized by P_0 in the vicinity of the crack tip when a new domain structure is nucleated under K-field loading. Due to symmetry, only the upper half of the model is displayed. The x and y distances are normalized as x/l_0 and y/l_0, and the polarization scale is normalized by the spontaneous polarization P_0.

To demonstrate the material polarization at the nucleation, Figure 2.4.6 shows contour plots of the x and y-components of the polarization normalized by P_0 in the vicinity of the crack tip when a new domain structure is nucleated under K field loading. Due to symmetry, only the upper half of the $200\,l_0 \times 200\,l_0$ region is plotted. The x and y distances are normalized as x/l_0 and y/l_0, and the polarization scale is normalized by the spontaneous polarization P_0

2.4.3 Purely Electrical Loading: Charge Load

In this section, the growth of a new domain from a crack tip during purely electrical loading: charge loading is simulated. We studied a two-dimensional square geometry with the length of the side of the square equal to $60\,l_0$, and the crack length equal to $30\,l_0$. The characteristic thickness of domain wall within the theory is $2\,l_0$. The generalized impermeable boundary conditions on the crack faces are used here such that the crack faces are traction free and there is a fixed surface charge density on the crack faces that exactly balances the normal component of the initial spontaneous polarization.

As shown in Figure 2.4.1, the initial spontaneous polarization P_0 is normal to the crack faces. The entire boundary of the square region is traction free, and the left and right sides of the region have no surface charge density. The top and bottom surfaces have an applied surface charge density of $\omega^{\pm} = \mp(P_0 - \omega_A)$. Note that when the surface charge increment ω_A is equal to zero, this is the initial state of the simulation with $\omega_A = 0$ and $\sigma_{ij} = 0, E_i = 0, P_y/P_0 = 1$ in the body. Then ω_A is increased to apply the charge loading on the top and bottom surfaces.

To generate the solution for a final equilibrium domain configuration, the domain was nucleated at the crack tip and allowed to evolve with a non-zero polarization viscosity term. The loading is applied by first ramping up a uniform charge load on the top and bottom surfaces with a charging rate of $\beta\dot{\omega}_A/E_0 = 0.1$ to a total charge of $\omega_A/P_0 = 0.12$ in the $60\,l_0 \times 60\,l_0$ domain. The charge was then fixed at $\omega_A/P_0 = 0.12$ and the domain structure was allowed to evolve until the solution was sufficiently close to the equilibrium configuration, at which point the polarization viscosity term was set to $\beta = 0$, to find the final equilibrium solution (Figure 2.4.7a).

Thereafter the additional charge is applied to the surface to a final value of $\omega_A / P_0 = 0.2$ and lastly the charge is removed from the surface to return to the initial uncharged state.
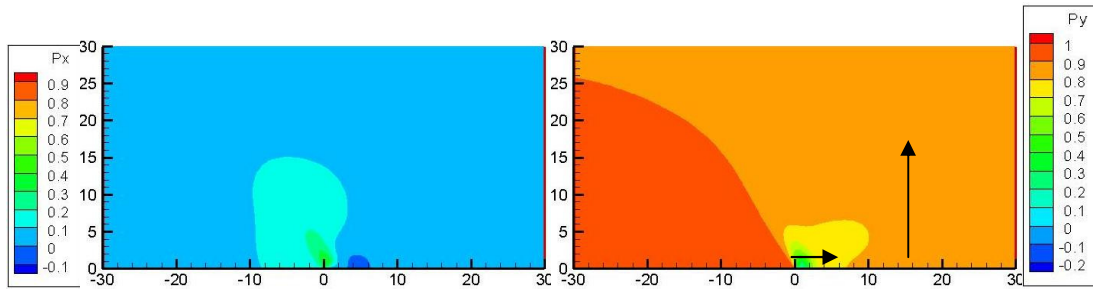
Domain Nucleation at $\omega_A / P_0 = 0.12$
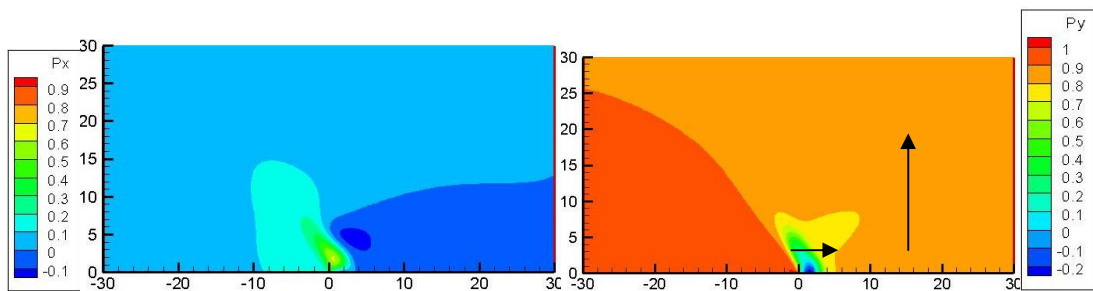
Domain Evolution at $\omega_A / P_0 = 0.12$

Figure 2.4.7a: Contour plots of the x and y-components of the polarization normalized by P_0 in the vicinity of the crack tip during the evolution of the domain structure with the fixed charge loading $\omega_A / P_0 = 0.12$ at different times, from the nucleation of the domain to the final equilibrium configuration. Due to symmetry, only the upper half of the model is displayed. The x and y distances are normalized as x/l_0 and y/l_0, and the polarization scale is normalized by the spontaneous polarization P_0. The arrows represent the nominal direction of the polarization in different regions.
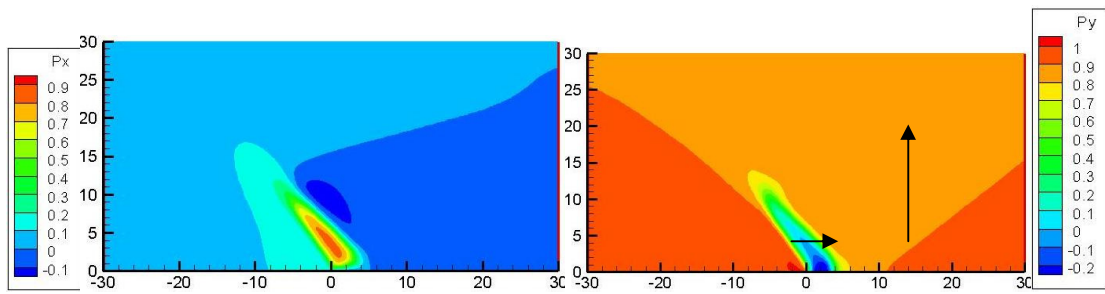
Domain Evolution at $\omega_A / P_0 = 0.12$
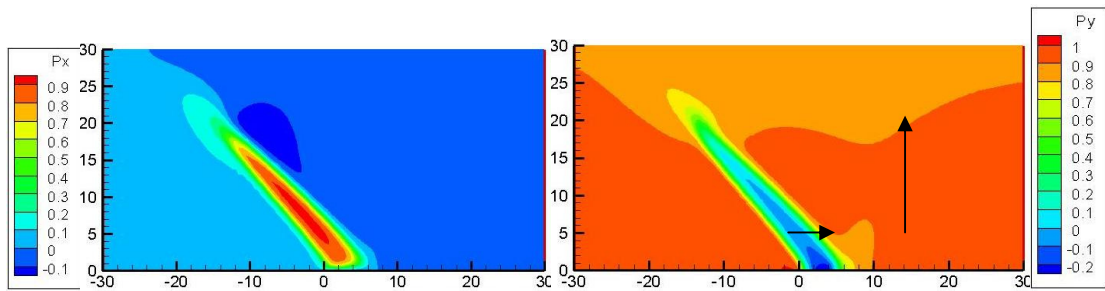
Domain Evolution at $\omega_A / P_0 = 0.12$
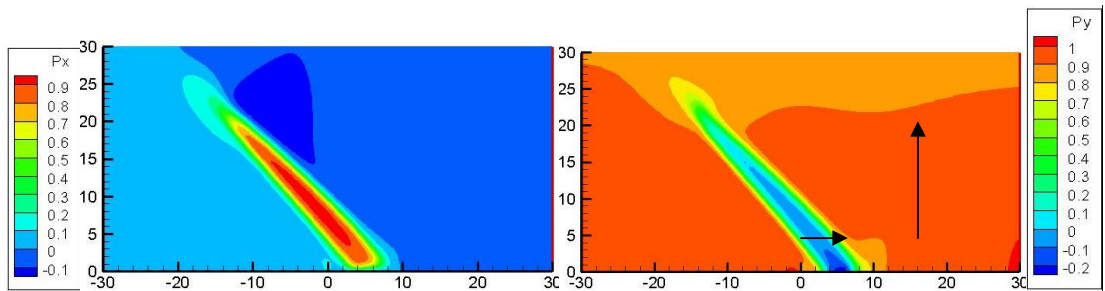
Final Equilibrium State at $\omega_A / P_0 = 0.12$

Figure 2.4.7a: Cont'd.

Note that in order to ensure accuracy of the computations at lease five finite element nodes span any domain wall, and the path-independence of the J-integral is verified for all cases of equilibrium.   If the mesh is too coarse then mesh-pinning of the domains occurs and significant but artificial path-dependence appears at equilibrium in the J-integral.   When the charge is fixed at $\omega_A / P_0 = 0.12$, the evolution of the domain structure at different times, from the nucleation of the domain to the final equilibrium

45

configuration, is shown in Figure 2.4.7a. Figure 2.4.7a shows contour plots of the x and y-components of the polarization normalized by P_0 in the vicinity of the crack tip. Figure 2.4.7b shows contour plots of the y-component of the polarization distributions at four different times in the domain evolution. The arrows represent the nominal polarization in different regions. This simulation illustrates that the 90° domain needle is nucleated at the crack tip and propagates through the entire domain until it reaches the charged boundary.
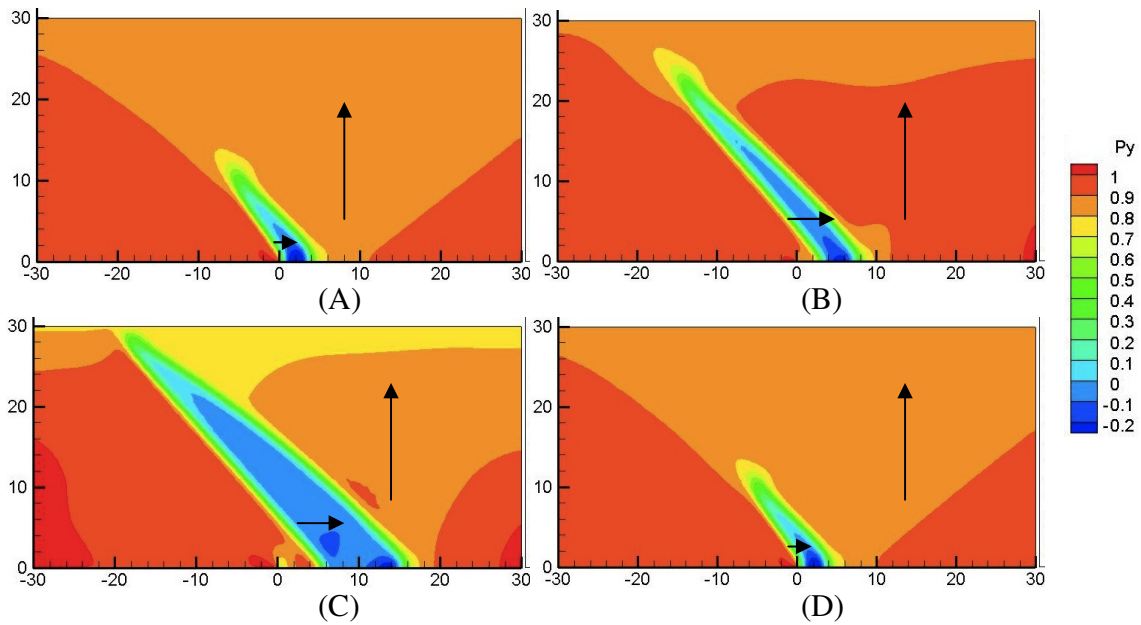
Figure 2.4.7b: Contour plots of the y-component of the polarization normalized by P_0 in the vicinity of the crack tip for (A) $\omega_A / P_0 = 0.12$ during the non-equilibrium evolution of the domain, (B) $\omega_A / P_0 = 0.12$ at the final equilibrium state for the domain, (C) equilibrium at $\omega_A / P_0 = 0.2$, and (D) equilibrium at $\omega_A / P_0 = 0.11$. Only the upper half of the model is displayed due to symmetry. The x and y distances are normalized as x/l_0 and y/l_0, and the polarization scale is normalized by the spontaneous polarization P_0. The arrows represent the nominal direction of the polarization in different regions.

46

This non-equilibrium propagation of the domain supports the hypothesis that an instability in the equilibrium solution exists at the domain nucleation threshold. Additionally, the equilibrium configurations just prior to the domain nucleation with no domain and that shown in Figure 2.4.7b (B) both occur at a charge level of $\omega_A / P_0 = 0.12$, and are sufficiently distinct from one another. This unstable growth of domains is in contrast to domain switching zones predicted using phenomenological constitutive laws (Landis, 2002a, 2003; Landis et al., 2004c; Wang and Landis, 2004, 2006) where the switching zones can grow in a stable fashion. The explanation for the difference is that these phase-field simulations assume a defect-free material. In such a material domain walls do not become pinned and are free to move at vanishingly small levels of electromechanical driving force (Xiao et al., 2005). The existence of defects and grain boundaries will likely act to hinder the propagation of domain needles.

Next, results for the crack-tip energy release rate calculation are presented. Figure 2.4.8 (a) plots the energy release rate as a function of the applied charge loading for the sample. Note that points A-D in Figure 2.4.8 (a) correspond to the domain structures illustrated in Figure 2.4.7b (A)-(D) respectively. Initially, as the charge is applied the energy release rate is negative and approximately quadratic in the applied charge. These features of the energy release rate are in accord with linear piezoelectric fracture mechanics solutions (Sosa, 1992; Pak, 1992; Suo et al., 1992).

Specifically, path-dependence of the energy release rate calculation for domain structure A is plotted as the blue curve in Figure 2.4.8 (b). Domain structure B is again an equilibrium configuration and the energy release rate calculation is path-independent. After domain structure B stabilizes, additional charge is applied and the domain structure is allowed to evolve at equilibrium to domain structure C.
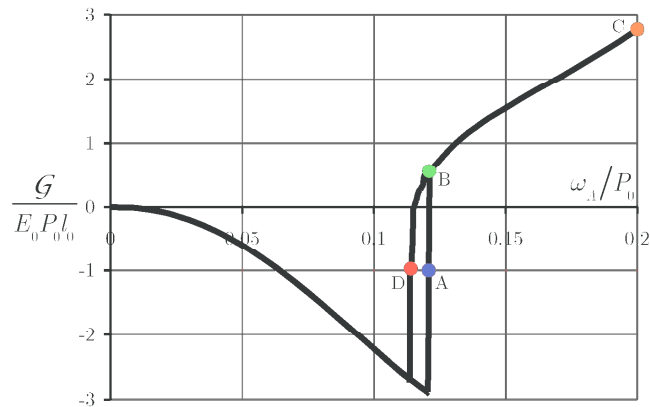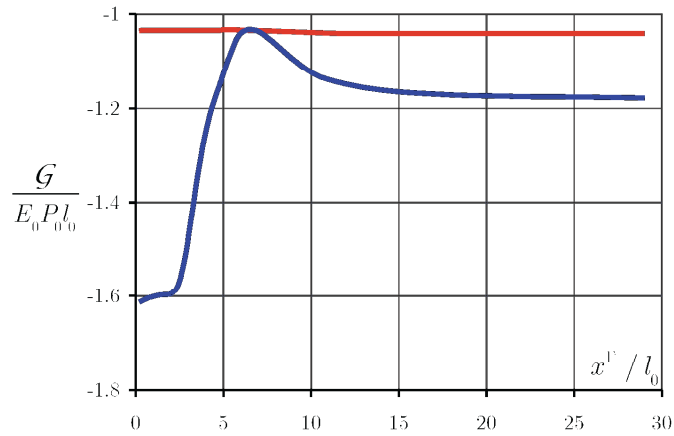
Figure 2.4.8:   (a) The crack-tip energy release rate as a function of the applied charge. Points A-D correspond to the domain structures illustrated in Figure 2.4.7b (A)-(D) respectively.   (b) The apparent energy release rate as calculated by $G_\Gamma = J_\Gamma - \omega_0 \left[\phi(x_1^+, 0) - \phi(x_1^-, 0) \right]$ for domain structures A (blue, non-equilibrium) and D (red, equilibrium).

During this loading process, the energy release rate increases in an approximately linear fashion.   Upon reaching structure C the applied charge is removed and the domain structures and the energy release rate "unload" along their original loading paths to structure B.   At this point, the unloading path diverges from the original loading path

48

and a hysteresis appears in the energy release rate versus applied charge response. Domain structure D is arrived at during the equilibrium unloading process and the energy release rate calculation is path-independent as shown by the red curve in Figure 2.4.8 (b). Further unloading of the charge causes the domain to vanish and the original negative quadratic branch of the energy release rate response is recovered.

The most interesting aspect of this simulation is the departure from the results of linear piezoelectric fracture mechanics.   Specifically, this calculation is the first that we are aware of that predicts that the crack-tip energy release rate can be positive under purely electrical loading for impermeable crack-face boundary conditions.   Furthermore, the calculation shows that an existing domain structure near the crack tip can cause a qualitatively different behavior for the energy release rate, positive and increasing with applied charge, from what is expected in linear piezoelectricity, negative and decreasing with applied charge.   A negative energy release rate implies that the energy is supplied by the crack tip fracture process when the crack propagates.   Such a scenario is difficult to envision physically.

Since the domain structure introduces spatial dependence in the material properties its effect on the energy release rate is to some degree connected with the results generated by Oates (Oates, 2005).   Oates found that by introducing a heterogeneity near the crack and using the semi-permeable crack-face boundary conditions (Hao and Shen, 1994), a positive crack-tip energy release rate could be generated by purely electrical loading when the heterogeneity is close the crack tip. In the work presented here the domain is such a heterogeneity and it is located at the crack tip. We do note that large scale switching does occur in this simulation and so a direct comparison to linear piezoelectric fracture mechanics concepts is tenuous.   However, these simulations demonstrate the effects that near tip domain structures can have on the

fracture process in ferroelectric crystals. Specifically, the negative contribution of the energy release rate from applied electric fields may in fact be positive for certain domain structures near crack tips. Hence, the modeling of crack tip domain structures and large scale domain switching behavior in facture specimens may be a key to understanding the plethora of seemingly disparate experimental observations on the electromechanical fracture of ferroelectric material.

We also investigated another unloading case where charge is applied to the surface first, then electric potential is set to be zero to unload the specimen rather than reducing the charge. Here, we studied a two-dimensional $40\,l_0 \times 60\,l_0$ region, where $40\,l_0$ is the height and $60\,l_0$ is the width. The characteristic length of domain wall is still $2\,l_0$, and the modified impermeable crack face boundary conditions are used. The crack tip is located at $(x/l_0, y/l_0) = (-10, 0)$ instead of the origin. First, the charge load is applied on the top surface as before, then a new domain structure is nucleated at the crack tip when $\omega_A / P_0 = 0.16$. Then we fix the load and let the domain evolve with a positive viscosity term, until it is very close to equilibrium. Then the viscosity term is turned off and final equilibrium state is reached. Similar as the previous simulation, the domain grows, expands, moves towards right boundary and stops by the charge layer on the top surface. Instead of unloading the specimen by reducing the charge load on the top surface, we set the electric potential on the top surface to be zero, and let the domain evolve with a viscosity term, until the equilibrium state without viscosity term. This procedure is shown in Figure 2.4.9, in which contour plots of the x (left) and y (right) component of the polarization normalized by P_0 is drawn. In the unloading procedure by reducing charge, we can see the domain needle reduces its size and moves towards left boundary, which is exactly the reverse process of the charge loading. For the zero

electric potential unloading, the domain needle stays where it was, and shrinks until finally vanishing, then the configuration is back to the initial configuration.

Domain Nucleation at $\omega_A / P_0 = 0.16$

Domain Evolution at $\omega_A / P_0 = 0.16$
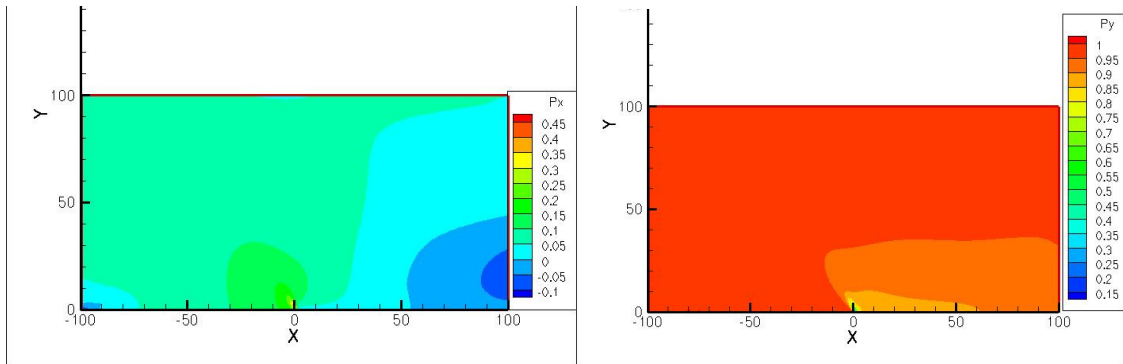

Final Equilibrium State at $\omega_A / P_0 = 0.16$
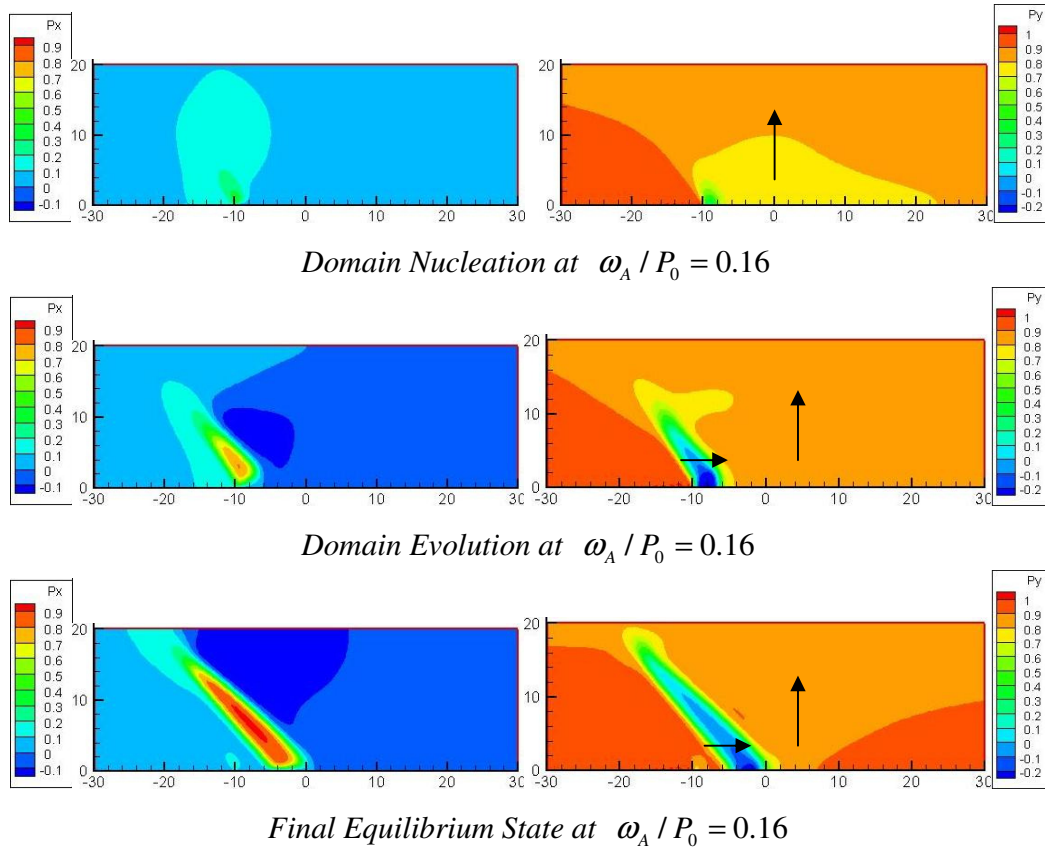
Figure 2.4.9: Contour plots of the x (left) and y (right) components of the polarization normalized by P_0 in the vicinity of the crack tip during the evolution of the domain structure with the fixed charge loading $\omega_A / P_0 = 0.16$ at different times, from the nucleation of the domain to the final equilibrium configuration, and then the electric potential on the top surface is set to be zero.   Due to symmetry, only the upper half of the model is displayed. The x and y distances are normalized as x/l_0 and y/l_0, and the polarization scale is normalized by the spontaneous polarization P_0. The arrows represent the nominal direction of the polarization in different regions.

51

Domain Evolution at $\phi_{top} = 0$

Domain Evolution at $\phi_{top} = 0$

Domain Evolution at $\phi_{top} = 0$

Final Equilibrium State at $\phi_{top} = 0$: Initial State
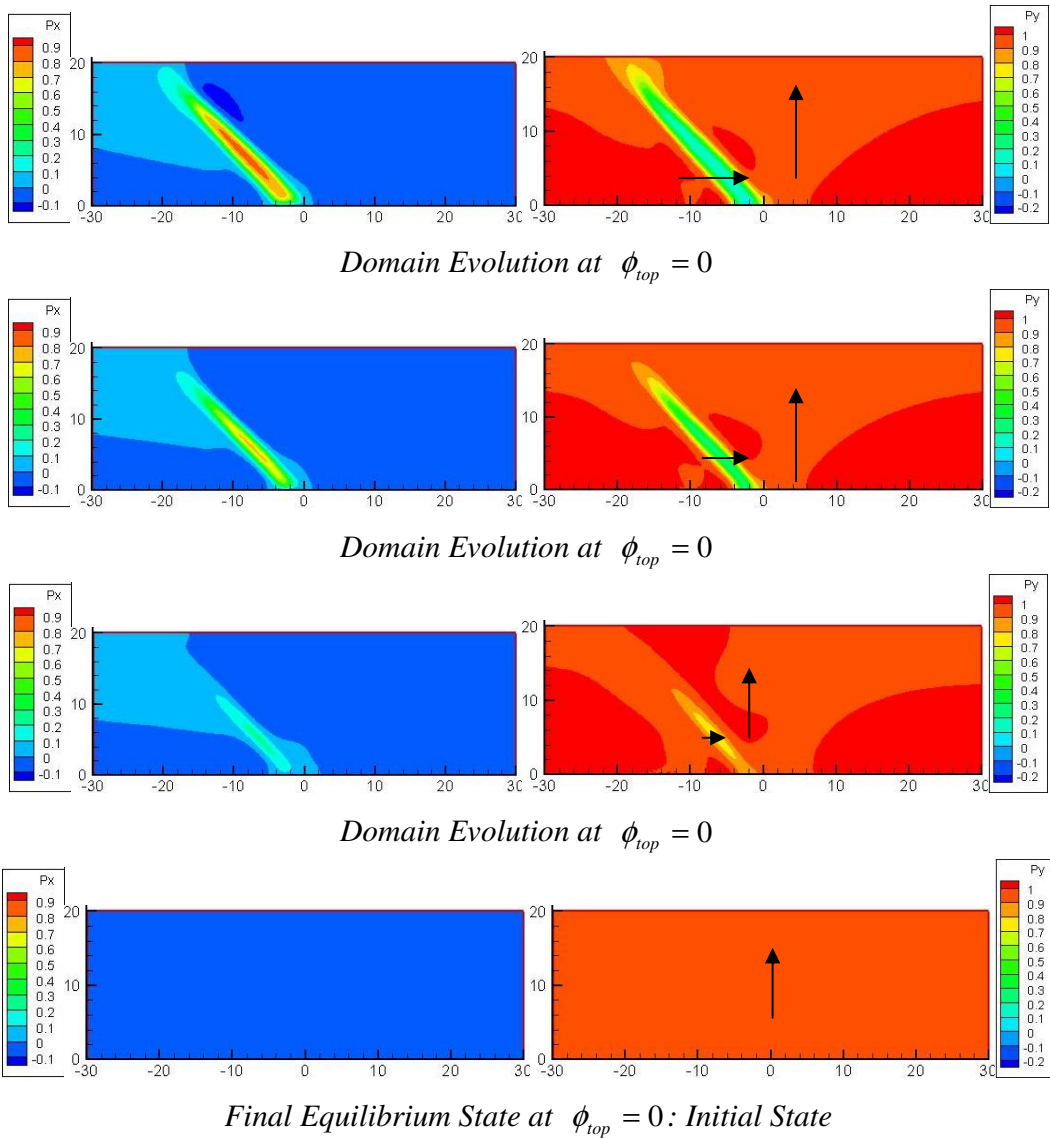
Figure 2.4.9: Cont'd.

2.4.4 Purely Electrical Loading: Controlled Electric Potential Load

In this section, the nucleation and evolution of the new domains from a crack tip during purely electrical loading, where the electric potential load on the top and bottom

surfaces is monotonically increased and then decrease is simulated. Though charge load and electric potential load are both purely electrical loading, the domain structure evolution for these two different loadings leads to different domain patterns. We still study the two-dimensional $60\,l_0 \times 60\,l_0$ and the crack length is equal to $30\,l_0$. The characteristic thickness of the domain wall is again $2\,l_0$, and the generalized impermeable boundary conditions are applied.
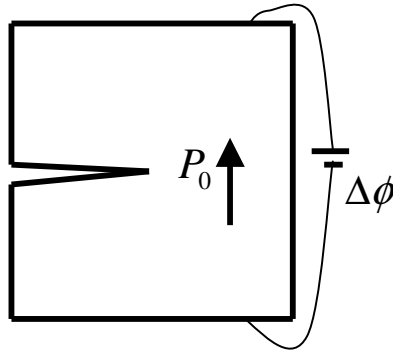
Figure 2.4.10: A schematic plot of the specimen. In this $60\,l_0 \times 60\,l_0$ domain, the entire boundary is traction free, and the left and right sides of the region have no surface charge density. The top and bottom surfaces have an applied electric potential of $\Delta\phi$.

As shown in Figure 2.4.10, the initial spontaneous polarization P_0 is normal to the crack faces. The entire boundary of the square region is traction free, and the left and right sides of the region have no surface charge density. The top and bottom surfaces are loaded by electric potential $\Delta\phi$. Note that when $\Delta\phi$ is equal to zero, it is the initial state of this simulation with $\Delta\phi = 0$, and $\sigma_{ij} = 0$, $E_i = 0$, $P_y / P_0 = 1$ in the body. Then $\Delta\phi$ is increased to apply the electric potential loading on the top and bottom surfaces.

53

When the loading is increased, the new domain is nucleated at the crack tip, similar to the case when charge is applied. Then it is allowed to evolve with a non-zero polarization viscosity term. The loading is applied by first ramping up a uniform electric potential load on top and bottom surfaces to the level $\Delta\phi/E_0 L = 32$ in a $60 l_0 \times 60 l_0$ domain (Point O-A in Figure 2.4.11(a)), where L is the vertical length of the specimen. Then the load is fixed at $\Delta\phi/E_0 L = 32$, and the domain structure is allowed to evolve until the solution is sufficiently close to the equilibrium configuration, at which point the polarization viscosity term is set to $\beta\dot{\omega}_A/E_0 = 0$, to find the final equilibrium solution (Point A-G in Figure 2.4.11(a)). Thereafter, additional potential is applied to the surface to a final value of $\Delta\phi/E_0 L = 50$ (Point G-H in Figure 2.4.11(a)) and finally the loading is removed from the surface (Point H-O' in Figure 2.4.11(a)). In Figure 2.4.11(b), the plot from O to A is presented alone to show that the apparent crack-tip energy release rate is negative and approximately quadratic in the applied electric potential as the loading is applied before the new domain is nucleated. Also, prior to the nucleation of the new domain, the solutions are for equilibrium states and the J-integral is path-independent.

As shown in Figure 2.4.11, the energy release rate remains negative under purely electrical loading when electric potential is applied to the surfaces. Prior to the nucleation of the new domain (point A), the apparent energy release rate is nearly quadratic in applied electric potential. When the domain is nucleated, polarization viscosity is introduced with fixed applied loading at $\Delta\phi/E_0 L = 32$. During the domain growth process the J-integral is not path-independent, and it cannot be used to calculate the crack tip energy release rate.

54
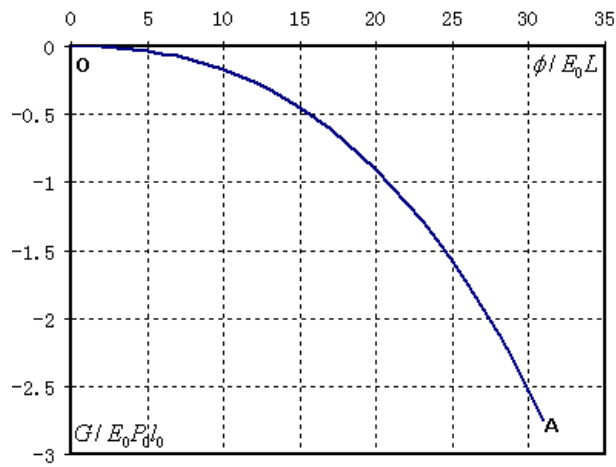
(a)
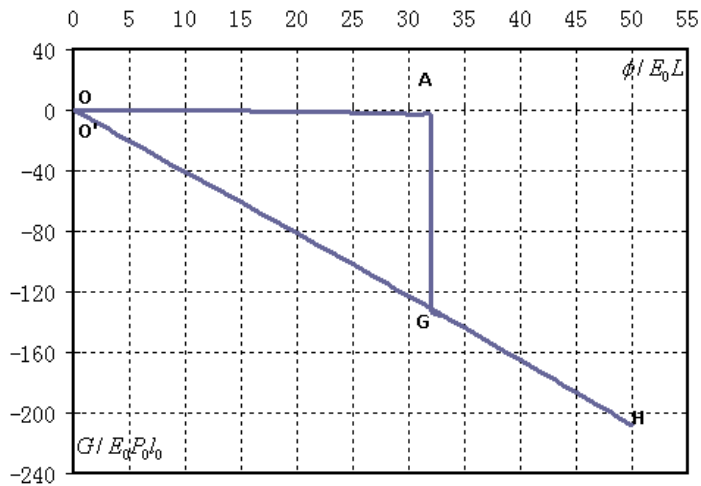
(b)

Figure 2.4.11: (a) The crack-tip energy release rate as a function of the applied electric potential. The loading path is O-A-G-H-O'. Points A-G correspond to the domain structures illustrated in Figure 2.4.11 A-G respectively. (b) The O-A segment is plotted alone to show the quadratic dependence.

When the solution is close to the final equilibrium configuration, the polarization viscosity is set to zero, and the final equilibrium state at $\Delta\phi / E_0 L = 32$ is reached (point G). At this point, the energy release rate is still negative, and its value is much larger

than the value just prior to the nucleation of new domain. From this new domain structure, when additional electric potential is applied until $\Delta\phi / E_0 L = 50$ (point H), the energy release rate will be approximately linear in the applied load. Finally, when the load is removed from the surface (point O'), the energy release rate remains a nearly linear function of the applied electric potential and returns to zero.

This simulation illustrates at the applied load level $\Delta\phi / E_0 L = 32$, the new domain structure is nucleated at the crack tip, then propagates up to the upper boundary and spreads over the electroded surface. The contour plot of the evolution of domain structure is shown in Figure 2.4.12 for (A) the nucleation state through (G) the final equilibrium state with $\Delta\phi / E_0 L = 32$. The arrows represent the nominal direction of the polarization in different regions.

In Figure 2.4.12 (A), the new domain structure is nucleated, and then grows (B). Unlike the controlled charge loading on the top surface in section 2.4.3 which prevents the new domain needle from intersecting the top surface due to the charge layer enforcing non-zero P_y on the top surface, the electric potential load does allow the domain needle to intersect and spread over the top surface since the electrode is able to redistribute the charges on it. In (C)-(F), we can observe that 90° domain walls and 180° domain walls both exist in the evolution of the domain structure with the fixed electric potential load. In the final equilibrium state (G) at $\Delta\phi / E_0 L = 32$, only 90° domain walls exists.
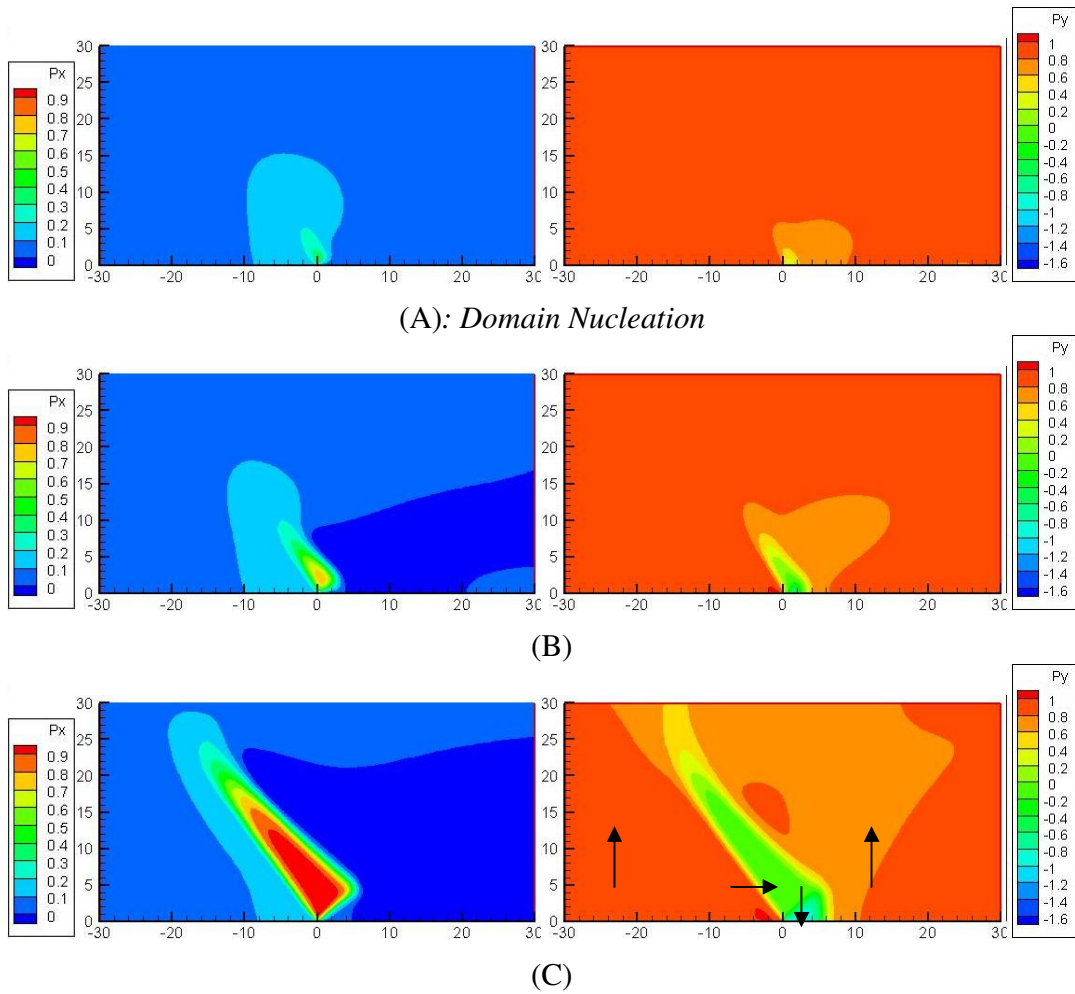
Figure 2.4.12:   Contour plots of the x-component (left) and y-component (right) of the polarization normalized by P_0 in the vicinity of the crack tip for (A) the nucleation state -- (G) the final equilibrium state at fixed electric potential load level $\Delta\phi / E_0 L = 32$.   (A)-(F) are not equilibrium states as they are obtained using a non-zero viscous term.   Only the upper half of the model is displayed due to symmetry.   The x and y distances are normalized as x / l_0 and y / l_0, and the polarization scale is normalized by the spontaneous polarization P_0.   The arrows represent the nominal direction of the polarization in different regions.
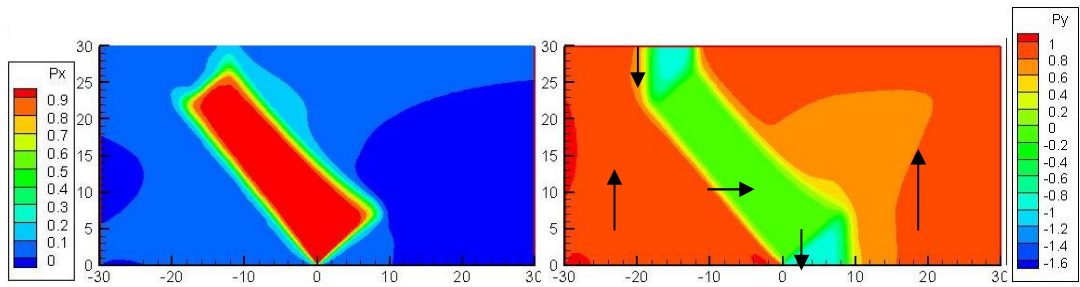
(D)
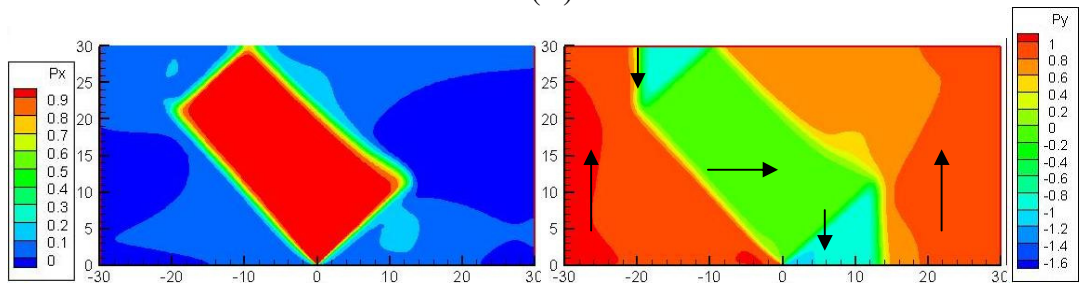
(E)
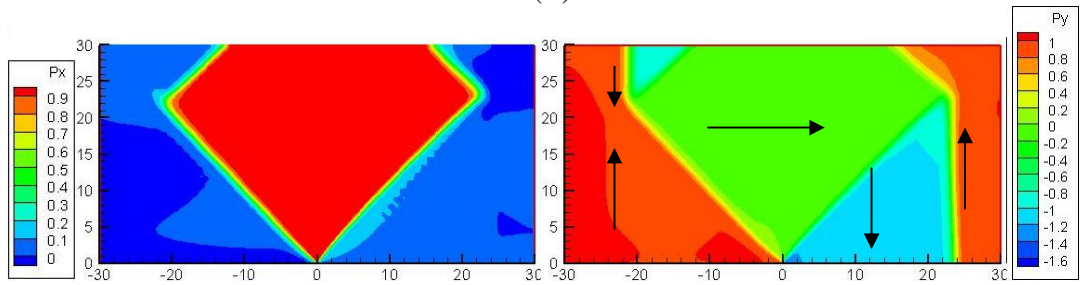
(F)
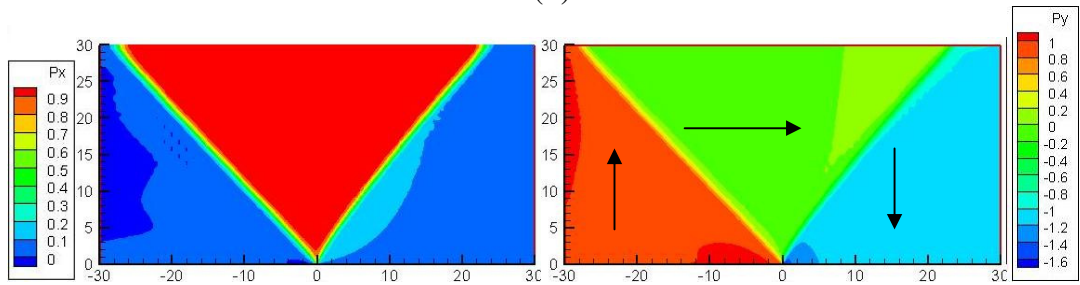
(G): *Final Equilibrium State at* $\Delta\phi/E_0L = 32$

Figure 2.4.12:   Cont'd.
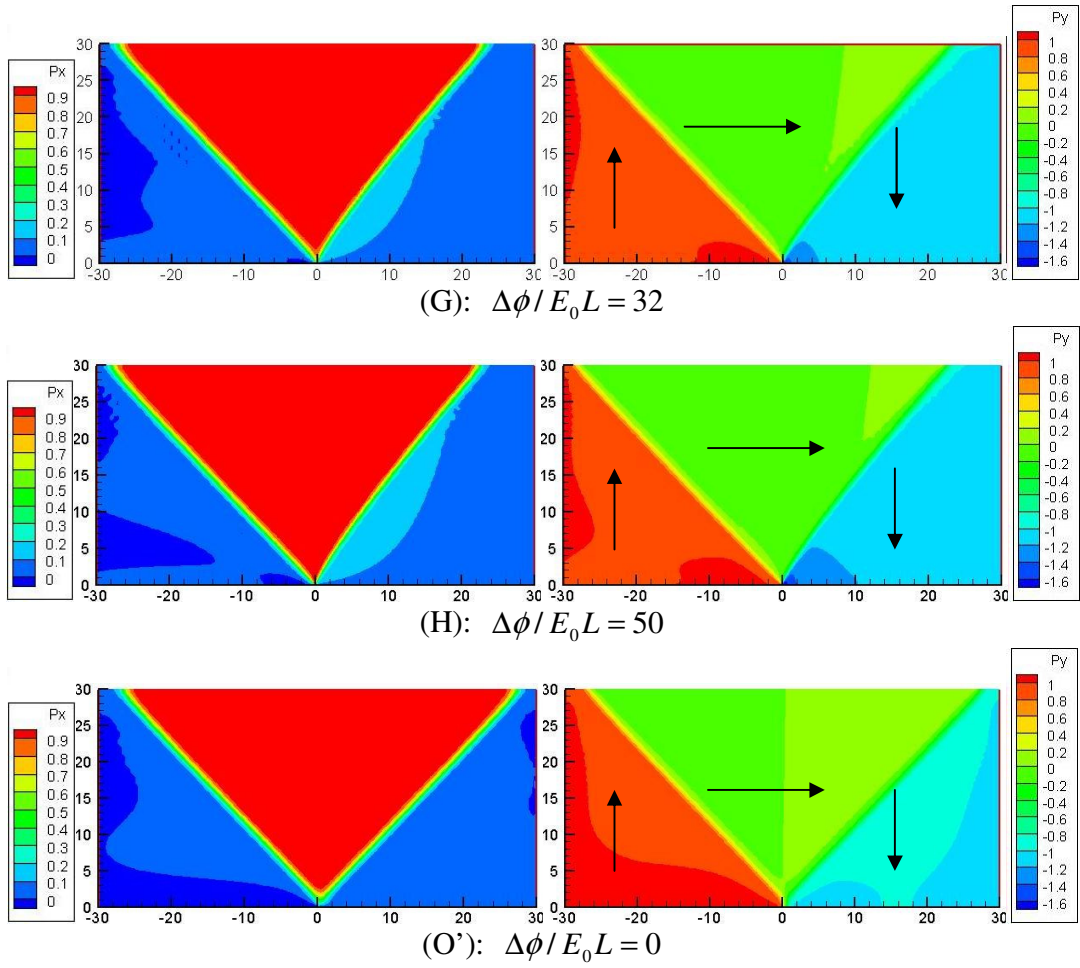
Figure 2.4.13: Contour plots of the x-component (left) and the y-component (right) of the polarization normalized by P_0 in the vicinity of the crack tip for three equilibrium states at the electric potential loads: (G) $\Delta\phi/E_0 L = 32$, (H) $\Delta\phi/E_0 L = 50$, and (O') $\Delta\phi/E_0 L = 0$. Only the upper half of the model is displayed due to symmetry. The x and y distances are normalized as x/l_0 and y/l_0, and the polarization scale is normalized by the spontaneous polarization P_0. The arrows represent the nominal direction of the polarization in different regions.

In Figure 2.4.13, contour plots of the x-component (left) and the y-component (right) of the polarization normalized by P_0 in the vicinity of the crack tip for three

59

equilibrium states at the following loads are plotted: (G) $\Delta\phi / E_0 L = 32$, (H) $\Delta\phi / E_0 L = 50$, and (O') $\Delta\phi / E_0 L = 0$. The domain structure remains approximately fixed, however, for larger $\Delta\phi$, the region of $P_y / P_0 = -1$ becomes slightly wider, which is consistent with the level of the load. At (O'), $\Delta\phi / E_0 L = 0$, the regions of $P_y / P_0 = -1$ and $P_y / P_0 = 1$ are approximately the same and at this state, the energy release rate is very close to zero.

2.4.5 Purely Electrical Loading: Controlled Charge Load on an Electrode

To further illustrate the point that different approaches to electrical loading on the top surface will give rise to different domain structures, we look at yet another type of electrical loading. Due to symmetry, we only consider the upper half region here. In section 2.4.3, a charge layer with uniform charge density resides on the top surface and the magnitude of the charge density is controlled, which requires the y-component of the electric displacement to be positive along the entire top surface; in section 2.4.4, the electric potential is controlled on the top surface, which allows any possible state of the y-component of the polarization to exist on the top surface, so that the domain needle is able to intersect the top surface and spread. In this section, the electric potential is required to be constant across the top surface, but the total surface charge instead of the potential on the top surface is controlled. This implies that the charge density can be non-uniform on the surface, which allows the domain needle to intersect the surface, while stabilizing the widening of the domain. This also implies that during the evolution of the domain structure the total charge on the electrodes must remain fixed, but they are able to move along the electrode, which in turn can cause the potential on the electrode to decrease.

60

Again, we still study the two-dimensional square geometry with the length of the side of the square equal to $60\,l_0$, and the crack length equal to $30\,l_0$. Again the characteristic thickness of a domain wall within the theory is $2\,l_0$. The generalized impermeable boundary conditions on the crack faces are still applied here. As shown in Figure 2.4.1, the initial polarization P_0 is normal to the crack faces. The entire boundary of the square region is traction free, and the left and right sides of the region have no surface charge density. The top and bottom surfaces have an applied total surface charge of $Q^{\pm} = \mp(P_0 - \omega_A) \bullet (60\,l_0)$, where $60l_0$ is the length of the top surface, and the electric potential on the top surface is forced to be uniform. The initial state is $\omega_A = 0$, and then ω_A is increased to apply the loading on the top and bottom surfaces. Here ω_A is the average charge density increment.

When the loading reaches $\omega_A / P_0 = 0.13$, the domain was nucleated at the crack tip as shown in Figure 2.4.14 (A), then allowed to evolve with a non-zero polarization viscosity term (Figure 2.4.14 (B)-(E)) with charge fixed at $\omega_A / P_0 = 0.13$, until the solution was sufficiently close to the equilibrium configuration. Then the polarization viscosity term was set to $\beta = 0$, to find the final equilibrium solution (Figure 2.4.14 (F)). Thereafter, additional charge is applied to the surface to a final value of $\omega_A / P_0 = 0.76$ (Figure 2.4.15 (F)-(K)).

Figure 2.4.14 shows contour plots of the x and y-components of the polarization distribution at different times during the domain evolution in the upper half of the specimen with fixed net electric charge load.
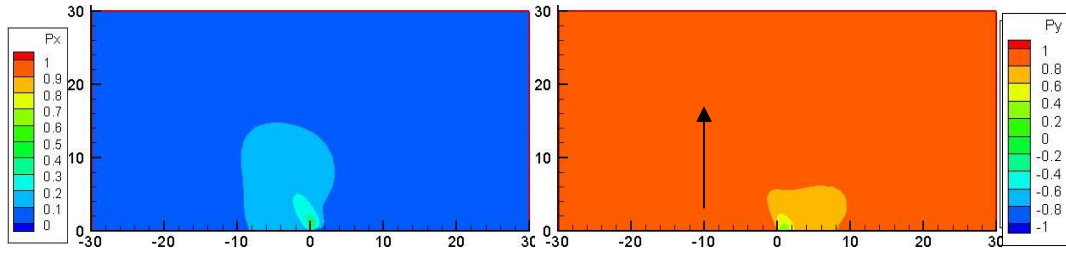
(A): *Domain Nucleation at* $\omega_A / P_0 = 0.13$
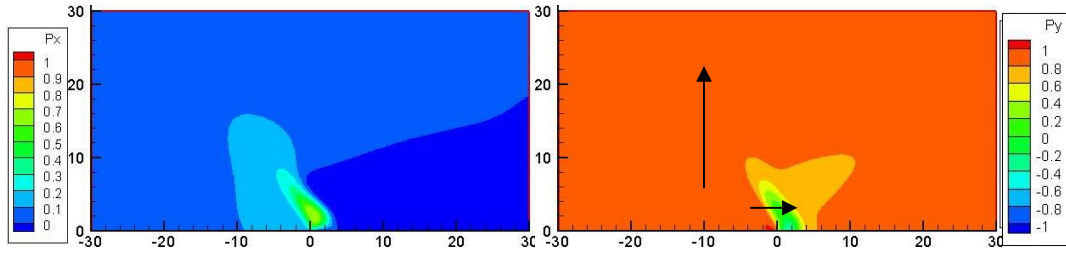
(B): *Domain Evolution at* $\omega_A / P_0 = 0.13$
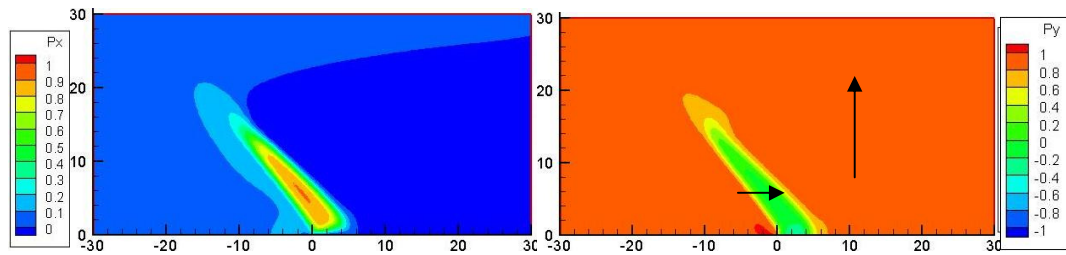
(C) : *Domain Evolution at* $\omega_A / P_0 = 0.13$

Figure 2.4.14:   Contour plots of the x-component (left) and the y-component (right) of the polarization normalized by P_0 in the vicinity of the crack tip for (A) the nucleation state -- (F) the final equilibrium state at fixed total charge load level $\omega_A / P_0 = 0.13$.   (A)-(E) are not equilibrium states as they are obtained using a non-zero viscous term.   Only the upper half of the model is displayed due to symmetry.   The x and y distances are normalized as x/l_0 and y/l_0, and the polarization scale is normalized by the spontaneous polarization P_0.   The arrows represent the nominal direction of the polarization in different regions.

62
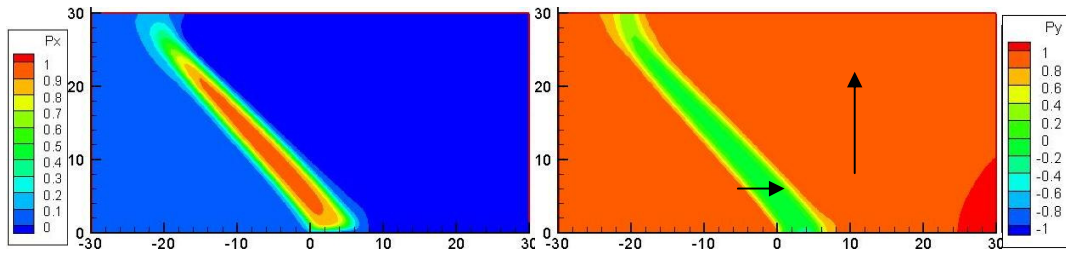
(D) : *Domain Evolution at* $\omega_A / P_0 = 0.13$
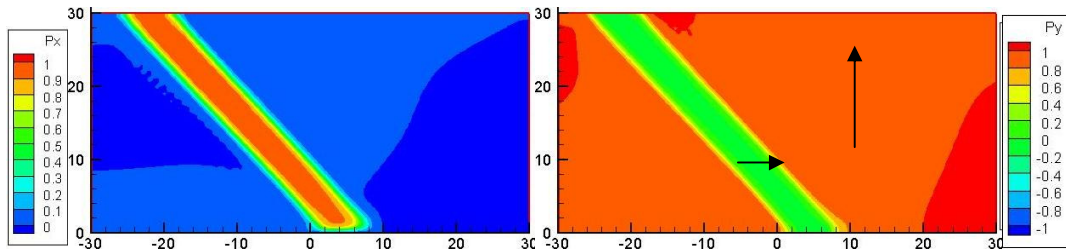
(E) : *Domain Evolution at* $\omega_A / P_0 = 0.13$
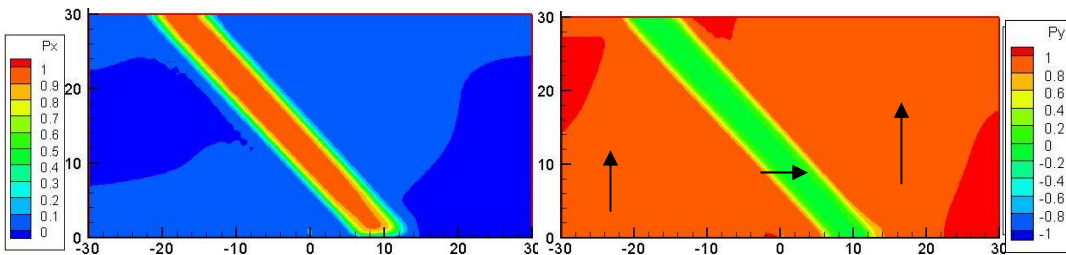
(F): *Equilibrium State at* $\omega_A / P_0 = 0.13$

Figure 2.4.14:   Cont'd.

Note that during the evolution the electric potential on the surface is allowed to change while the net charge on the surface is held fixed.   The arrows represent the nominal polarization directions in different regions.   The figure shows that the 90° domain needle is nucleated at the crack tip and propagates through the entire domain, and finally intersects the top boundary.   In contrast to the fixed potential case, the width of the domain needle is effectively restricted by the fixed net charge loading level.   After

the domain intersects the top boundary, the domain moves away from the crack tip towards the right boundary, and ultimately stops at the equilibrium state. During this process the apparent energy release rate changes significantly from initial nucleation to final equilibrium state. Before the domain is nucleated, the energy release rate is negative and shows a quadratic dependence on the applied electrical load, which is consistent with linear piezoelectricity. As the domain grows at fixed load, the J-integral is not path-independent during the non-equilibrium evolution. After the final equilibrium configuration is reached, the energy release rate jumps from a negative value to a positive value, in the same fashion as the uniform charge loading case density.

Figure 2.4.15 shows contour plots of the normalized x and y-components of the polarization distribution at different electrical load levels during the domain evolution in the upper half of the specimen. The arrows represent the nominal polarization in different regions. After the domain structure reaches equilibrium the configuration at $\omega_A / P_0 = 0.13$, if the ω_A / P_0 continues increasing, the enforcement of the positive y-component of the polarization is weaken, the domain needle with nominal $P_x / P_0 = 1, P_y / P_0 = 0$ will become wider and shift more to the right. Finally, the expanded needle reaches the right boundary, and another 90° domain wall is formed. During this process, the energy release remains positive and increasing.
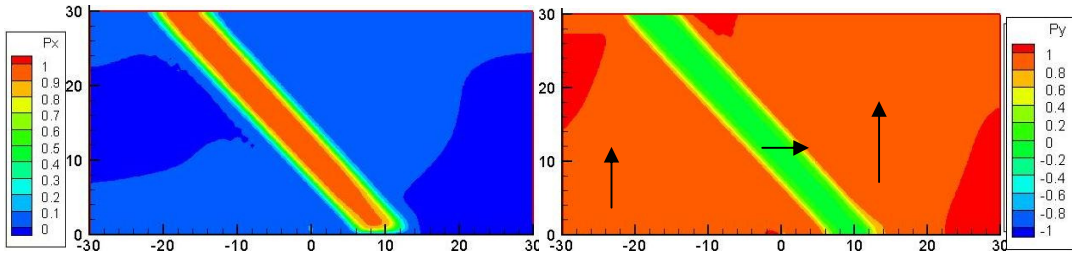
(F): $\omega_A / P_0 = 0.13$
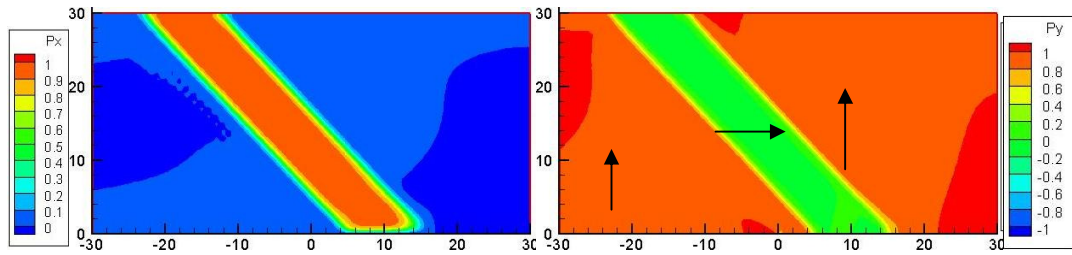
(G): $\omega_A / P_0 = 0.19$
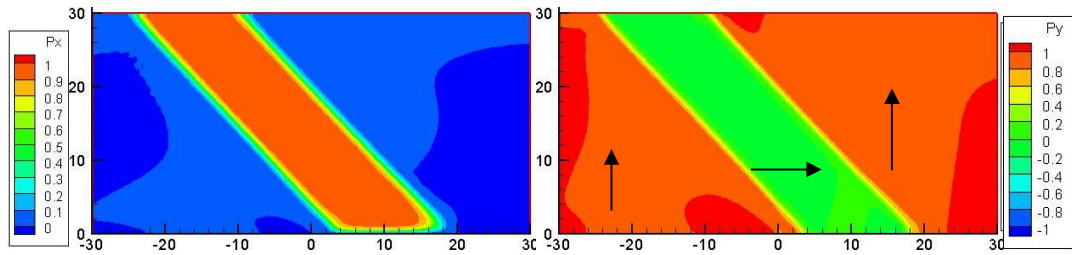
(H): $\omega_A / P_0 = 0.26$

Figure 2.4.15: Contour plots of the x-component (left) and the y-component (right) of the polarization normalized by P_0 in the vicinity of the crack tip for three equilibrium states at the total charge loads: (F) $\omega_A / P_0 = 0.13$, (G) $\omega_A / P_0 = 0.19$, (H) $\omega_A / P_0 = 0.26$, (I) $\omega_A / P_0 = 0.40$, (J) $\omega_A / P_0 = 0.50$, and (K) $\omega_A / P_0 = 0.76$. Only the upper half of the model is displayed due to symmetry. The x and y distances are normalized as x/l_0 and y/l_0, and the polarization scale is normalized by the spontaneous polarization P_0. The arrows represent the nominal direction of the polarization in different regions.

65

(I): $\omega_A / P_0 = 0.40$

(J): $\omega_A / P_0 = 0.50$

(K): $\omega_A / P_0 = 0.76$
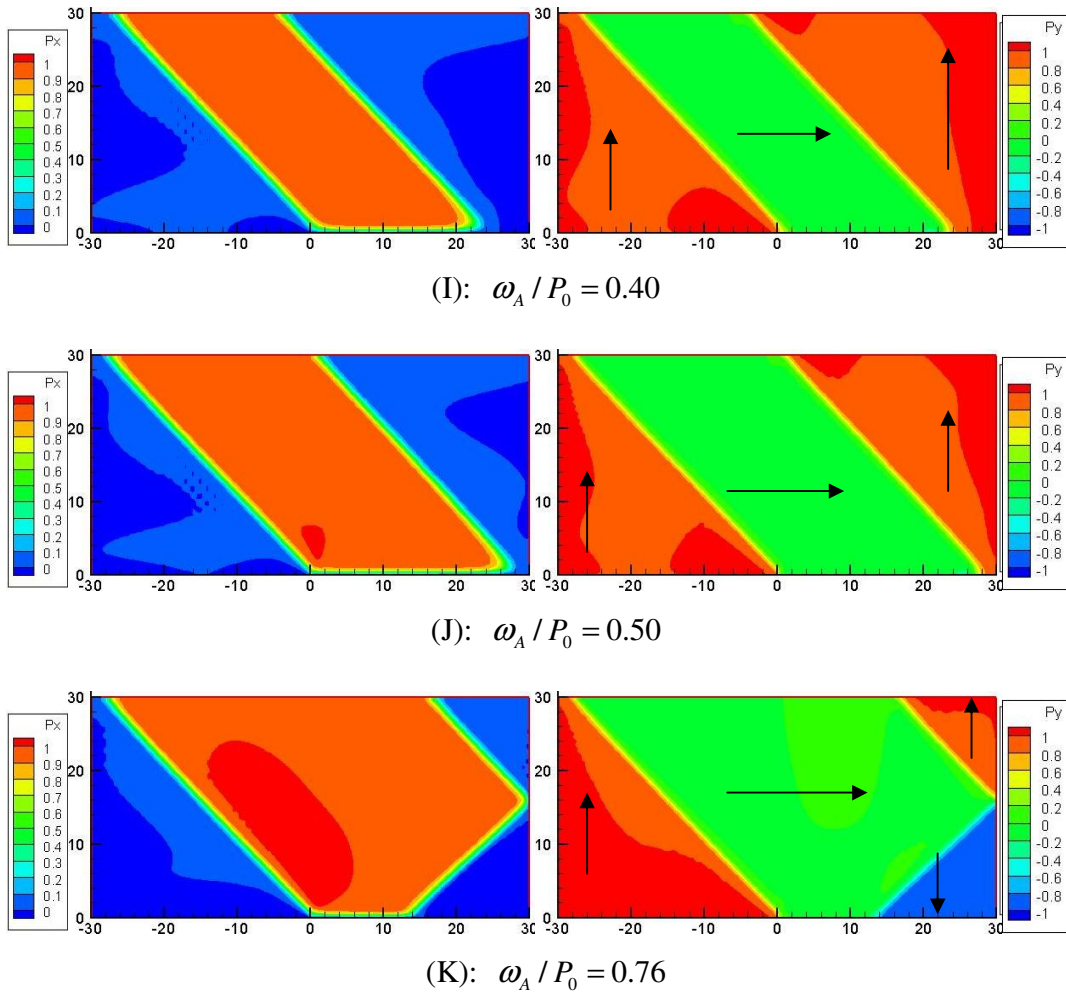
Figure 2.4.15:   Cont'd.

The energy release rate is plotted as the function of the applied charge as shown in the Figure 2.4.16.   When the applied charge increases from zero, the energy release rate is negative for purely electrical loading, and after the new domain is nucleated, the energy release rate becomes positive and increasing with the applied load, which are similar to the applied charge density loading in Section 2.4.3.   As charge is removed from the surface, the energy release rate remains positive but decreases.   When the energy release rate approaches zero, the domain structure reaches another instability point

66

and cannot achieve equilibrium without the non-zero polarization viscosity term. Here again, the polarization viscosity term is introduced and the domain structure evolves until the final equilibrium is reached. This process allows the domain structure to return back to the initial loading state and the remaining dependence of the energy release on the charge during unloading process is indistinguishable from the energy release rate during the loading process.
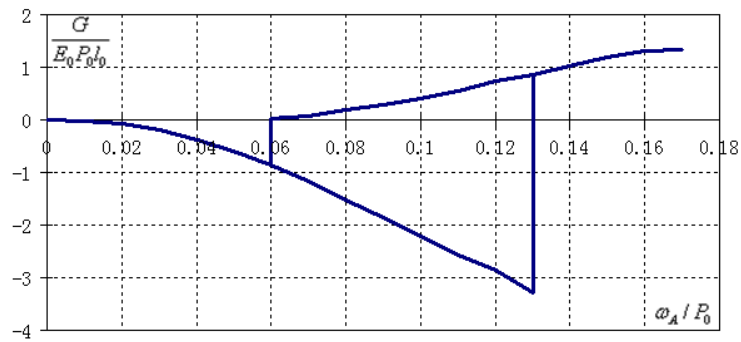
Figure 2.4.16: The energy release rate as the function of applied charge.

Comparing the response of the energy release rates with purely electrical loading for different ways of loading, we can conclude that the control of total net charge will generate a positive energy release rate after the new domain structure is formed, while the control of electric potential introduces an energy release rate that is always negative for this crack specimen geometry.

2.4.6 Combined Mechanical and Electrical Loading

The previous calculations focus on the specimen with the initial polarization perpendicular to the crack surfaces, and with purely electrical loading. In this section, we study the case with the initial polarization parallel to the crack surfaces, and the

combination of mechanical and electrical loading. Figure 2.4.17 shows a schematic plot of a two dimensional $60\, l_0 \times 60\, l_0$ domain, and the crack length is equal to $30\, l_0$. The characteristic thickness of a domain wall is $2\, l_0$. The top & bottom sides of the region have no surface charge density. The left surface has zero electric potential and the right surface has an applied surface charge density of $\omega = P_0 - \omega_A$. The crack surfaces are charge free and traction free.

First, the mechanical displacement is applied on the top surface of the region until $\Delta u = 0.01 * 30\, l_0$. Then the displacement is fixed at the level $\Delta u = 0.01 * 30\, l_0$, and ω_A is increased to apply a charge loading on the right surface to generate an opposing electric field to the initial polarization.
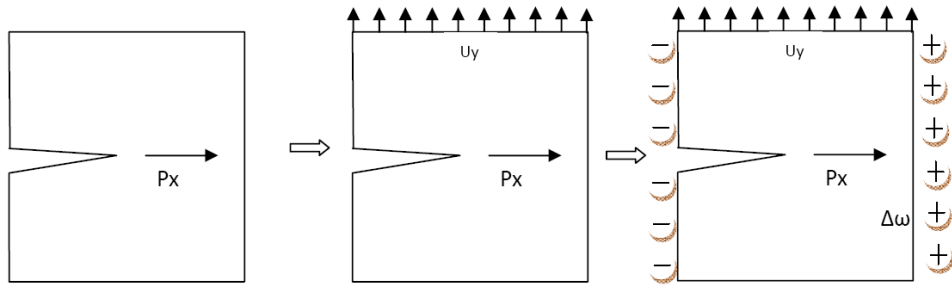
Figure 2.4.17: A schematic plot of the specimen. In this $60\, l_0 \times 60\, l_0$ domain, the entire boundary is traction free, and the top and bottom sides of the region have no surface charge density. The left surface has zero electric potential and the right surface has an applied surface charge density of $\omega = P_0 - \omega_A$. When $\omega_A = 0$, then $P_x / P_0 = 1, P_y / P_0 = 0$ is the initial state.

When the charge is increased to $\omega_A / P_0 = 0.24$, a new domain is nucleated at the crack tip, and it is allowed to evolve with a non-zero polarization viscosity term, until the solution is very close to the equilibrium configuration. At that time, the viscosity term is set to be zero, and the final equilibrium state is reached.

68
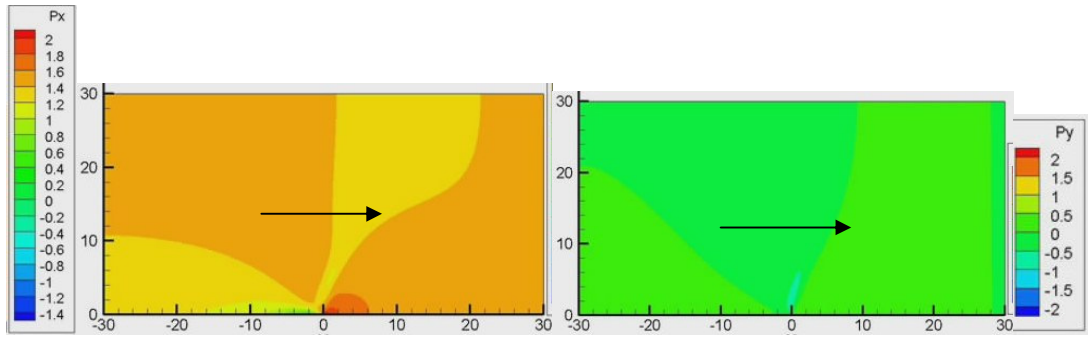
Domain Nucleation at $\omega_A / P_0 = 0.24$
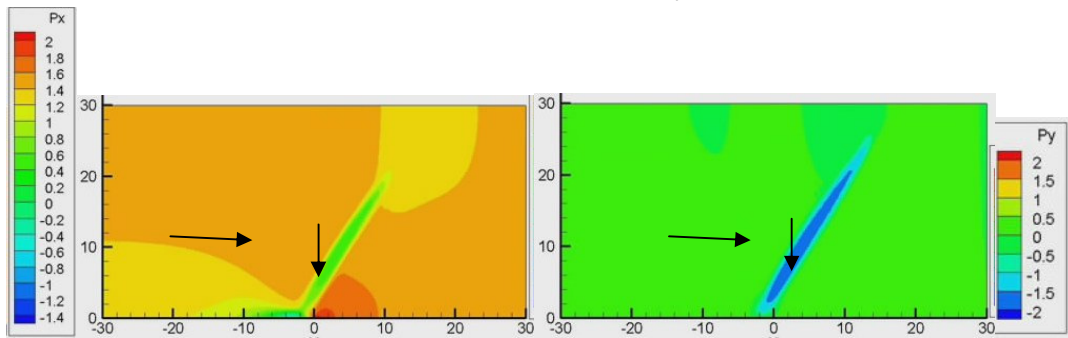
Domain Evolution at $\omega_A / P_0 = 0.24$
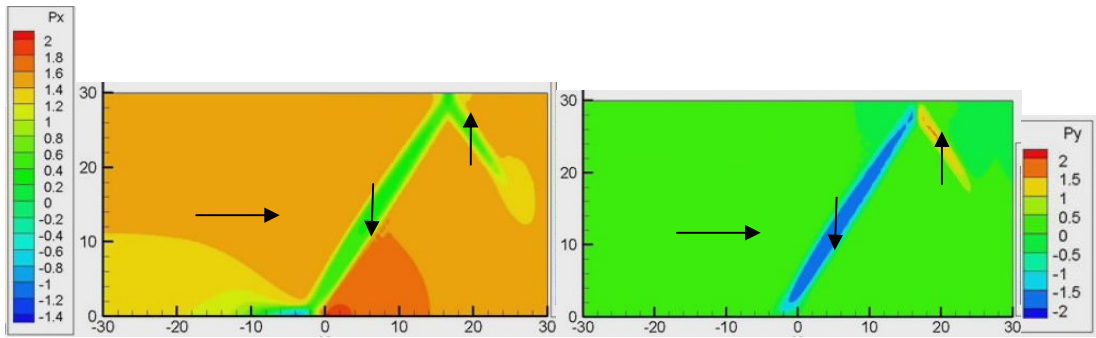
Domain Evolution at $\omega_A / P_0 = 0.24$

Figure 2.4.18: Contour plots of the x-component (left) and the y-component (right) of the polarization normalized by P_0 in the vicinity of the crack tip for different times at the fixed charge load $\omega_A / P_0 = 0.24$ and a fixed mechanical displacement load.   Only the upper half of the model is displayed due to symmetry.   The x and y distances are normalized as x/l_0 and y/l_0, and the polarization scale is normalized by the spontaneous polarization P_0.   The arrows represent the nominal direction of the polarization in different regions.

69

Domain Evolution at $\omega_A / P_0 = 0.24$

Domain Evolution at $\omega_A / P_0 = 0.24$

Domain Evolution at $\omega_A / P_0 = 0.24$

Final Equilibrium State at $\omega_A / P_0 = 0.24$

Figure 2.4.18:   Cont'd.

70
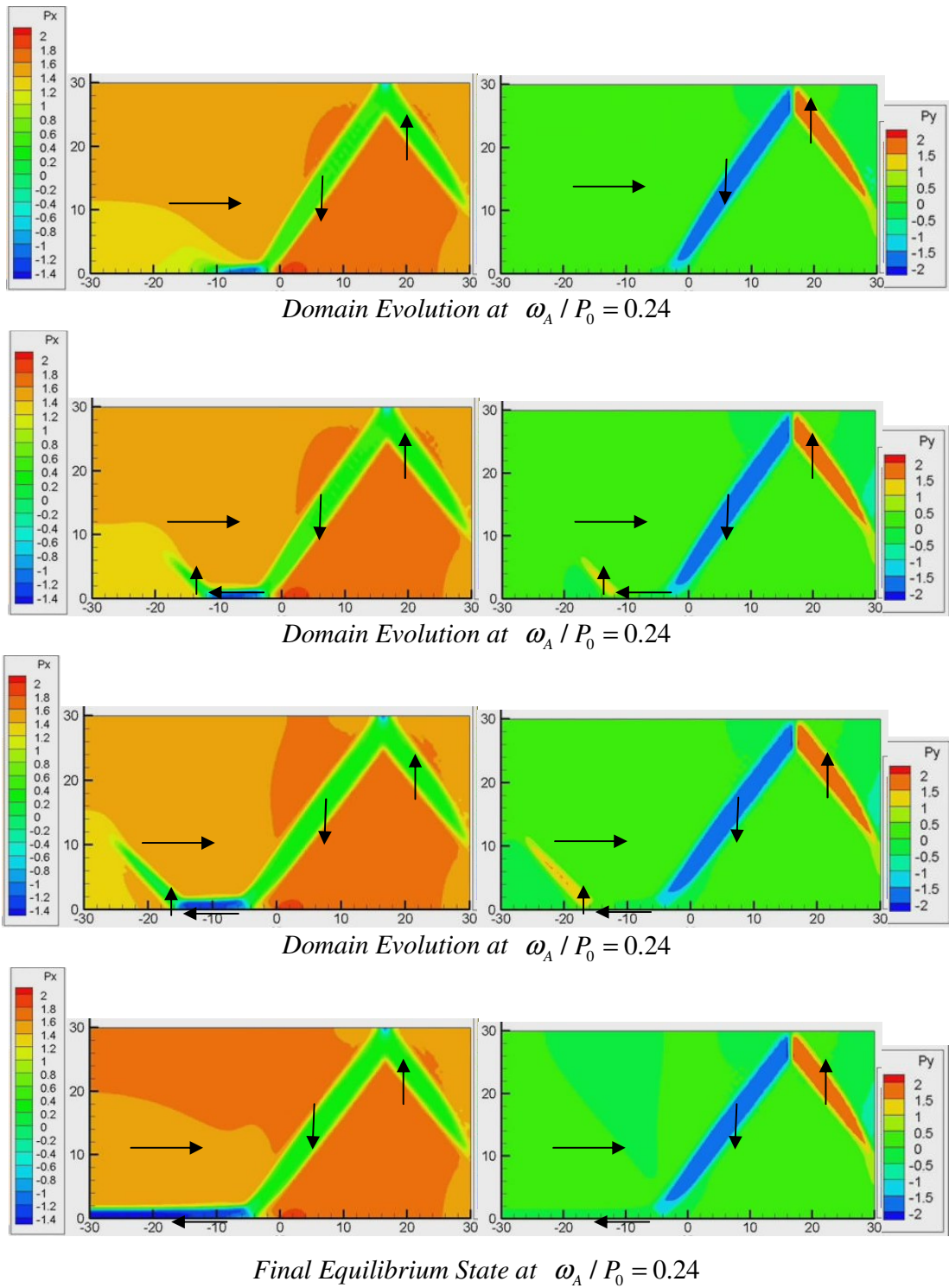
Domain nucleation and evolution until the final equilibrium state is shown in Figure 2.4.18. For this simulation, a 90° domain is first nucleated at the crack tip, and then grows towards the top surface. While the charge is fixed, the domain evolves and reaches the top surface, and "reflects", forming a 180° domain wall and a newly oriented domain. At the same time, a 180° domain grows from the crack tip to the left boundary, and finally reaches the left side of this square region. In the final equilibrium configuration, the 180° and 90° domains both exist.
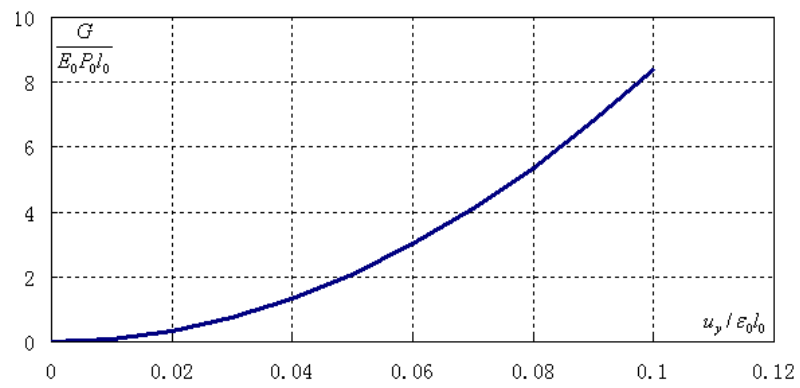
(a)
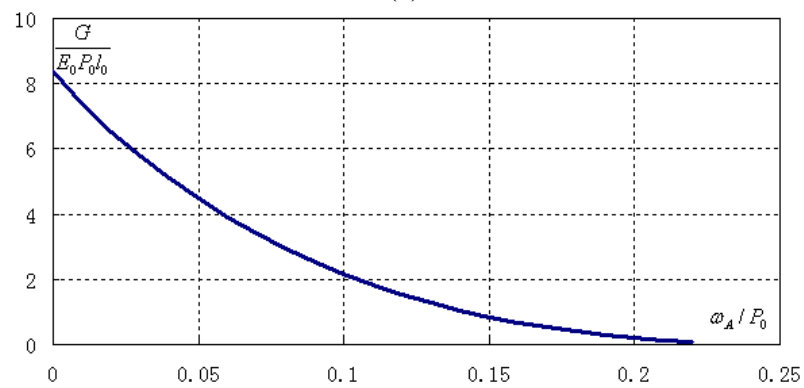
(b)

Figure 2.4.19:   (a) The crack-tip energy release rate as a function of the applied negative mechanical displacement in y-direction.   (b) The crack-tip energy release rate as a function of the applied charge before domain nucleation.

The energy release rate as the function of the applied mechanical displacement and charge are plotted during the mechanical-electrical loading in Figure 2.4.19. With purely mechanical loading by applying compressive mechanical displacement, the energy release rate is positive and increasing with the applied compressive mechanical load. When the compressive displacement is fixed on the top surface, and the net charge is applied, the energy release rate will decrease and approaches zero. At the charge loading level where the energy release rate is close to zero, the new domain structure is nucleated.

2.4.7 Evolution of a Pre-existing 180° Domain Needle

In addition to the crack studies, we also studied the growth/evolution of a 180° domain needle within a uniformly poled region. Figure 2.4.20 shows a schematic plot of a $100\,l_0 \times 200\,l_0$ domain, in which $100\,l_0$ is the width of the region and $200\,l_0$ is the height. The top and bottom sides of the region have no surface charge density. The left and the right surfaces have an applied surface charge density of $\omega = \pm(P_0 - \omega_A)$. In the majority of the region, $P_x / P_0 = 1$, $P_y / P_0 = 0$, while the center left of the region contains a 180° domain needle with $P_x / P_0 = -1$, $P_y / P_0 = 0$. We fix the charge load at $\omega_A / P_0 = 0.2$, and allow the structure to evolve. Due to symmetry, only the upper half of the model is meshed and analyzed. In the upper half region, the boundary of the domain needle is located at $x / l_0 + 8 y / l_0 \le 80$.
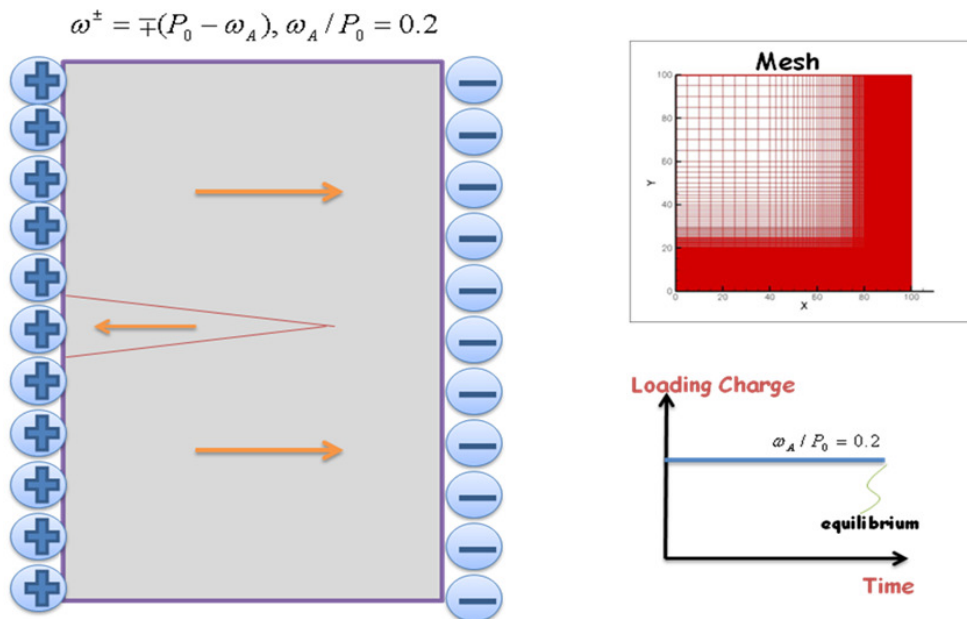
Figure 2.4.20: A schematic plot of a $100\,l_0 \times 200\,l_0$ domain, in which $100\,l_0$ is the width of the region and $200l_0$ is the height. The top & bottom sides of the region have no surface charge density. The left surface and the right surfaces have an applied surface charge density of $\omega^{\mp} = \pm(P_0 - \omega_A)$. In most of the region, $P_x/P_0 = 1$, $P_y/P_0 = 0$, and there exists a 180° domain needle with $P_x/P_0 = -1$, $P_y/P_0 = 0$. We fix the load $\omega_A/P_0 = 0.2$, and allow the structure to evolve. Due to symmetry, only the upper half of the model is modeled and analyzed. In the upper half region, the boundary of the domain needle is $x/l_0 + 8y/l_0 \leq 80$. The mesh is refined over the 180° domain needle and ahead of the needle, and is relatively coarse elsewhere.

The mesh is refined over the 180° domain needle and ahead of the needle, and is relatively coarse elsewhere. It was expected that the domain needle would grow towards the right boundary. However, significantly more complex domain patterns occurred in the simulations. Rather than a single 180° domain needle, new 90° domains form and grow, until the 90° domains reach the right boundary, and are stopped by the applied charge layer.

In addition to the charge load on the left and right boundaries, we also used mechanical constraint to control the domain structures. Here, different cases with different mechanical displacement boundary conditions are simulated.

(1) No constraint on the outer boundary

For this case the entire region is traction free on the outer boundary. Due to symmetry, we only analyze the upper half of the region.

The evolution of the domain structure with fixed charge $\omega_A / P_0 = 0.2$ is shown in Figure 2.4.21. (a) Shows the initial state with a 180° domain needle, however, note that the initial state is not an equilibrium state. Then the domain is allowed to evolve with a non-zero polarization viscosity term (b-e), and finally the polarization viscosity is set to zero to obtain the final equilibrium state (f). As time elapses, a new 90° domain forms from the tip of the domain needle, and grows towards the right boundary until the surface charge layer on this boundary constrains it. During the growth of this new 90° domain structure, the 180° domain needle retrieves back, and ultimately stops in the middle of the boundary at the equilibrium state.
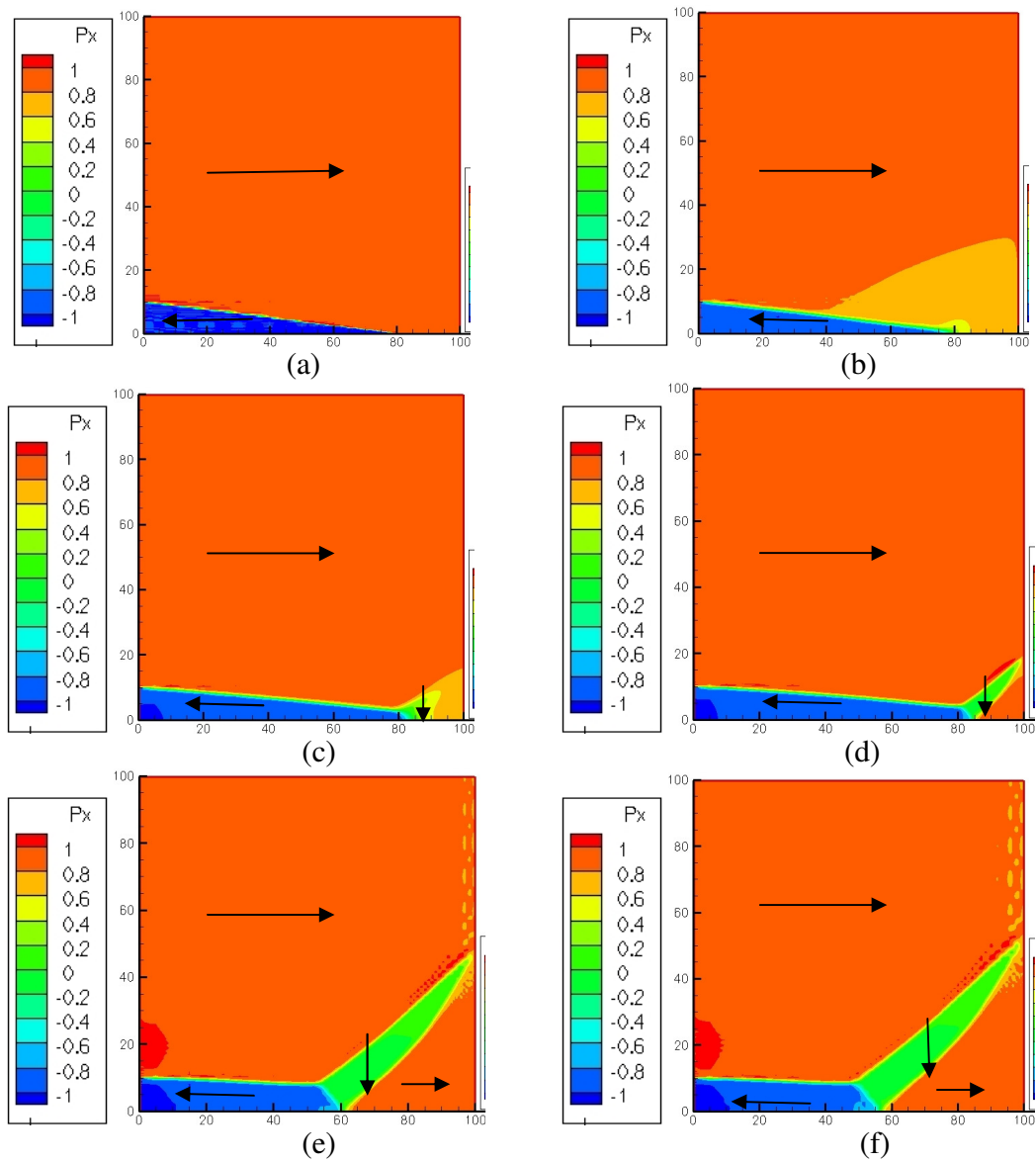
Figure 2.4.21: Contour plots of the x-component of the polarization normalized by P_0 at the fixed charge load $\omega_A / P_0 = 0.2$ without the constraint on the outer boundaries. Only the upper half of the model is displayed due to symmetry. The x and y distances are normalized as x/l_0 and y/l_0, and the polarization scale is normalized by the spontaneous polarization P_0. The arrows represent the nominal direction of the polarization in different regions. (a)-(e) are non-equilibrium states, and (f) is the final equilibrium state.

75

(2) Mechanical Constraint on the outer boundary

The simulation without constraint on the outer boundary results in a distorted right boundary.   Next, we constrain the left and the right boundaries to remain flat. Then the x-component of the mechanical displacement on the left and right surfaces are fixed, and both x and y-components of the mechanical displacements are specified and fixed on the top and bottom surfaces.   First we initialize the entire domain $P_x / P_0 = 1$, $P_y / P_0 = 0$, and find the associated stress-free strain.   The center left of the region contains a 180° domain needle with $P_x / P_0 = -1, P_y / P_0 = 0$.   Due to symmetry, only the upper half of the model is meshed and analyzed.   In the upper half region, the boundary of the domain needle is located at $x/l_0 + 8y/l_0 \leq 80$, where x and y are normalization length by l_0.   Finally, the charge load of $\omega_A / P_0 = 0.2$ is applied on the right boundary and the evolution of the domain structure is simulated.

A contour plot of the x-component of the polarization normalized by P_0 at the fixed charge load $\omega_A / P_0 = 0.2$ is shown in Figure 2.4.22.   The arrows represent the nominal direction of the polarization in different regions.   Plots (a)-(e) are non-equilibrium states, and (f) is the final equilibrium state.   In addition to the new 90° domain that nucleates from the tip of the 180° domain needle without the mechanical constraint on the outer boundary, a second 90° domain nucleates from the tip of the domain needle and grows following the first 90° domain.   The two 90° domains come to rest when the first 90° domain reaches the same location as where the 90° domain from the unconstrained case.

76
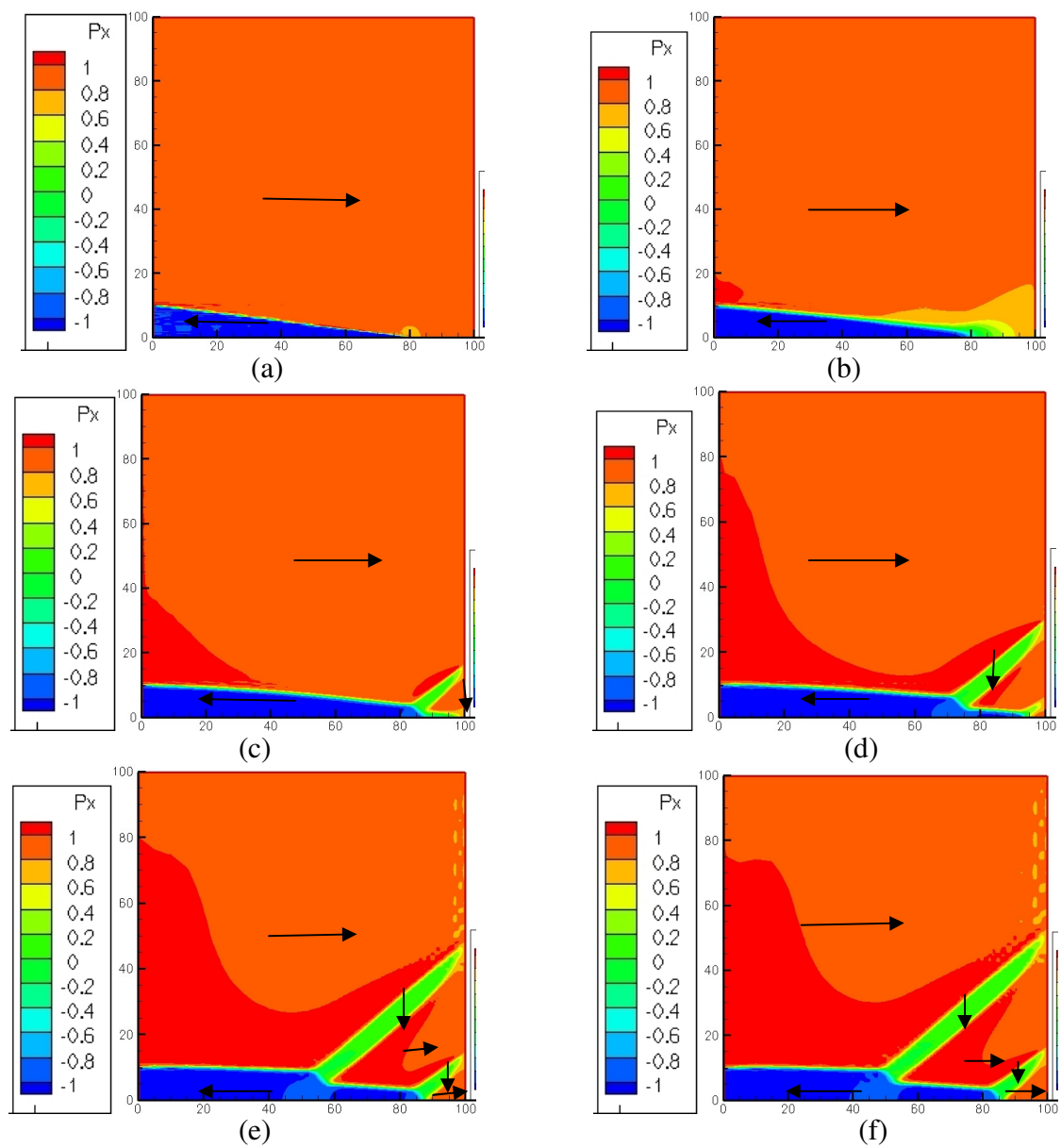
Figure 2.4.22: Contour plot of the x-component of the polarization normalized by P_0 at the fixed charge load $\omega_A / P_0 = 0.2$ with constraint on the outer boundaries. Only the upper half of the model is displayed due to symmetry. The x and y distances are normalized as x/l_0 and y/l_0, and the polarization scale is normalized by the spontaneous polarization P_0. The arrows represent the nominal direction of the polarization in different regions. (a)-(e) are non-equilibrium states, and (f) is the final equilibrium state.

If the y-component of mechanical displacement on the top surface remains negative with the magnitude to be $0.2 \times 100\, l_0 \times \varepsilon_{yy}^0 / \varepsilon_0$, and the x-component of mechanical displacement on the right boundary is positive with the magnitude $0.2 \times 100\, l_0 \times \varepsilon_{xx}^0 / \varepsilon_0$. All the remaining boundary conditions are identical with the previous case, and the domain structure is allowed to evolve with the fixed charge load of $\omega_A / P_0 = 0.2$.
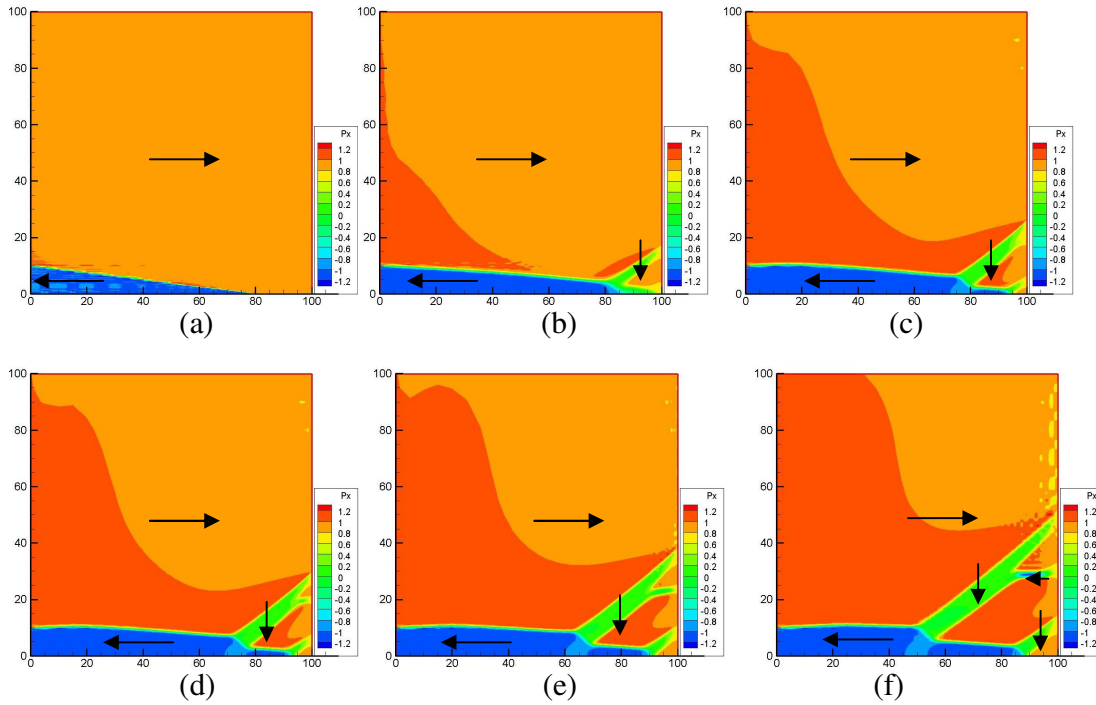
Figure 2.4.23: Contour plot of the x-component of the polarization normalized by P_0 at the fixed charge load $\omega_A / P_0 = 0.2$ with compressive displacement fixed in y direction and extensive displacement fixed in x direction on the outer boundaries. Only the upper half of the model is displayed due to symmetry. The x and y distances are normalized as x/l_0 and y/l_0, and the polarization scale is normalized by the spontaneous polarization P_0. The arrows represent the nominal direction of the polarization in different regions. (a)-(e) are non-equilibrium states, and (f) is the final equilibrium state.

The evolution of the domain structure is shown in Figure 2.4.23, in which (a)-(e) are the non-equilibrium states, and (f) is the final equilibrium state. Then we can observe another 180° domain nucleates from the first 90° domain at the final equilibrium state comparing to the previous case.

(3) Electric Potential loading

<div style="text-align:center">(a)   (b)   (c)   (d)</div>
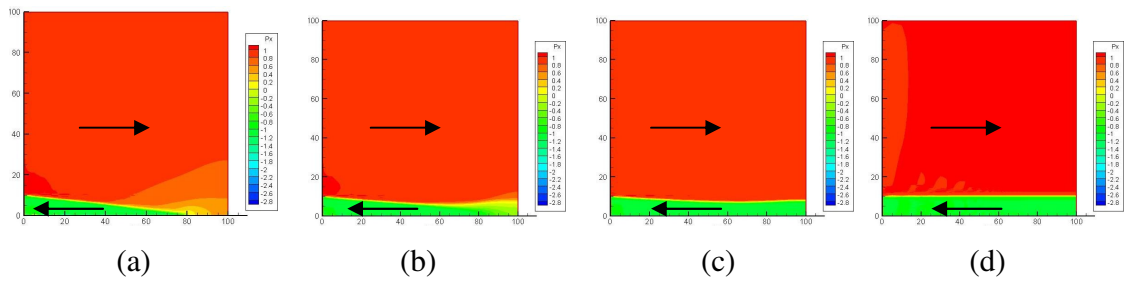
Figure 2.4.25: Contour plot of the x-component of the polarization normalized by P_0 at the fixed charge load $\omega_A / P_0 = 0.2$ on the left boundary and electric potential $\Delta\phi / E_0 l_0 = 0.4$ with compression in y direction and tension in x direction on the outer boundaries. Only the upper half of the model is displayed due to symmetry. The x and y distances are normalized as x/l_0 and y/l_0, and the polarization scale is normalized by the spontaneous polarization P_0. The arrows represent the nominal direction of the polarization in different regions. (a)-(c) are non-equilibrium states, and (d) is the final equilibrium state.

With the same geometry, if electric potential is applied on the right boundary instead of charge loading, then the domain needle spreads through the entire structure. Figure 2.4.25 shows the evolution of domain structure with the electric potential at the right boundary fixed at $\Delta\phi / E_0 L = 0.4$, and (d) is the final equilibrium state. In this case, the pre-existing 180° domain needle is able to grow and intersect the right boundary, with constraint on the outer boundary or without constraint on the outer

boundary. This occurs because there is no charge layer to constrain the domain needle from growing and intersecting the right boundary.

2.5 DISCUSSION

In this chapter, the formulation of the phase-field model for ferroelectrics is given, and the finite element method is used to implement the numerical model. To calculate the crack-tip energy release rate, a modified J-integral is used. For cases where the initial polarization has a component normal to the crack faces, a modified impermeable crack face boundary conditions is applied.

Using the phase-field theory as the modeling approach, and the finite element method as the numerical tool, we simulated the nucleation and evolution of domain structures with different geometries and different mechanical & electrical loadings in ferroelectrics. The simulations lead us to some conclusions. The J-integral is path-independence only for equilibrium states, and in these cases it can be used to calculate the apparent crack-tip energy release rate. For combinations of KI-KD loading, KD plays the primary key role in the domain nucleation. Under purely electrical loading when charge is applied directly to the surface, the apparent crack-tip energy release rate becomes positive after a 90° domain nucleates and grows to an equilibrium configuration. Such positive energy release rates do not occur in linear piezoelectric fracture mechanics from purely electrical loading.

Also, in this charge loading case, we observe that the 90° domain needle expands and moves towards the right boundary of the square region. This situation gives us some hints that another new domain structure might nucleate at the crack tip and grow towards the direction of the first domain needle. However, for the case in section 2.4.3,

when the charge load on the top surface is increased, the 90° domain needle simply expands to balance the new charges, and no new domain is nucleated from the crack tip. We also tested several other scenarios, such as using a specimen with a larger height to length ratio to determine if the first domain would move father from the tip allowing for the nucleation of another new domain. However, none of the cases that we investigated gave rise to a second domain being nucleated from the crack tip. Rather than a second domain nucleating from the crack tip, the simulations show that new domains nucleate from the other locations as the electrical loading is increased.

Chapter III   Finite Deformation Phase-Field Modeling

In the previous chapter, the assumptions associated with a linear kinematics deformation-displacement description are made throughout the calculations.   The small deformation assumption is prevalent in phase-field modeling literature.   This simplification allows the electrical forces on the material and the associated Maxwell stresses that are induced by long-range electrical interactions to be neglected.   In this chapter, finite deformations will be incorporated into the phase-field theory to account for such electrical forces.   For the dissipation associated with polarization changes, an objective rate of polarization is used to make the dissipation frame indifferent.   The problem of domain nucleation from a crack tip is modeled with the theory and we find that the resulting domain structure evolution does not differ significantly from the linear kinematics theory.   In order to study a problem where finite deformations are critical for the analysis, the theory is used in Chapter 4 where dielectric elastomers materials are introduced.   These materials can be used in electrically driven actuator devices, manipulators and energy harvesters.   In Chapter 4 the instabilities in dielectric elastomer composites are investigated..

3.1 FINITE DEFORMATION THEORY

In Chapter 2, a phase-field model using the assumptions of linear kinematics was presented.   Such theories assume that the electrical forces that exist in ferroelectric materials can be neglected as higher order terms.   In this chapter, a general finite deformation theory for phase-field modeling of ferroelectrics is presented.   Standard index notation is used with summation implied over repeated indices.   Lowercase

indices represent quantities in current state while uppercase indices represent quantities in reference state.

Consider two nearby material particles *P* and *Q* within an object with position vectors $\mathbf{X}$ and $\mathbf{X} + \mathbf{dX}$ respectively in the undeformed or reference configuration. After deformation these particles move to the positions *p* and *q* with position vectors $\mathbf{x}$ and $\mathbf{x} + \mathbf{dx}$ respectively in the deformed or current configuration. To describe the history of deformation of the body, $\mathbf{x}$ can be written as a function of the two independent variables, the reference material particle position $\mathbf{X}$ and time t, $\mathbf{x} = \mathbf{x}(\mathbf{X}, t)$. The deformation gradient tensor $\mathbf{F}$ is then defined as,

$$F_{iK} = \frac{\partial x_i(\mathbf{X}, t)}{\partial X_K} \tag{3.1}$$

This deformation gradient tensor $\mathbf{F}$ is a linear operator mapping the vector between the two differentially separated material particles P and Q in the reference state, $\mathbf{dX}$, to the vector connecting the same two material particle p and q in the current state, $\mathbf{dx}$. The tensor $\mathbf{F}$ is generally not symmetric, and represents both stretching and rotation. The determinant of the deformation gradient tensor, also called the Jacobian of the deformation $J = \det(\mathbf{F})$ describes the volume change between the reference state and current state, i.e. $dv = \det(\mathbf{F}) \bullet dV$.

Ultimately we are interested in numerical solutions for the phase-field theory using finite deformation kinematics. With this goal in mind we develop the governing equations of the theory with respect to the reference configuration. First, consider mechanical equilibrium.

$$\int_{S_0} \tilde{t}_i dS_0 + \int_{V_0} \tilde{b}_i dV_0 = 0 \qquad (3.2)$$

Here we have introduced the Cartesian components of the reference traction $\tilde{t}_i$ with dimensions of force per unit reference area, and the reference body force $\tilde{b}_i$ with dimension of force per unit reference volume. Next we introduce the first Piola-Kirchoff stress tensor s_{Ji}, which is linked to the reference traction such that

$$\tilde{t}_i = s_{Ji} N_J \quad \text{on } S_0. \qquad (3.3)$$

Here N_J are the Cartesian components of the unit vector normal to the reference surface S_0. Application of the divergence theorem to the integral form of the equilibrium equation and recognizing that this equation must be valid for any arbitrary volume of the material provides the point-wise form for the equilibrium equation as,

$$s_{Ji,J} + \tilde{b}_i = 0 \quad \text{in } V_0. \qquad (3.4)$$

Next consider the equations of electrostatics. The spatial electric field components E_i are related to the electric potential ϕ as,

$$E_i = -\phi_{,i} \qquad (3.5)$$

Of interest for finite deformation theories is the reference electric field $\tilde{E}_I$, which is defined in the following equation and related to the spatial electric field as,

$$\tilde{E}_J = -\phi_{,J} = -\frac{\partial \phi}{\partial x_i}\frac{\partial x_i}{\partial X_J} = E_i F_{iJ} \tag{3.6}$$

Note that the reference electric field is an objective measure of the electric field that can be used to characterize the electric field acting on the material in free energy functions and constitutive relations. Next, consider Gauss's law in integral form. Gauss's law states that the flux of the electric displacement through a closed surface is equal to the free charge enclosed by the surface.

$$\int_S D_i n_i \, dS = \int_S \underbrace{D_i J F_{Ji}^{-1}}_{\tilde{D}_J} N_J \, dS = \int_{V_0} \tilde{q} \, dV_0 \tag{3.7}$$

Here we have identified the reference electric displacement $\tilde{D}_J$ and the reference free charge density $\tilde{q}$ as the free charge per reference volume. Note that the reference electric displacement and the reference electric field are work conjugate quantities such that,

$$\int_V E_i D_i \, dV = \int_{V_0} \tilde{E}_J \tilde{D}_J \, dV_0 \tag{3.8}$$

Finally, the application of the divergence theorem to Gauss's law and the recognition that the result holds for any arbitrary volume yields,

$$\tilde{D}_{J,J} - \tilde{q} = 0 \quad \text{in } V_0. \tag{3.9}$$

85

Gauss's law can also be applied to a "pillbox" around a surface element to yield a relationship between the reference electric displacement and the reference surface charge per unit reference area $\tilde{\omega}$ as,

$$\tilde{D}_J N_J = -\tilde{\omega} \quad \text{on } S_0.$$ (3.10)

Our final balance laws for the phase-field theory are for the micro-forces. Paralleling the description of mechanical equilibrium we introduce the previously described micro-forces (see Chapter 2) in their associated reference forms, $\tilde{\pi}_i$ and $\tilde{\gamma}_i$, along with a "first Piola-Kirchoff" micro-force tensor $\tilde{\xi}_{Ji}$, where $\tilde{\xi}_{Ji} = J F_{Jk}^{-1} \xi_{ki}$. Then, the micro-force balance in referential form is,

$$\int_{S_0} \tilde{\xi}_{Ji} N_J dS_0 + \int_{V_0} \tilde{\pi}_i dV_0 + \int_{V_0} \tilde{\gamma}_i dV_0 = 0 \quad \Rightarrow \quad \tilde{\xi}_{Ji,J} + \tilde{\pi}_i + \tilde{\gamma}_i = 0 \quad in \quad V_0.$$ (3.11)

With the similar process in section 2.1, the Helmholtz free energy of the material including the free space occupied by the material is assumed to take the form:

$$\psi = \psi(F_{iJ}, \tilde{D}_I, P_i, P_{i,J})$$ (3.12)

where F_{iJ} is the deformation gradient tensor, $\tilde{D}_I$ is the electric displacement in reference state, P_i is the material polarization, and $P_{i,J}$ is the derivation of the material polarization P_i with respect to X_J coordinate.

Once again considering isothermal processes below the Curie temperature, the second law of thermodynamics is written as the Clausius-Duhem inequality as

$$\int_{V_0} \dot{\tilde{\psi}} dV_0 \le \int_{V_0} (\tilde{b}_i \dot{x}_i + \phi \dot{\tilde{q}} + \tilde{\gamma}_i \dot{P}_i) dV_0 + \int_{S_0} (\tilde{t}_i \dot{x}_i + \phi \dot{\tilde{\omega}} + \tilde{\xi}_{Ji} N_J \dot{P}_i) dS_0 \qquad (3.13)$$

Substitution into this inequality of the balance laws for equilibrium, Gauss's law, and micro-force, along with the application of the divergence theorem yields

$$\dot{\tilde{\psi}} \le s_{Ji} \dot{F}_{iJ} + \tilde{E}_I \dot{\tilde{D}}_I + \tilde{\xi}_{Ji} \dot{P}_{i,J} - \tilde{\pi}_i \dot{P}_i \qquad (3.14)$$

This form for the dissipation inequality suggests taking the following dependencies for the Helmholtz free energy per unit reference volume,

$$\tilde{\psi} = \tilde{\psi}(F_{iJ}, \tilde{D}_I, P_i, P_{i,J}, \dot{P}_i) \qquad (3.15)$$

Then, at first glance, the analysis of the inequality implies

$$s_{Ji} = \frac{\partial \tilde{\psi}}{\partial F_{iJ}}, \quad \tilde{E}_I = \frac{\partial \tilde{\psi}}{\partial \tilde{D}_I}, \quad \tilde{\xi}_{Ji} = \frac{\partial \tilde{\psi}}{\partial P_{i,J}}, \quad \tilde{\pi}_i = -\frac{\partial \tilde{\psi}}{\partial P_i} - \beta_{ij} \dot{P}_j \qquad (3.16)$$

Note that Equation (3.16a-c) are rigorously valid, however Equation (3.16d) is simply one possible choice that can be taken to satisfy the inequality. However, we will note here that this choice does not satisfy objectivity for the material dissipation.

For the finite element method it is useful to define virtual work quantities. The internal virtual work (IVW) and internal virtual dissipation work can be written as

$$IVW = \int_{V_0} s_{Ji} \delta F_{iJ} + \tilde{E}_I \delta \tilde{D}_I + \tilde{\xi}_{Ji} \delta P_{i,J} + \tilde{\eta}_i \delta P_i \, dV_0$$
$$IVD = \int_{V_0} \beta_{ij} \dot{P}_j \delta P_i \, dV_0 \qquad (3.17)$$

87

In order to implement the electric potential as a nodal variable for the finite element method we will utilize the electrical enthalpy per unit reference volume $\tilde{h}$, which can be derived from a Legendre transformation

$$\tilde{h} = \tilde{\psi} - \tilde{E}_I \tilde{D}_I \tag{3.18}$$

In order to mimic the small deformation theory of Chapter 2, the electrical enthalpy $\tilde{h}$ is given in the following form

$$
\begin{aligned}
\tilde{h}(\tilde{\varepsilon}_{IJ}, \tilde{P}_I, \tilde{P}_{I,J}, \tilde{E}_I) &= \tilde{\psi} - \tilde{E}_I \tilde{D}_I \\
&= \frac{1}{2} a_{IJKL} \tilde{P}_{I,J} \tilde{P}_{K,L} \\
&\quad + \frac{1}{2} \bar{a}_{IJ} \tilde{P}_I \tilde{P}_J + \frac{1}{4} \bar{\bar{a}}_{IJKL} \tilde{P}_I \tilde{P}_J \tilde{P}_K \tilde{P}_L + \frac{1}{6} \bar{\bar{\bar{a}}}_{IJKLMN} \tilde{P}_I \tilde{P}_J \tilde{P}_K \tilde{P}_L \tilde{P}_M \tilde{P}_N + \frac{1}{8} \bar{\bar{\bar{\bar{a}}}}_{IJKLMNRS} \tilde{P}_I \tilde{P}_J \tilde{P}_K \tilde{P}_L \tilde{P}_M \tilde{P}_N \tilde{P}_R \tilde{P}_S \\
&\quad + b_{IJKL} \tilde{\varepsilon}_{IJ} \tilde{P}_K \tilde{P}_L + \frac{1}{2} c_{IJKL} \tilde{\varepsilon}_{IJ} \tilde{\varepsilon}_{KL} + f_{IJKLMN} \tilde{\varepsilon}_{IJ} \tilde{\varepsilon}_{KL} \tilde{P}_M \tilde{P}_N + g_{IJKLMN} \tilde{\varepsilon}_{IJ} \tilde{P}_K \tilde{P}_L \tilde{P}_M \tilde{P}_N \\
&\quad - \frac{1}{2} \kappa_0 J C_{IJ}^{-1} \tilde{E}_I \tilde{E}_J - J C_{IJ}^{-1} \tilde{E}_I \tilde{P}_J
\end{aligned}
\tag{3.19}
$$

In the last line of the Equation (3.19), the factor JC_{IJ}^{-1} is from the transformation

$$
\int_V \frac{1}{2} \kappa E_i E_i + E_i P_i \, dV = \int_{V_0} \left(\frac{1}{2} \kappa \underbrace{(F_{iJ} E_i)}_{\tilde{E}_J} \underbrace{(F_{lK} E_l)}_{\tilde{E}_K} \underbrace{F_{Jm}^{-1} F_{Km}^{-1}}_{C_{JK}^{-1}} + \underbrace{(F_{iJ} E_i)}_{\tilde{E}_J} \underbrace{(F_{lK} P_l)}_{\tilde{P}_K} \underbrace{F_{Jm}^{-1} F_{Km}^{-1}}_{C_{JK}^{-1}} \right) J \, dV_0
$$

The 2nd Piola-Kirchoff stress, and the invariant descriptions of electric displacements, micro-forces are derived as

88

$$\tilde{T}_{JI} = \frac{\partial h}{\partial \tilde{\varepsilon}_{IJ}}, \quad \tilde{D}_I = -\frac{\partial h}{\partial \tilde{E}_I}, \quad \bar{\xi}_{JI} = \frac{\partial h}{\partial \tilde{P}_{I,J}}, \quad and \quad \tilde{\eta}_I \equiv \frac{\partial h}{\partial \tilde{P}_I} \tag{3.20}$$

Notice that while $\tilde{E}_I$ and $\tilde{D}_I$ are invariant descriptions of electric field and electric displacement for rigid body rotations of the material, the deformation gradient F_{kI}, the polarization P_i and the reference gradient of the polarization $P_{i,J}$ are not objective measures. In order to model the ferroelectric material described in Chapter 2 we have utilized is the Green-Lagrange strain tensor $\tilde{\varepsilon}_{IJ}$, an objective polarization measure $\tilde{P}_I = F_{jI} P_j$, and an objective polarization gradient measure $\tilde{P}_{IJ} = F_{kI} P_{k,J}$.

3.2 OBJECTIVE RATE OF POLARIZATION

As mentioned previously, Equation (3.16d) and (3.17b) do not yield rigid rotation-invariant descriptions of the material dissipation. To make the description of the dissipation frame indifferent, an objective rate of polarization must be used. Historically, three objective rates are usually implemented: the Truesdell rate, the Green-Naghdi rate, and the Jaumann rate. The Jaumann rate is adopted as the objective polarization rate in the theory presented here.

The Jaumann rate of polarization is defined as

$$\overset{\Delta}{P}_i = \dot{P}_i - \omega_{ij} P_j = \dot{P}_i - \frac{1}{2}(\dot{u}_{i,j} - \dot{u}_{i,j}) P_j \tag{3.21}$$

where ω_{ij} is the spin tensor.

Under a rigid body rotation, there is no energy dissipation when using the Jaumann rate of polarization for the dissipation $\beta \overset{\Delta}{P}_i \overset{\Delta}{P}_i$, while if the dissipation is

described as $\beta \dot{P}_i \dot{P}_i$ then it is not zero for a rigid body rotation. Figure 3.2.1 shows a schematic of a polarized specimen undergoing a rigid body rotation. The electric potential on the top and bottom surfaces is fixed at zero. The initial material polarization is $P_y / P_0 = 1$, and the center-point on the bottom surface has a pin support. The upper right corner is displaced in a circular arc with the center of the arc located at the pin support.
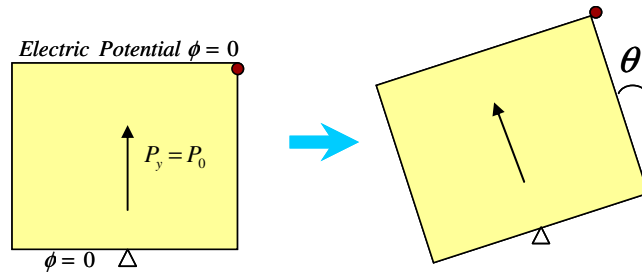
Figure 3.2.1: A schematic plot of the rigid rotation of a generalized plane strain domain. The electric potential on the top and bottom surfaces are zero. Initial material polarization is $P_y / P_0 = 1$, and the center bottom has a pin support. The entire domain rotated with the center of rotation located at the pin support.

Suppose the specimen has a rotation angle of θ, then the spin tensor $\boldsymbol{\omega}$ can be written as

$$\boldsymbol{\omega} = \begin{bmatrix} 0 & -\dot{\theta} \\ \dot{\theta} & 0 \end{bmatrix} \tag{3.22}$$

and

$$P_1 = -P_0 \sin\theta, \ \ P_2 = P_0 \cos\theta$$
$$\Rightarrow \dot{P}_1 = -P_0 \dot{\theta} \cos\theta, \ \ \dot{P}_2 = -P_0 \dot{\theta} \sin\theta \tag{3.23}$$

90

The spatial rate of polarization inherited from last chapter gives the energy dissipation rate $\dot{D}$

$$\dot{D}_{Spatial} = \int_V \beta_{ij} \dot{P}_i \dot{P}_j \, dV$$

The energy dissipation rate associated with Jaumann rate of polarization is defined as

$$\dot{D}_{Jaumann} = \int_V \beta_{ij} \overset{\Delta}{P}_i \overset{\Delta}{P}_j \, dV \tag{3.24}$$

Then the Jaumann rate of polarization is

$$\begin{cases} \overset{\Delta}{P}_1 = \dot{P}_1 - \omega_{12} P_2 = -P_0 \dot{\theta} \cos\theta - (-\dot{\theta}) P_0 \cos\theta = 0 \\ \overset{\Delta}{P}_2 = \dot{P}_2 - \omega_{21} P_1 = -P_0 \dot{\theta} \sin\theta - \dot{\theta}(-P_0 \sin\theta) = 0 \\ \Rightarrow \\ \dot{D}_{Jaumann} = \int_V \beta_{ij} \overset{\Delta}{P}_i \overset{\Delta}{P}_j \, dV = 0 \end{cases} \tag{3.25}$$

From this calculation, it is shown that the energy dissipation with the Jaumann rate of polarization is zero. Simulation results agree with the theoretical prediction. The energy dissipation with the spatial rate of the polarization is not frame indifferent, such that this rate of the polarization does not yield zero dissipation for a rigid body rotation.

3.3 FINITE DEFORMATION ANALYSIS OF THE DOMAIN NUCLEATION PROBLEM

The nucleation and growth of a new domain from a crack tip during purely electrical charge loading is simulated within the finite deformation phase-field model.

In order to compare the simulation results generated from the finite deformation phase-field model with the linear kinematics case, the size of the specimen and the loading conditions are the same as the linear kinematics simulations, which are described in Section 2.4.3.

A two-dimensional square geometry with the length of the side of the square equal to $60\,l_0$ is studied here, and the crack length equal to $30\,l_0$. The characteristic thickness of domain wall within the theory is $2\,l_0$. The generalized impermeable boundary conditions on the crack faces are applied. The initial spontaneous polarization P_0 is normal to the crack faces. The entire boundary of the square region is traction free, and the left and right sides of the region have no surface charge density. The top and bottom surfaces have an applied surface charge density of $\omega^{\pm} = \mp(P_0 - \omega_A)$, and $\omega_A = 0$ corresponds the initial state. Then ω_A is increased to apply the charge loading on the top and bottom surfaces.

At charge loading level at $\omega_A / P_0 = 0.12$, the domain was nucleated at the crack tip and allowed to evolve with a non-zero polarization viscosity term. The loading is applied by first ramping up a uniform charge load on the top and bottom surfaces with a charging rate of $\beta \dot{\omega}_A / E_0 = 0.1$ to a total charge of $\omega_A / P_0 = 0.12$ in the $60\,l_0 \times 60\,l_0$ domain. The charge was then fixed at $\omega_A / P_0 = 0.12$ and the domain structure was allowed to evolve until the solution was sufficiently close to the equilibrium configuration, at which point the polarization viscosity term was set to $\beta = 0$ to find the final equilibrium solution.

Domain Nucleation at $\omega_A / P_0 = 0.12$

Domain Evolution at $\omega_A / P_0 = 0.12$

Final Equilibrium at $\omega_A / P_0 = 0.12$
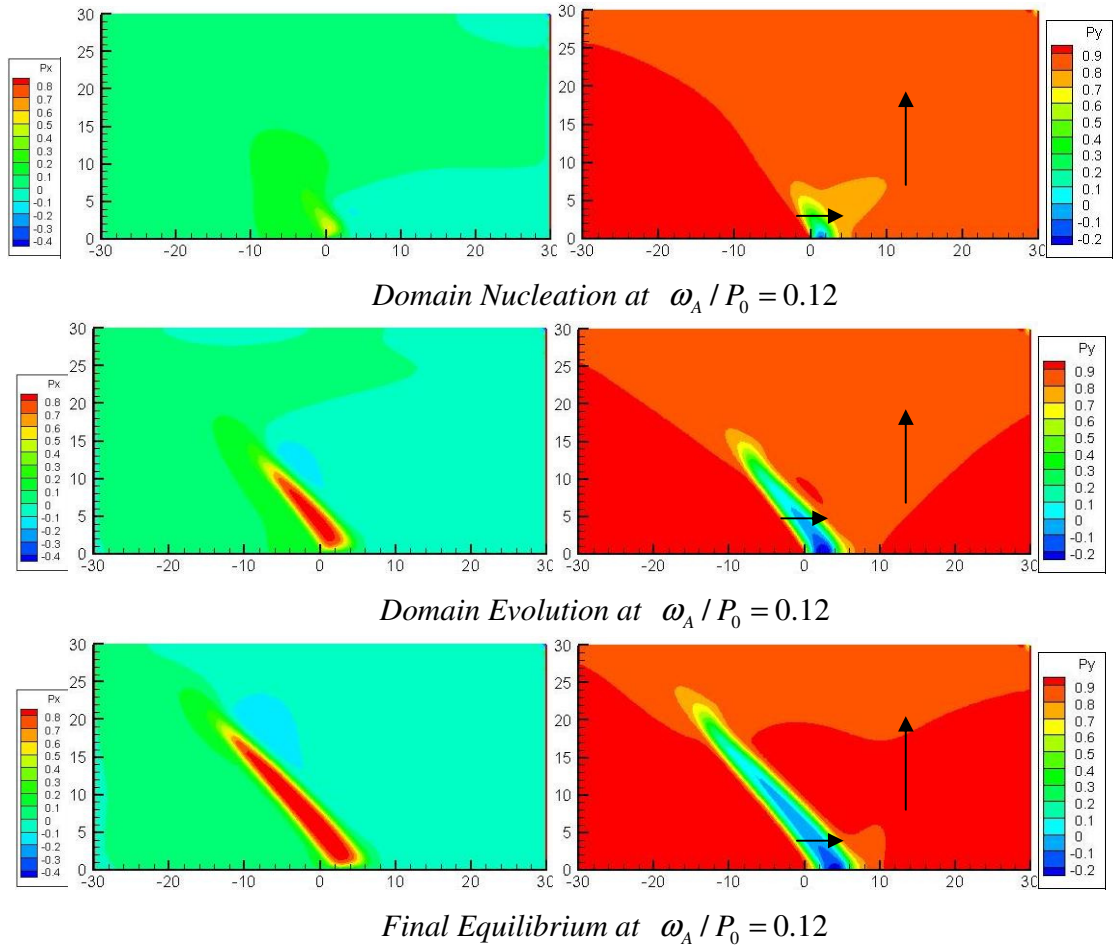
Figure 3.3.1: Contour plots of the x and y-components of the polarization normalized by P_0 in the vicinity of the crack tip during the evolution of the domain structure with the fixed charge loading $\omega_A / P_0 = 0.12$ at different times, from the nucleation of the domain to the final equilibrium configuration. Due to symmetry, only the upper half of the model is displayed.   The x and y distances are normalized as x/l_0 and y/l_0, and the polarization scale is normalized by the spontaneous polarization P_0.   The arrows represent the nominal direction of the polarization in different regions.

Figure 3.3.1 shows the contour plots of the x and y-components of the polarization normalized by P_0 in the vicinity of the crack tip during the evolution of the domain structure with the fixed charge loading $\omega_A / P_0 = 0.12$ at different times, from

93

the nucleation of the domain to the final equilibrium configuration.   The arrows represent the nominal direction of the polarization in different regions.

Comparing Figure 3.3.1 generated from finite deformation phase-field model with the Figure 2.4.7 from the linear kinematics phase-field model, the charge loading levels at nucleation of the new domain are the same, and the final domain structures for the two models are nearly indistinguishable.   We also performed the analogous simulations for the charge-controlled uniform electric potential loading case and found similar agreement between the two theories.   Hence, these results suggest that the linear kinematics assumption is sufficient for modeling most domain evolution problems in ferroelectric ceramics.

Chapter IV   Instabilities in Dielectric Elastomer Composites

While piezoelectric ceramics can generally attain strains less than 1% under electric field loading, dielectric elastomers can undergo much larger strains of over 100% and thus require a finite deformation theory for the description of the material behavior. Dielectric elastomers were implemented in the early 1990s as a new class of electroactive polymer (EAP) actuators. This material has gained substantial attentions in the last two decades for applications in dielectric elastomers include actuator devices, manipulators and energy harvesters due to their large strains that can be induced by voltage, the fast deformation response, and light weight. Excellent reviews of the literatures in this field have been given by Carpi et al. and Suo (F. Carpi et al., 2008; Suo, 2010).

4.1 BACKGROUND

In 1880, W. Roentgen designed an experiment with electric charges on natural rubber, and M. P. Sacerdote followed on Roentgen's experiment by formulating a theory on the strain response to an applied electric field in 1899. Then the first piezoelectric polymer, Electret, was discovered in 1925. In 1969, Kawai demonstrated that polyvinylidene fluoride (PVDF) exhibits a large piezoelectric effect. An important step in discovering dielectric elastomers was the work by Zhenyi et al. (Zhenyi et al., 1994) and others on investigating electrostriction in polymers, which showed the possibility of electroactive polymers beyond the already discovered piezoelectric polymers. Simultaneously, research in robotics in the late 1980s, and the need for flexible large-stroke actuators, also lead to enhanced interest in dielectric elastomers.

All dielectric materials contain bound electrons or ions, which do not move over significant distances causing charge flow though the material as in a conductor. Instead,

the charge carriers can only shift slightly from their equilibrium positions in response to an applied electric field, and this process is called dielectric polarization. In all materials mechanical deformation and electrical polarization are inherently coupled, and the magnitude of this coupling allows dielectric elastomers to convert electrical energy to mechanical energy in an actuator mode, or convert mechanical energy to electrical energy in a generator mode. Figure 4.1.1 illustrates a thin layer of a dielectric elastomer sandwiched between two compliant electrodes across the thickness of the layer. Applying charge to the top and bottom surfaces causes a reduction in the layer thickness and expands the cross-sectional area. This straining caused by the applied electric field can exceed 100%. This large strain behavior has led some researchers to refer to dielectric elastomers as artificial muscles.

(a) Reference State   (b) Current State
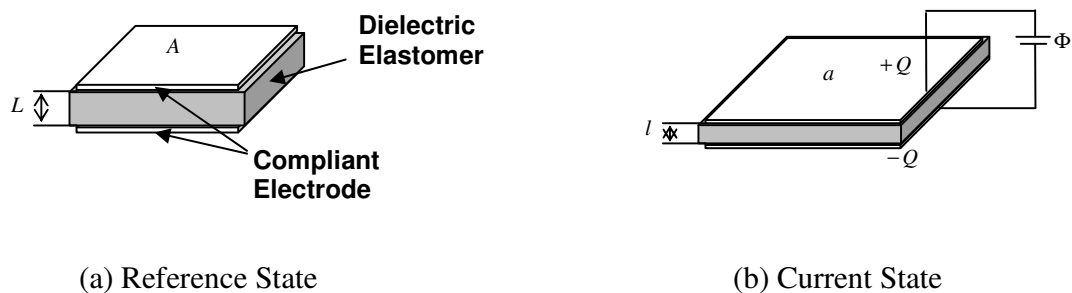
Figure 4.1.1:   A schematic plot of a dielectric elastomer in the (a) reference state and (b) the deformed or current state. The dielectric elastomer deforms under the applied electric field.

The electric field in the dielectric elastomer is given as $E = \Delta\phi/l$. As the applied electric field increases, the electrostrictive effect causes the dielectric elastomer to become thinner, which causes an even higher electric field at the same voltage. The increase in the electric field lead to two possible failure modes: electrical breakdown or electromechanical instability. For ferroelectric ceramics, the deformation induced by

96

voltage is usually limited by electrical breakdown, i.e. charges are able to migrate through the material creating a highly conductive channel that connects the opposing electrodes. For dielectric elastomers as a compliant dielectric, the deformation induced by the electric field generally leads to some form of electromechanical instability. Such instabilities in dielectric elastomer composites will be investigated in the following sections of this chapter. Electromechanical instabilities are sensitive to the mechanical stress versus deformation behavior of the elastomer. Dielectric elastomers are composed of a network of long and flexible polymer chains held together by cross-links. At small deformation levels, the dielectric is compliant, since the density of the networked chains is small resulting in a lower stiffness of the elastomer. Then, as deformation proceeds, the dielectric elastomer stiffens steeply at modest stretches when the networked chains are straightened towards their full contour length. In the next section we introduce the constitutive descriptions that will be used to model these behaviors.

4.2 HYPERELASTIC MODELS

In this chapter the mechanical behavior of dielectric elastomers is modeled using finite deformation hyperelasticity. The hyperelastic material models can be classified as phenomenological descriptions of the observed behavior such as the Mooney-Rivilin and Ogden models, mechanistic models derived from arguments about the underlying structure of the material such as the Neo-Hookean model, and hybrids of the phenomenological and mechanistic approaches such as the Gent model. In our simulation, the compressible Neo-Hookean model and compressible Gent model are used.

In addition to the deformation dependence, the free energy descriptions for dielectric elastomers must also include a dependence on electric field or electrical polarization. The hyperelastic models used in this chapter that includes the electric polarization as a parameter can be found in Appendix D.

(a) Reference State   (b) Current State
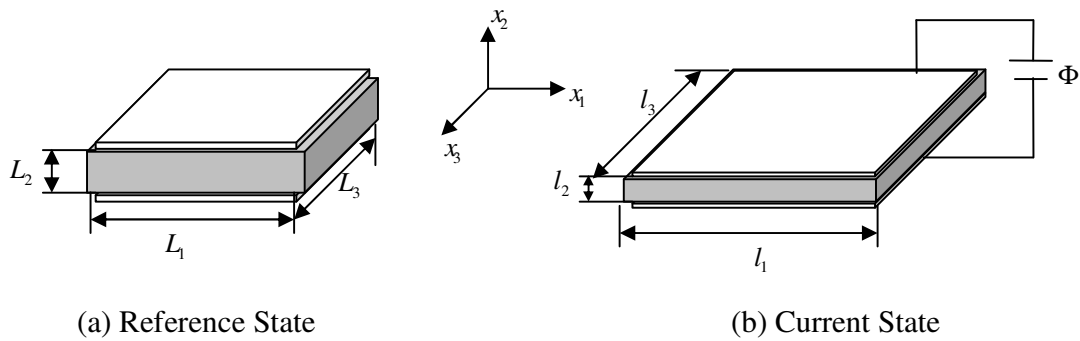
Figure 4.2.1: A schematic plot of a dielectric elastomer with dimension $L_1 \times L_2 \times L_3$ at (a) the reference state and with dimensions $l_1 \times l_2 \times l_3$ at (b) the current state. The dielectric elastomer deforms under the applied electric field.

Figure 4.2.1 shows a schematic plot of a dielectric elastomer with the dimensions $L_1 \times L_2 \times L_3$ at (a) the reference state and with the dimensions $l_1 \times l_2 \times l_3$ at (b) the current state. The dielectric elastomer will deform under the application of electric field. The principal stretches $\lambda_1, \lambda_2, \lambda_3$ are defined as $\lambda_1 = l_1 / L_1$, $\lambda_2 = l_2 / L_2$, and $\lambda_3 = l_3 / L_3$ respectively.

The general form of the free energy to be used in this chapter for the description of dielectric elastomers can be written as

$$W = W(\lambda_1, \lambda_2, \lambda_3, E)$$

$$= W_s(\lambda_1, \lambda_2, \lambda_3) - \frac{\kappa}{2} J F_{Ji}^{-1} F_{Ki}^{-1} \tilde{E}_J \tilde{E}_K \qquad (4.1)$$

$$= W_s(\lambda_1, \lambda_2, \lambda_3) - \frac{\kappa}{2} J C_{JK}^{-1} \tilde{E}_J \tilde{E}_K$$

where $W_s(\lambda_1, \lambda_2, \lambda_3)$ is the energy due to stretching which will be different for the different hyperelastic models, κ is the dielectric electrical permittivity of the material, J is the determinant of gradient deformation tensor, $\tilde{\mathbf{E}}$ is the reference electric field in reference state, $\mathbf{F}^{-1}$ is the inverse of the deformation gradient tensor and $\mathbf{C}^{-1}$ the inverse of right Cauchy-Green deformation tensor. Note that the electrical part of the free energy assumes that the dielectric permittivity of the material is independent of the volume change, which is a feature that can of course be modified but is approximately true for many materials.

Using the assumption of generalized plane strain, $\lambda_3 = 1$. Then the energy form in (4.1) can be expanded for the different hyperelastic models.

The compressible Neo-Hookean model takes the free energy form

$$W_N^C = -\frac{1}{2} \kappa_{mat} J (C_{11}^{-1} \tilde{E}_1^2 + C_{22}^{-1} \tilde{E}_2^2 + C_{12}^{-1} \tilde{E}_1 \tilde{E}_2 + C_{21}^{-1} \tilde{E}_2 \tilde{E}_1)$$
$$+ \frac{\mu}{2} (I_1^C J^{-2/3} - 3) + \frac{K}{2} (J - 1)^2 \qquad (4.2)$$

where κ is the permittivity, the subscript $_{mat}$ represents the permittivity of the dielectric elastomer material, J is the determinant of the deformation gradient tensor $J = \det(\mathbf{F})$, $\mathbf{C}$ is the right Cauchy-Green deformation tensor, $\tilde{\mathbf{E}}$ is the reference electric field, I_1^C is the first invariant of right Cauchy-Green deformation tensor

$I_1^C = tr(\mathbf{C}) = C_{II}$, and μ, K are the shear modulus and bulk modulus of the dielectric elastomer respectively.

The first line of the energy form in (4.2) represents the energy stored in the material with the coupling between mechanical deformation and the electric field, and the second line represents the Helmholtz free energy associated with the stretching of the elastomer. For the incompressible case, $J = \det(\mathbf{F}) = 1$, the energy function of the Neo-Hookean model will reduce to the form

$$W_N^I = -\frac{1}{2}\kappa_{mat}(C_{11}^{-1}\tilde{E}_1^{\;2} + C_{22}^{-1}\tilde{E}_2^{\;2} + C_{12}^{-1}\tilde{E}_1\tilde{E}_2 + C_{21}^{-1}\tilde{E}_2\tilde{E}_1)$$
$$+\frac{\mu}{2}(I_1^C - 3)$$

(4.3)

The compressible Gent model takes the form

$$W_G^C = -\frac{1}{2}\kappa_{mat}J(C_{11}^{-1}\tilde{E}_1^{\;2} + C_{22}^{-1}\tilde{E}_2^{\;2} + C_{12}^{-1}\tilde{E}_1\tilde{E}_2 + C_{21}^{-1}\tilde{E}_2\tilde{E}_1)$$
$$-\frac{\mu}{2}J_m \ln(1 - \frac{I_1^C - 3}{J_m}) - \mu\ln J + \frac{K}{2}(\frac{J^2-1}{2} - \ln J)$$

(4.4)

where J_m denotes the limiting value for $I_1^C - 3$ and is a new material constant. This parameter allows the model to represent the saturation of deformation associated with the straightening of the polymer chains. As for the Neo-Hookean model, the first line in equation (4.4) is the energy stored in the material, and the second line is the Helmholtz free energy associated with the stretching. For the incompressible case, the free energy form of Gent model reduces to

$$W_G^I = -\frac{1}{2}\kappa_{mat}(C_{11}^{-1}\tilde{E}_1^{\ 2} + C_{22}^{-1}\tilde{E}_2^{\ 2} + C_{12}^{-1}\tilde{E}_1\tilde{E}_2 + C_{21}^{-1}\tilde{E}_2\tilde{E}_1)$$
$$-\frac{\mu}{2}J_m\ln(1-\frac{I_1^C-3}{J_m})$$

(4.5)

Furthermore, in the limit as $J_m \to \infty$, the Gent model reduces to the Neo-Hookean model.

The finite element method is used as numerical technique to solve the boundary value problems, and mechanical displacement and electric potential are chosen as the nodal degrees of freedom.

4.3 SIMULATION RESULTS

In this section, we studied the electromechanical behavior of dielectric elastomers filled with square arrays of different inclusion types using compressible Neo-Hookean model and Gent models for the description of the elastomer.   Finite deformation affects are accounted for and the theory is implemented in the finite element method.

(a)   (b)
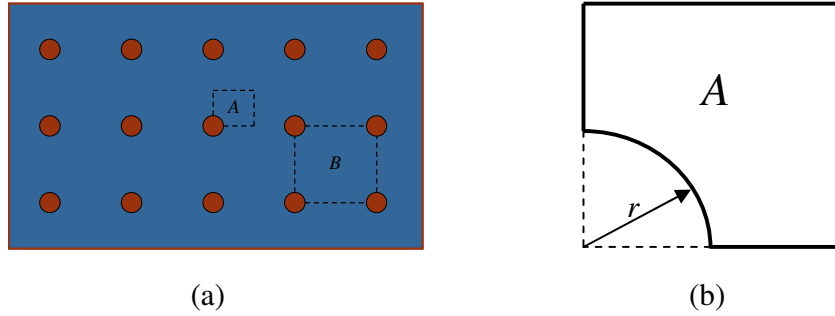
Figure 4.3.1:   A schematic plot of a generalized plane strain dielectric elastomer specimen with a repeated pattern of long cylindrical inclusions.   Due to symmetry, only the regions A or B enclosed by the dashed lines are analyzed.   The small cell A is a $L \times L$ square, and the radius of the inclusion is r.

Figure 4.3.1 shows a schematic plot of a dielectric elastomer specimen with a square array of long cylindrical inclusions.   Due to symmetry, only the regions enclosed by the dashed lines, small cell A and large cell B, are analyzed.   Consider a two-dimensional $L \times L$ square region as in Figure 4.3.1(b), with the radius of an inclusion as r.   Four different inclusion types are considered: (1) rigid conducting inclusions, (2) conducting holes, (3) impermeable (perfectly insulating) holes and (4) air-filled insulating holes.   We study ratios of the inclusion size to the specimen side length r/L, from 0 to 1 with the increments of 1/10.   Here we use the plane strain assumption such that the strain in the x_3 direction is assumed to be zero.
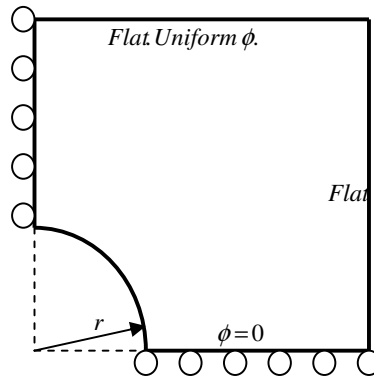
Figure 4.3.2: In a $L \times L$ square, the radius of the inclusion is r. The left boundary is charge free and the horizontal displacement is zero due to symmetry; the right boundary is charge free and remains straight and vertical; the vertical displacement and electric potential for the lower boundary are zero; the top boundary remains straight and horizontal with a uniform electric potential. The boundary conditions at the inclusion boundary vary with the different inclusion types.

The first simulations are for a material with different inclusion sizes and types under pure electric loading in a $L \times L$ domain. As shown in Figure 4.3.2, in a $L \times L$ square, the radius of inclusion is r.   The left boundary is charge free and the horizontal

102

displacement is zero due to symmetry; the right boundary is charge free and remains straight and vertical; the vertical displacement and electric potential for the lower boundary are zero; the top boundary remains straight and horizontal with a uniform electric potential. The boundary conditions at the inclusion boundary vary with the different inclusion types.

(1) Rigid conducting inclusions: mechanical displacement and electric potential at the inclusion interface are fixed at zero.

(2) Conducting holes: the interface is free of mechanical tractions, and the electric potential at the interface is zero.

(3) Air-filled insulating holes: the interface between air and material is free of mechanical tractions and charges, and the air inside the hole is modeled such that the permittivity of free space is also accounted for.

(4) Impermeable (perfectly insulating) holes: the interface is free of mechanical tractions and charges, and the permittivity of free space is approximately to be zero.

In order to track solutions after electrical "softening" occurs, the electrical loading is increased by increasing the net charge on the top surface while maintaining a uniform electric potential uniform along the surface. The nominal electric field $E = \phi / L$, where ϕ is the electric potential on the top surface and L the initial length of the unit cell. The nominal electric displacement $D = Q / A$, where Q is the total applied charge to the upper surface, and A is the initial area of the top surface. The electric field and the electric displacement are normalized by $\sqrt{\mu / \kappa}$ and $\sqrt{\mu \kappa}$ respectively, where μ is the shear modulus and κ is the permittivity of the material. To illustrate the behavior of the material when there is no inclusion, the contraction of the speciment in the direction of applied charge is plotted as a function of the electric displacement in Figure 4.3.3 for a Neo-Hookean material. As an electrical loading is applied, the

material contracts.   This behavior can be rationalized in several ways, the simplest being that the full electromechanical energy of the system is reduced if the electrodes move together.   This reduction in energy consists of an increase in the strain energy and the stored electrostatic energy along with a reduction in the potential energy due to the electrical work done by the battery that feeds charge to the electrodes in order to keep the voltage constant.
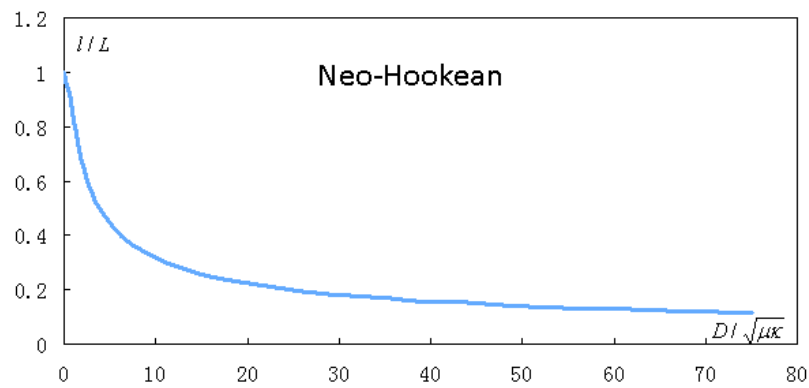
Figure 4.3.3:   The stretch in the direction of applied charge is plotted as a function of the nominal electric displacement.   The electric displacement is normalized by $\sqrt{\mu\kappa}$, where μ is the shear modulus and κ is the dielectric permittivity of the material.   This plot is for the Neo-Hookean material without an inclusion.

Figure 4.3.4 shows the comparison of the charge-voltage behavior predicted by the Neo-Hookean model and the Gent model with $J_m=50$.   The nominal electric displacement is plotted as the function of the nominal electric field.   Figure 4.3.4(b) magnifies the region in plot (a).

104
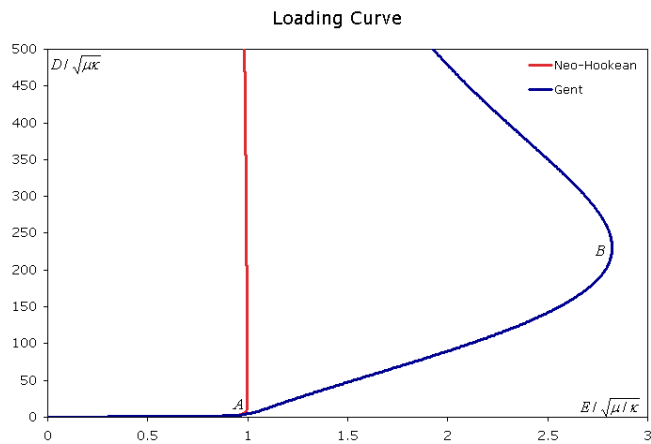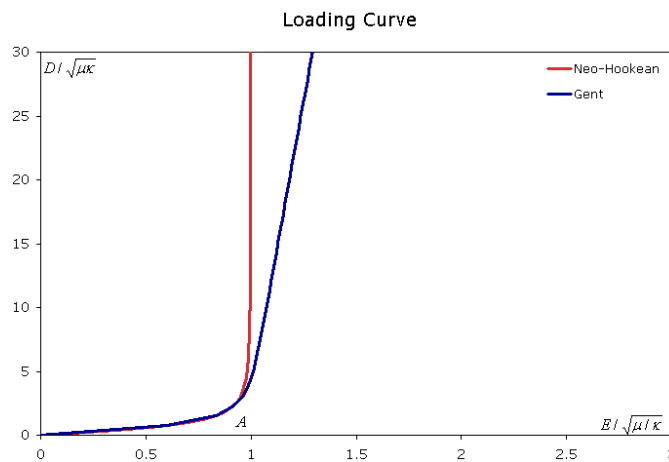
Figure 4.3.4: Comparison between the Neo-Hookean model and the Gent model with J_m=50. The nominal electric displacement is plotted as a function of the nominal electric field. (b) magnifies the region near point A in the plot (a). For both models, the material responses are approximately linear. At point A, the two models diverge, the Gent model shows that the material "hardens" initially, and beyond load level B, localized thinning occurs and the voltage decreases with increasing charge.

For both models at low levels of applied voltage the electrical response for the capacitor structure in that charge flows easily between the two electrodes without the need for increases in the applied voltage. In contrast, the Gent model predicts that the

structure has an electrical "hardening" behavior where additional voltage is required to cause the charge transfer between electrodes. Note that even for the Gent model the structural electrical response can be characterized as "soft" after point A. For the Gent material there is eventually a voltage level, point B, that does lead to an instability where the voltage decreases with the increasing charge. Notice that the plot illustrates that the Neo-Hookean and the Gent models share the same electrical "softening" point A in the structural response. To illustrate an example for a dielectric elastomer composite, Figure 4.3.5 plots a similar comparison of the charge-voltage curve for the Neo-Hookean model and the Gent model with J_m=50 when the normalized inclusion size is r/L=0.8. Again, this figure illustrates that the structural softening points at which where the slope of response changes significantly are similar for both models. Hence, in many cases we will simply use the Neo-Hookean model to report unambiguous instability points for the composites structures to be investigated.
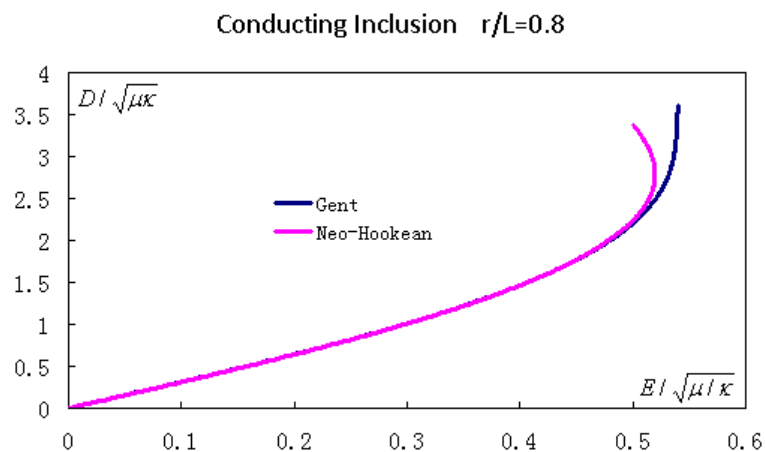
Figure 4.3.5: Comparison of the charge-voltage curves from the Neo-Hookean model and the Gent model with J_m=50 for rigid conducting inclusions of radius r/L=0.8. The x-axis represents the normalized nominal electric field and the y-axis represents the normalized nominal electric displacement.

106

Comparisons of the charge-voltage curves for different types of the four different inclusions: rigid conducting inclusions, conducting holes, perfectly insulating holes, and air-filled insulating holes; with the inclusion size r/L=0.8 using the Neo-Hookean model are shown in Figure 4.3.6. With the same normalized electric displacement, the normalized electric field decreases in the order of the ratio of permittivity in the free space to the material. Rigid conducting inclusions and conducting holes assume infinity permittivity of free space, then different insulating holes take the ratio of permittivity in the dielectric material to the free space to be 1,2,5,10, and finally impermeable (perfectly insulating) holes implied zero permittivity in the free space.

Inclusion r/L=0.8
Neo-Hookean
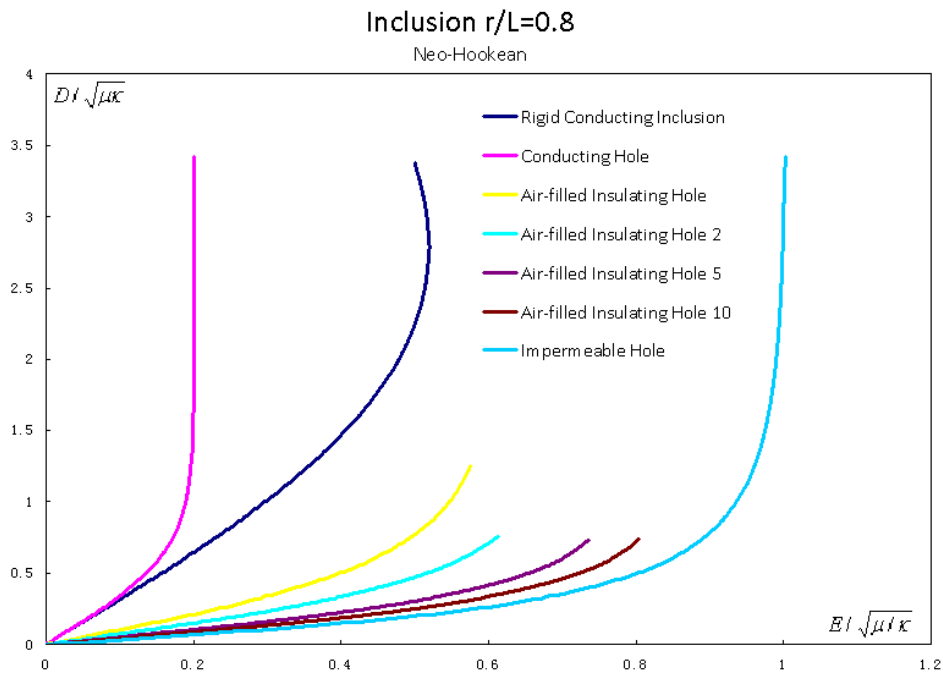
Figure 4.3.6: Comparison of the charge-voltage curves for different types of inclusions: rigid conducting inclusions, conducting holes, impermeable (perfectly insulating) holes and air-filled insulating holes with the inclusion size r/L=0.8 using the Neo-Hookean model. The x-axis represents the normalized nominal electric field and the y-axis represents the normalized nominal electric displacement.
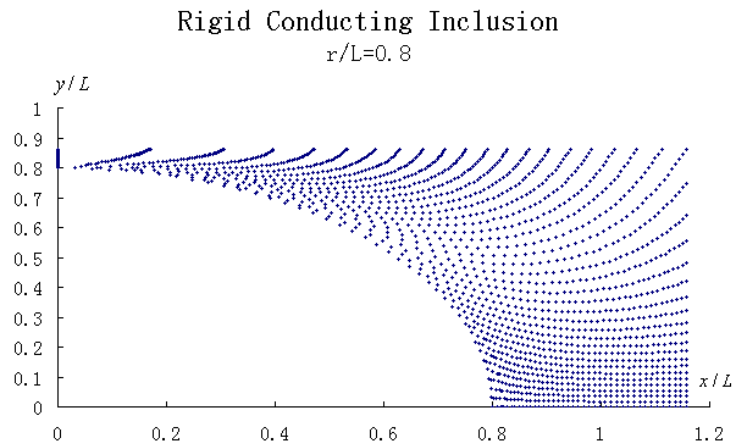
Figure 4.3.7: The deformation mode at instability for rigid conducting inclusions with the inclusion size r/L=0.8, using the Neo-Hookean model.
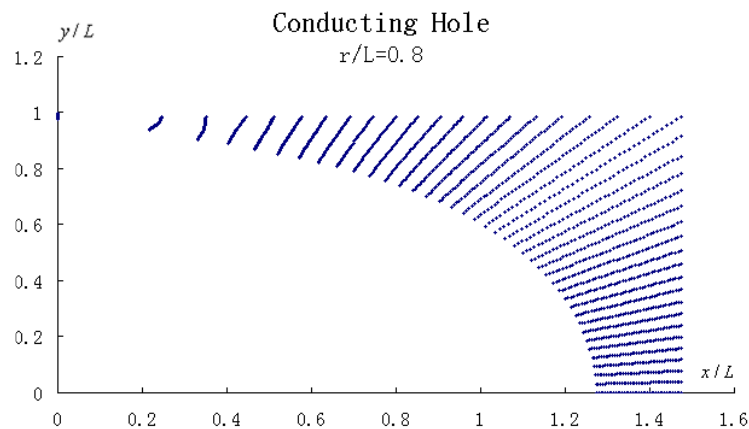
Figure 4.3.8: The deformation mode at instability for conducting holes with the inclusion size r/L=0.8, using the Neo-Hookean model.

The deformation modes at the instability are different for the different types of inclusions. In Figures 4.3.7~4.3.10, these deformation modes at the instability for different inclusion types are plotted. Here, the material model used is the Gent model with J_m=50. For the conducting inclusions, including rigid conducting inclusions and conducting holes, a pinching instability is favored. The thickness of the material

between adjacent inclusions/holes becomes very small.   The instability occurs when the increase of the local electric field due to the ligament thinning overwhelms the materials ability to elastically resist the deformation.   In contrast, the perfectly insulating holes (and we suspect that this also occurs for the air-filled holes) undergo a cusping/collapse type of instability, where the sides of the holes collapse and contact occurs forming a cups at the hole equators.   We were unable to numerically achieve the cusp instability in the air-filled holes due to the requirement that the air inside the holes must be meshed. Since this material has no elastic stiffness, multi-point constraints, connecting the internal nodes to control nodes on the hole boundary, were used to control the displacements of the nodes on the inside of the hole.   As the hole starts to collapse the control nodes on the boundary move in a way that causes ill-conditioning of the internal elements leading to numerical difficulties in obtaining valid solutions.   This is not to say that such solutions are impossible, but rather that a more sophisticated procedure is required to control the displacements and mesh configuration that represents the air inside of the holes.

Air-filled Insulating Hole
r/L=0.8

(a)

Impermeable Hole r/L=0.8
$D / \sqrt{\mu \kappa} = 0.556$

(b)
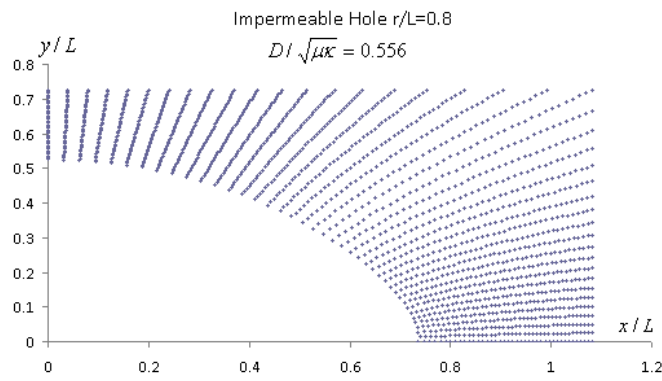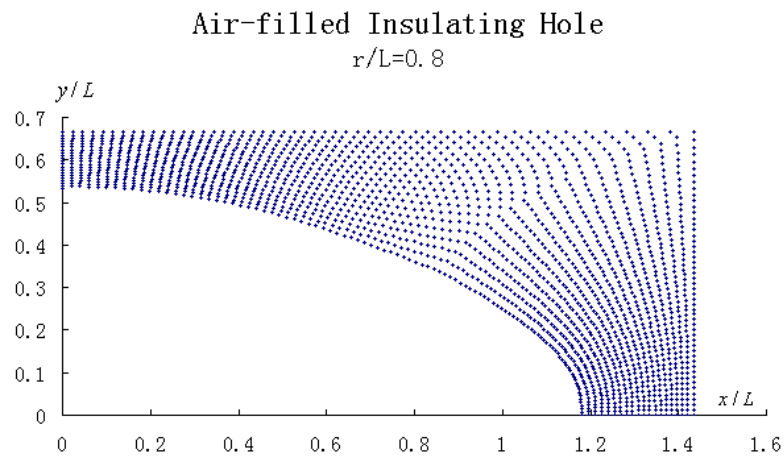
Figure 4.3.9: (a) The deformation mode at the numerical instability for air-filled insulating holes with the inclusion size r/L=0.8, using the Neo-Hookean model. (b) The deformation for impermeable (perfectly insulating) holes with the inclusion size r/L=0.8 at small load.
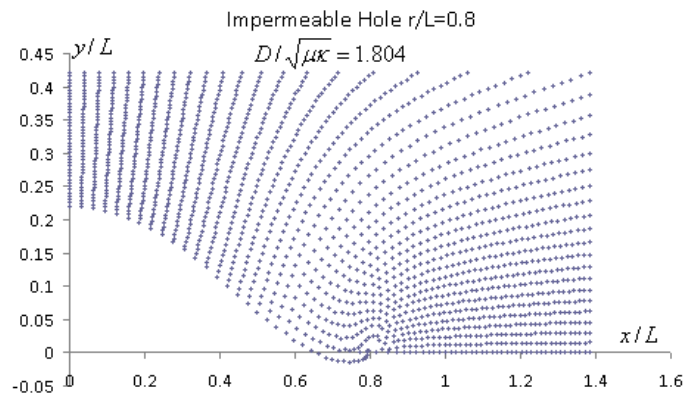
Figure 4.3.10: The deformation mode at instability for impermeable (perfectly insulating) holes with the inclusion size r/L=0.8, using the Gent model with J_m=50.

The normalized electrical loads at the electrical loading instability for the different inclusion types using the Neo-Hookean material model are compared in Figure 4.3.11. For conducting holes, the critical load at instability is linear in the inclusion size. As the inclusion size increases, the critical electrical loading level at the instability decreases primarily because the pinching instability can occur more readily in the thinner ligaments separating the holes.
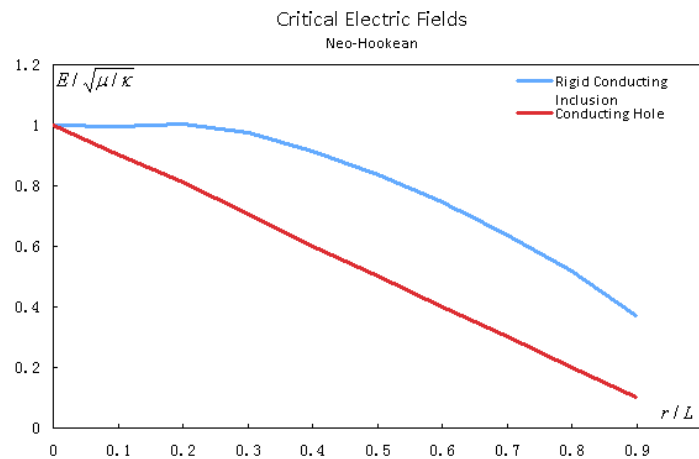
Figure 4.3.11: The loads at instability are plotted with respect to inclusion size for rigid conducting inclusions and conducting holes using the Neo-Hookean model.

111

The calculations above are based on the small unit cell, region A in Figure 4.3.1. The small unit cell places considerable constraints on the deformation patterns that can be achieved in the composite. To investigate other modes of deformation a larger unit cell is introduced. Instead of pure electrical loading, mechanical loading will be applied first, and then followed by electrical loading. The instabilities in this structure due to mechanical loading has been studied by Bertoldi and Boyce (2008) and Triantafyllidis et al. (2006). A schematic plot and mesh of the large unit cell, region B in Figure 4.3.1, is shown in Figure 4.3.13. When charge is applied, the loading curves for the large unit cell and small unit cell are compared for air-filled insulating holes r/L=0.9 using the Gent model with J_m=50. For the large unit cell, the bottom surface is fixed in the vertical direction and the electric potential is zero; the left surface is constrained to remain flat and the horizontal mechanical displacement is zero due to symmetry; and the right surface is constrained to remain flat. The top surface is also constrained to remain flat, and the electric potential is uniform along this surface. A compressive mechanical displacement is applied on the top surface to reach and go beyond the mechanical loading instability, and then charge is applied with the mechanical displacement held fixed on the top surface. Two different inclusion types are investigated: air-filled insulating holes with $\kappa_{mat} = 10\kappa_{hole}$ and conducting holes with $\kappa_{mat} = \kappa_{hole}/1000$. In the calculation, the Gent model with J_m =50 is used and the inclusion size r/L is 0.9.
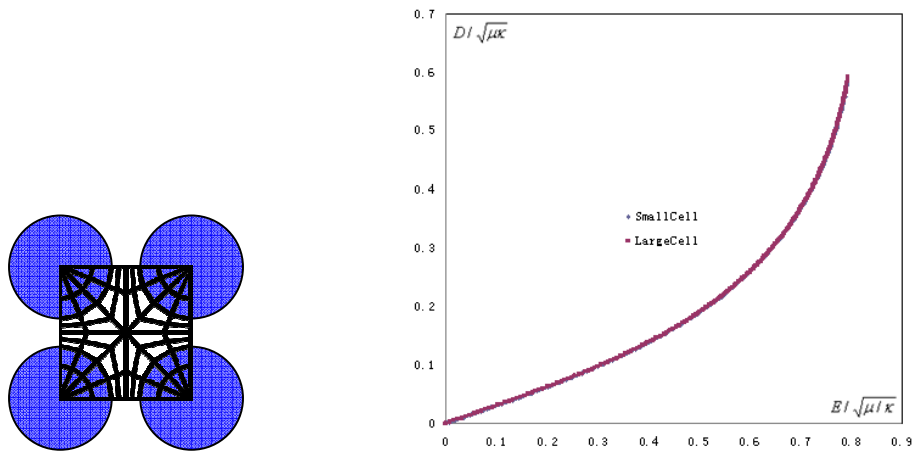
Figure 4.3.13: A schematic plot and mesh of region B in Figure 4.3.1. The loading curve of large unit cell and small unit cell are compared for the air-filled insulating holes of radius r/L=0.9 using the Gent model with J_m=50.

Figure 4.3.14(a) shows the mechanical loading curve for the large unit cell. The x-axis is the normalized strain and the y-axis is the normalized first Piola-Kirchhoff stress. Figure 4.3.14(b) illustrates the deformation mode of the mechanical loading instability. The elastomers "buckle" under the mechanical compression in the vertical direction. This calculation is for the Gent model with J_m=50, air-filled insulating holes ($\kappa_{mat} = 10\kappa_{hole}$) and conducting holes ($\kappa_{mat} = \kappa_{hole}/1000$) with inclusion size r/L=0.9. Both the air-filled insulating holes and the conducting holes share the same behavior since the material is subject to mechanical loading only.
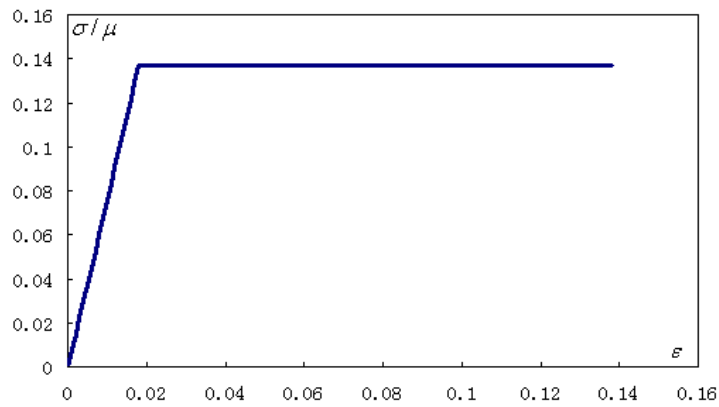
(a)
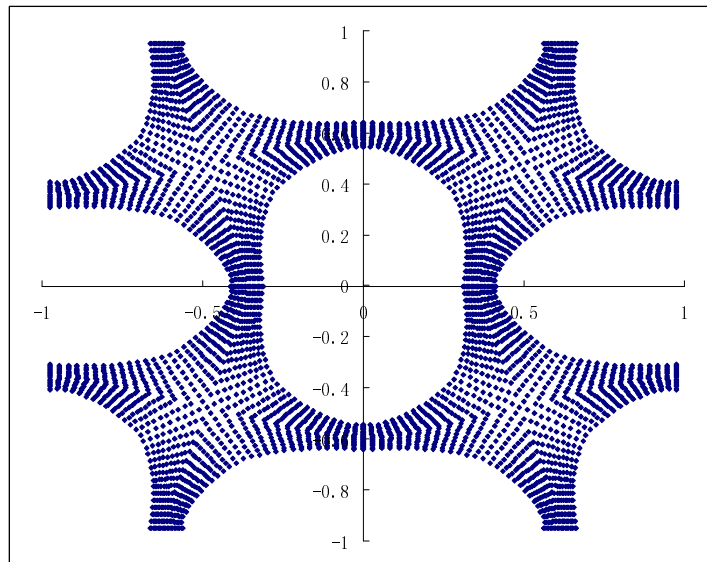
(b)

Figure 4.3.14: (a) Mechanical loading curve for the large unit cell. (b) The deformation mode at the mechanical loading instability. The calculation is for the Gent model with J_m=50, air-filled insulating holes ($\kappa_{mat} = 10\kappa_{hole}$) and conducting holes ($\kappa_{mat} = \kappa_{hole}/1000$) with inclusion size r/L=0.9.

(a)

(b)
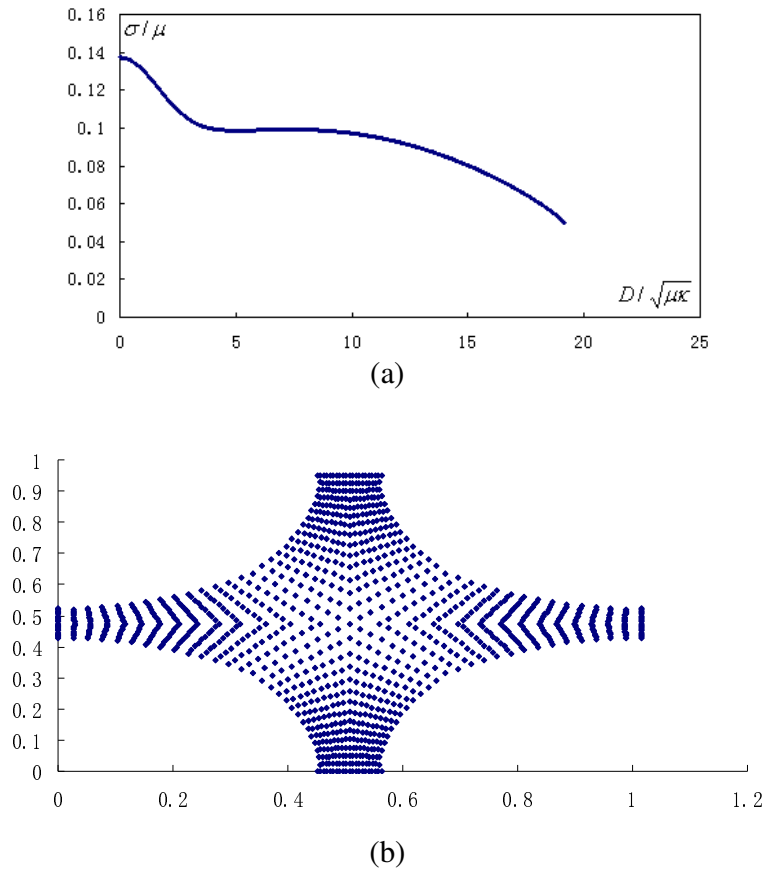
Figure 4.3.15: (a) Mechanical stress versus applied electric displacement with fixed mechanical displacement on the top surface u/L=-0.05. When mechanical stress reaches zero, the material is unbuckled. (b) The shape at the unbuckled state. The calculation is for the Gent model with J_m=50, air-filled insulating holes ($\kappa_{mat} = 10\kappa_{hole}$) with inclusion size r/L=0.9.

With the mechanical displacement fixed on the top surface, the charge is now applied. The air-filled insulating holes and the conducting holes now behave differently. For the air-filled insulating holes, Figure 4.3.15(a) shows mechanical stress versus applied electric displacement response, with the mechanical displacement on the top surface fixed at u/L=-0.05. The first Piola-Kirchhoff stress decreases nearly quadratically with the applied charge. Then when mechanical stress reaches zero, the

115

material is unbuckled (the unbuckled shape is drawn in Figure 4.3.15(b)).   After unbuckling, the deformation mode follows that of the simple unit cell, and if more charge is applied, the first Piola-Kirchoff stress behaves nearly linearly in the electric displacement.
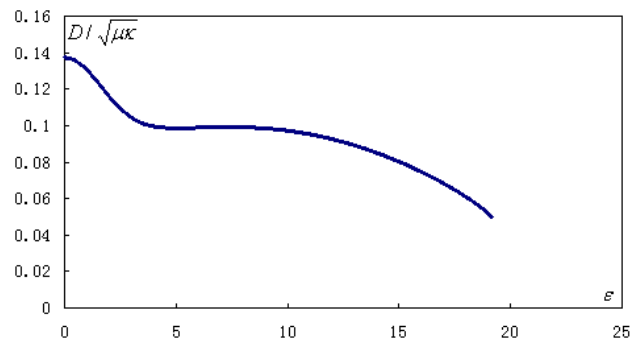
(a)
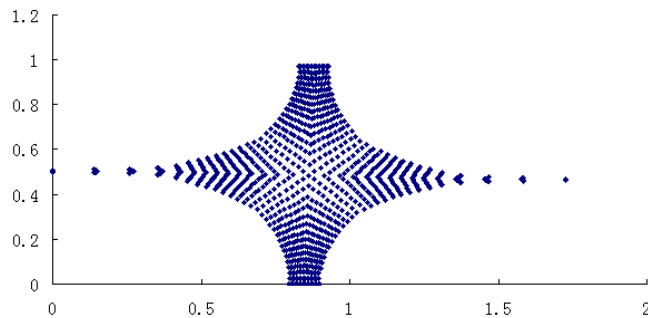
(b)

Figure 4.3.16: (a) Mechanical stress versus applied electric displacement with fixed mechanical displacement on the top surface with u/L=-0.03.   The pinching instability occurs as the applied charge increases.   (b) The deformation mode at the pinching instability.   The calculation is for the Gent model with J_m=50, conducting holes ($\kappa_{mat} = \kappa_{hole}/1000$) with inclusion size r/L=0.9.

For the conducting holes ($\kappa_{mat} = \kappa_{hole}/1000$) with inclusion size r/L=0.9, Figure 4.3.16(a) shows the curve of mechanical stress versus the applied electric displacement,

with mechanical displacement on the top surface fixed at u/L=-0.03. For this case, the unbuckling and the pull-in process occur simultaneously. Then, when the applied charge reaches a critical value the material experiences a pinching instability. The deformation mode at the pinching instability is plotted in Figure 4.3.16(b).

4.4 DISCUSSION

In Chapter 3, finite deformation effects were incorporated into the phase-field theory. An objective rate of the electric polarization was used to cause the energy dissipation to be frame indifferent.   Since the working strain of ferroelectric ceramics is small, it was shown the qualitative results for the numerical simulation of domain evolution with the finite deformation theory does not significantly differ from its linear kinematics counterpart.   Hence, for most domain structure evolution problems we tentatively conclude that the assumptions associated with linear kinematics assumption are acceptable.   We do envision that even for these materials there are likely to be some problems where the effects of finite deformations are significant.

In contrast to ferroelectric ceramics, dielectric elastomers can undergo strains on the order to ~100%, so that difference between the reference configuration and current/deformed configuration is significant.   In this chapter the finite deformation effects and the associated electrical forces are accounted for, and the theory is implemented using the finite element method. Hyperelastic models, such as the Neo-Hookean model and the Gent model, are used to describe the elastic parts of the material free energy.   The electromechanical behavior, including the occurrence of some interesting instabilities, of dielectric elastomers filled with square arrays of different inclusions types were then studied.   For the electrical loading instability, the conducting

117

inclusions favor a pinching instability whereas the insulating holes undergo collapse/cusping instability. Next, the mechanical loading instability was investigated, followed by electrical loading with fixed mechanical load. The results show that the insulating holes will unbuckle and return to the initial state under the application of electrical loading, while the conducting holes will unbuckle but undergo pinching instability with electrical loading.

Chapter V Outlook and Future Work

During the course of the studies described in this dissertation, several issues associated with the numerical solution of the phase-field model were encountered. First, in many cases the domain structures that arise in a given simulation can be difficult to predict a priori. Prior knowledge of the expected domain structures can be used advantageously when constructing finite element meshes for a given initial-boundary value problem. Fine meshes are desired in regions where domain walls are expected (due to the large polarization gradients), and in order to reduce the computational overhead, coarse meshes are preferred in regions where the solution is expected to be smooth. Problems can arise when domains nucleate and grow into regions where the mesh is coarse. This leads us to the second issue that the regions of the coarse mesh act as numerical pinning sites. What this means is that a domain wall that would otherwise sweep through a region unimpeded is instead stopped at the location where the mesh coarsens. Clearly, when this occurs the accuracy of the solution is poor and the results can no long be trusted. These numerical issues were not addressed in this work, but clearly adaptive mesh refinement and coarsening strategies will be beneficial for the accurate solution of problems where the domain structure evolution is unpredictable.

One of the tentative findings from Chapter 3 was that the inclusion of finite deformation effects did not play a large role in the domain nucleation and subsequent evolution from a crack tip. However, caution should be taken when attempting to extrapolate this observation to other boundary value problems. For example, finite deformation will certainly be important in thin structures that may undergo large deflections and rotations but relatively small strains. Also, the region within a crack can be modeled directly, which will then allow for the fully consistent integration of electrical

forces on crack faces within this modeling approach. At present, the state-of-the art for applying electrical tractions on crack faces uses a linear kinematics description of the bulk but a finite deformation description of the crack interior. This, albeit minor, inconsistency can be "fixed" by using a full finite deformation approach.

A final challenge that was encountered when generating the numerical simulations was for the collapse/cusping of the air-filled holes in the dielectric elastomer composite studies. In fact, this mode of deformation was unexpected and to my knowledge has not yet been observed. In order to investigate this phenomenon properly, numerical techniques that can handle the contact and large geometry changes within the holes are needed. It may be possible that the initiation of the cusping phenomenon can be handled with simple-minded methods, but the post-cusping behavior will most likely require more sophisticated numerical techniques.

Appendix A: Linear Piezoelectric Constitutive Laws

Depending on which independent fields variables are used, four forms of the linear piezoelectric constitutive laws governing the relationship among mechanical stress, mechanical strain, electric field and electric displacement about a fixed remanent strain and polarization state are given here.

$$\varepsilon_{ij} - \varepsilon_{ij}{}^{r} = s_{ijkl}^{E}\sigma_{kl} + d_{kij}E_{k}$$
$$D_{i} - P_{i}^{r} = d_{ikl}\sigma_{kl} + \kappa_{ij}^{\sigma}E_{j}$$

(A.1)

or

$$\sigma_{ij} = c_{ijkl}^{E}(\varepsilon_{kl} - \varepsilon_{kl}{}^{r}) - e_{kij}E_{k}$$
$$D_{i} - P_{i}^{r} = e_{ikl}(\varepsilon_{kl} - \varepsilon_{kl}{}^{r}) + \kappa_{ij}^{\varepsilon}E_{j}$$

(A.2)

or

$$\sigma_{ij} = c_{ijkl}^{D}(\varepsilon_{kl} - \varepsilon_{kl}{}^{r}) - h_{kij}(D_{k} - P_{k}{}^{r})$$
$$E_{i} = -h_{ikl}(\varepsilon_{kl} - \varepsilon_{kl}{}^{r}) + \beta_{ij}^{\varepsilon}(D_{i} - P_{i}^{r})$$

(A.3)

or

$$\varepsilon_{ij} - \varepsilon_{ij}{}^{r} = s_{ijkl}^{D}\sigma_{kl} + g_{kij}(D_{k} - P_{k}{}^{r})$$
$$E_{i} = -g_{ikl}\sigma_{kl} + \beta_{ij}^{\sigma}(D_{j} - P_{j}{}^{r})$$

(A.4)

where $\varepsilon_{ij}{}^{r}$ and P_{i}^{r} are the remanent strain and polarization; S_{ijkl}^{E}, S_{ijkl}^{D}, C_{ijkl}^{E}, and C_{ijkl}^{D} are the fourth rank tensors of elasticity; d_{kij}, e_{kij}, h_{kij} and g_{kij} are the third rank tensors of piezoelectricity; κ_{ij}^{σ}, $\kappa_{ij}^{\varepsilon}$, β_{ij}^{σ}, and β_{ij}^{ε} are the second rank dielectric tensors. Relationships among the different coefficients can be obtained by manipulating the different forms of the constitutive laws.

Appendix B: Helmholtz Free Energy and Material Properties of Barium Titanate $BaTiO_3$

The general form for the Helmholtz free energy applied in Chapter 2 is given in Equation (2.18).   For a coordinate system with the Cartesian axes aligned with <1 0 0> directions, the specific form used to fit the dielectric, piezoelectric and elastic properties of ferroelectric single crystals that undergo a cubic to tetragonal phase transformation through the Curie temperature is:

$$\psi = \frac{a_0}{2}(P_{1,1}^2 + P_{2,2}^2 + P_{3,3}^2 + P_{1,2}^2 + P_{2,1}^2 + P_{1,3}^2 + P_{3,1}^2 + P_{2,3}^2 + P_{3,2}^2)$$

$$+ \frac{a_1}{2}(P_1^2 + P_2^2 + P_3^2) + \frac{a_2}{4}(P_1^4 + P_2^4 + P_3^4) + \frac{a_3}{2}(P_1^2 P_2^2 + P_2^2 P_3^2 + P_1^2 P_3^2)$$

$$+ \frac{a_4}{6}(P_1^6 + P_2^6 + P_3^6) + a_6(P_1^4(P_2^2 + P_3^2) + P_2^4(P_1^2 + P_3^2) + P_3^4(P_1^2 + P_2^2))$$

$$+ \frac{a_5}{4}(P_1^4 P_2^4 + P_2^4 P_3^4 + P_3^4 P_1^4) - \frac{b_1}{2}(\varepsilon_{11} P_1^2 + \varepsilon_{22} P_2^2 + \varepsilon_{33} P_3^2)$$

$$- \frac{b_2}{2}((\varepsilon_{22} + \varepsilon_{33})P_1^2 + (\varepsilon_{11} + \varepsilon_{33})P_2^2 + (\varepsilon_{11} + \varepsilon_{22})P_3^2)$$

$$- b_3((\varepsilon_{12} + \varepsilon_{21})P_1 P_2 + (\varepsilon_{13} + \varepsilon_{31})P_1 P_3 + (\varepsilon_{23} + \varepsilon_{32})P_2 P_3)$$

$$+ \frac{c_1}{2}(\varepsilon_{11}{}^2 + \varepsilon_{22}{}^2 + \varepsilon_{33}{}^2) + c_2(\varepsilon_{11}\varepsilon_{22} + \varepsilon_{11}\varepsilon_{33} + \varepsilon_{22}\varepsilon_{33})$$

$$+ \frac{c_3}{2}((\varepsilon_{12} + \varepsilon_{21})^2 + (\varepsilon_{13} + \varepsilon_{31})^2 + (\varepsilon_{23} + \varepsilon_{32})^2)$$

$$+ (\frac{f_1}{2}\varepsilon_{11}{}^2 + \frac{f_2}{2}(\varepsilon_{22} + \varepsilon_{33})^2 + f_3(\varepsilon_{11}\varepsilon_{22} + \varepsilon_{11}\varepsilon_{33}) + f_4\varepsilon_{22}\varepsilon_{33}$$

$$+ \frac{f_5}{2}((\varepsilon_{12} + \varepsilon_{21})^2 + (\varepsilon_{13} + \varepsilon_{31})^2) + \frac{f_6}{2}(\varepsilon_{23} + \varepsilon_{32})^2)P_1^2$$

$$+ (\frac{f_1}{2}\varepsilon_{22}{}^2 + \frac{f_2}{2}(\varepsilon_{11} + \varepsilon_{33})^2 + f_3(\varepsilon_{11}\varepsilon_{22} + \varepsilon_{22}\varepsilon_{33}) + f_4\varepsilon_{11}\varepsilon_{33}$$

$$+ \frac{f_5}{2}((\varepsilon_{12} + \varepsilon_{21})^2 + (\varepsilon_{23} + \varepsilon_{32})^2) + \frac{f_6}{2}(\varepsilon_{13} + \varepsilon_{31})^2)P_2^2$$

$$+ (\frac{f_1}{2}\varepsilon_{33}{}^2 + \frac{f_2}{2}(\varepsilon_{11} + \varepsilon_{22})^2 + f_3(\varepsilon_{11}\varepsilon_{33} + \varepsilon_{22}\varepsilon_{33}) + f_4\varepsilon_{11}\varepsilon_{22}$$

$$+ \frac{f_5}{2}((\varepsilon_{13} + \varepsilon_{31})^2 + (\varepsilon_{23} + \varepsilon_{32})^2) + \frac{f_6}{2}(\varepsilon_{12} + \varepsilon_{21})^2)P_3^2$$

$$+ (\frac{g_1}{4}\varepsilon_{11} + \frac{g_2}{4}(\varepsilon_{22} + \varepsilon_{33}))P_1^4 + (\frac{g_1}{4}\varepsilon_{22} + \frac{g_2}{4}(\varepsilon_{11} + \varepsilon_{33}))P_2^4$$

$$+ (\frac{g_1}{4}\varepsilon_{33} + \frac{g_2}{4}(\varepsilon_{11} + \varepsilon_{22}))P_3^4 + \frac{g_3}{4}(\varepsilon_{12} + \varepsilon_{21})(P_1 P_2^3 + P_2 P_1^3)$$

$$+ \frac{g_3}{4}(\varepsilon_{13} + \varepsilon_{31})(P_1 P_3^3 + P_3 P_1^3) + \frac{g_3}{4}(\varepsilon_{23} + \varepsilon_{32})(P_2 P_3^3 + P_2 P_1^3)$$

$$+ \frac{1}{2\kappa_0}((D_1 - P_1)^2 + (D_2 - P_2)^2 + (D_3 - P_3)^2) \tag{B.1}$$

123

The properties of mono-domain single crystal barium titanate ($BaTiO_3$) have been measured by Li et al. (Li et al.,1991) at room temperature (~22 °C). For a domain with spontaneous polarization in the x_3 direction, the spontaneous polarization and strain rate is:

$$P_3^s = 0.26 \text{ C/m}^2, P_1^s = P_2^s = 0, \ \varepsilon_{33}^s = 0.0082,$$
$$\varepsilon_{11}^s = \varepsilon_{22}^s = -0.0027, \varepsilon_{12}^s = \varepsilon_{21}^s = \varepsilon_{23}^s = 0.$$

In the same coordinate system, the elastic, piezoelectric, and dielectric properties given in standard Voigt notation are:

$$s_{11}^E = 8.01 \times 10^{-12} \text{ m}^2/\text{N}, \ s_{12}^E = -1.57 \times 10^{-12} \text{ m}^2/\text{N}, \ s_{13}^E = -4.6 \times 10^{-12} \text{ m}^2/\text{N},$$
$$s_{33}^E = 12.8 \times 10^{-12} \text{ m}^2/\text{N}, \ s_{12}^E = 17.8 \times 10^{-12} \text{ m}^2/\text{N}, \ s_{13}^E = 7.91 \times 10^{-12} \text{ m}^2/\text{N},$$
$$d_{33} = 106 \times 10^{-12} \text{ C/N}, \ d_{31} = -50 \times 10^{-12} \text{ C/N}, \ d_{15} = 580 \times 10^{-12} \text{ C/N},$$
$$\kappa_{11}^\sigma = 4100\kappa_0 = 36.3 \times 10^{-9} \text{ V m/C}, \ \kappa_{33}^\sigma = 160\kappa_0 = 1.42 \times 10^{-9} \text{ V m/C},$$
$$\kappa_0 = 8.854 \times 10^{-12} \text{ V m/C}.$$

where κ_0 is the dielectric permittivity of free space.

Therefore, the permittivities at constant stress presented above are calculated accordingly. In order to fit these properties of a mono-domain the coefficients of the Helmholtz free energy are chosen as follows:

$$a_1 = -0.668325 E_0 / P_0, \quad a_2 = -3.80653 E_0 / P_0{}^3, \quad a_3 = 0.789223 E_0 / P_0{}^3,$$

$$a_4 = 12.4421 E_0 / P_0{}^5, \quad a_6 = 0.134226 E_0 / P_0{}^5,$$

$$b_1 = 2.54138 E_0 / \varepsilon_0 P_0, \quad b_2 = 1.74267 E_0 / \varepsilon_0 P_0, \quad b_3 = 0.399353 E_0 / \varepsilon_0 P_0,$$

$$c_1 = 2.04999 \sigma_0 / \varepsilon_0, \quad c_2 = 0.971673 \sigma_0 / \varepsilon_0, \quad c_3 = 1.27976 \sigma_0 / \varepsilon_0,$$

$$f_1 = 0.663581 E_0 / \varepsilon_0{}^2 P_0, \quad f_2 = 0.841326 E_0 / \varepsilon_0{}^2 P_0, \quad f_3 = -0.170635 E_0 / \varepsilon_0{}^2 P_0,$$

$$f_4 = 0.687281 E_0 / \varepsilon_0{}^2 P_0, \quad f_5 = 0.106647 E_0 / \varepsilon_0{}^2 P_0, \quad f_6 = 0.2132841 E_0 / \varepsilon_0{}^2 P_0,$$

$$g_1 = -3.66149 E_0 / \varepsilon_0{}^2 P_0{}^3, \quad g_2 = 6.274239 E_0 / \varepsilon_0{}^2 P_0{}^3, \quad g_3 = -1.21644 E_0 / \varepsilon_0{}^2 P_0{}^3.$$

where

$$P_0 = 0.26 \ \text{C/m}^2, \quad \varepsilon_0 = 0.0082, \quad E_0 = 2.18247 \times 10^7 \ \text{V/m}, \text{ and } \sigma_0 = E_0 P_0 / \varepsilon_0 = 692 \times 10^6 \ \text{N/m}^2.$$

The definition of P_0, ε_0 arise from the spontaneous state. And the critical electric field E_0 is the magnitude of the electric field required to cause homogeneous 180° switching when the electric field is applied in the opposite direction of the uniform spontaneous polarization. Finally, the stress σ_0 is a derived quantity used for normalizations.

The parameter a_0 appearing in the Equation (B.1) determines the domain wall thickness. If $a_0 = 1 \times 10^{-10} \ \text{V m}^3/\text{C}$, then $l_0 = 1 \text{nm}$, and therefore the 180° domain wall has thickness equal to 2 nm which is in general agreement with experiment observations (Zhang et al., 1992).

Appendix C: Stroh Formalism in Piezoelectrics

The stroh solution is a compact, complex variable representation for generalized plane strain problem.   Here we will investigate two-dimensional (independent of the x_3 direction, $\varepsilon_{33} = E_3 = 0$) problems in homogenous, linear, piezoelectric materials with no body forces or charges (Landis, 2008).   The governing equations for this two-dimensional problem are:

$$E_1 = -\phi_{,1} \quad \text{and} \quad E_2 = -\phi_{,2} \tag{C.1.a}$$

$$\varepsilon_{11} = u_{1,1} \, , \, \varepsilon_{22} = u_{2,2} \, , \, 2\varepsilon_{12} = u_{1,2} + u_{2,1} \, , \, 2\varepsilon_{31} = u_{3,1} \quad \text{and} \quad 2\varepsilon_{32} = u_{3,2} \tag{C.1.b}$$

$$D_{1,1} + D_{2,2} = 0 \tag{C.1.c}$$

$$\sigma_{11,1} + \sigma_{21,2} = 0, \, \sigma_{12,1} + \sigma_{22,2} = 0, \quad \text{and} \quad \sigma_{31,1} + \sigma_{32,2} = 0 \quad with \quad \sigma_{ij} = \sigma_{ji} \tag{C.1.d}$$

Standard index notation is used with summation implied over repeated indices, and $,j$ represents partial differentiation with respect to the x_j coordinate direction.

Ultimately, we will state the equilibrium equations in terms of mechanical displacements u_i and the electric potential ϕ, so we need the stresses σ_{ij} and electric displacements D_i in terms of the strain ε_{ij} and electric field E_i from the constitutive response, then the stresses and electric displacements can be written in terms of the displacement and potential, and finally these relationships will be placed into the equilibrium and Gauss' law to get three governing partial differential equations for the displacements and potential.

In Appendix A, we have the formula (A.2), and use the (C.1.a) & (C.1.b), assuming the generalized plane strain and electric field conditions, then

$$\left.\begin{array}{l}\sigma_{ij}=c^{E}_{ijkl}\varepsilon_{kl}-e_{kij}E_{k}\\ D_{i}=e_{ikl}\varepsilon_{kl}+\kappa^{\varepsilon}_{ij}E_{j}\end{array}\right\}\Rightarrow\begin{bmatrix}c^{E}_{i\delta j\gamma}&e_{\gamma i\delta}\\ e_{\delta j\gamma}&-\kappa^{\varepsilon}_{\delta\gamma}\end{bmatrix}\begin{pmatrix}u_{j}\\ \phi\end{pmatrix}_{,\gamma\delta}=0 \tag{C.2}$$

where the Greek subscripts are only allowed to take on the values 1 and 2, and summation over repeated indices is still assumed. The constants c^{E}, e and κ^{ε} in (C.2) can be obtaining by manipulating (A.1) and (A.2), since the material properties in (A.1) are given in Appendix B.

To solve these equations in (C.2), we assume a solution of the form,

$$\begin{pmatrix}u_{i}\\ \phi\end{pmatrix}=\begin{pmatrix}a_{i}\\ a_{4}\end{pmatrix}f(z)=\mathbf{a}f(z) \tag{C.3}$$

where $z=x_{1}+px_{2}$ is a complex variable (p is complex with generally both real and imaginary parts). Therefore, (C.2) becomes an eigenvalue problem with p as the eigenvalues and $\mathbf{a}$ as the eigenvectors, and our characteristic equation can be written as,

$$\left\{\mathbf{Q}+p(\mathbf{R}+\mathbf{R}^{T})+p^{2}\mathbf{T}\right\}\mathbf{a}=0 \tag{C.4}$$

Using standard Voigt notation,

$$\mathbf{Q}=\begin{bmatrix}c_{11}&c_{16}&c_{15}&e_{11}\\ c_{16}&c_{66}&c_{56}&e_{16}\\ c_{15}&c_{56}&c_{55}&e_{15}\\ e_{11}&e_{16}&e_{15}&-\kappa_{11}\end{bmatrix},\ \mathbf{R}=\begin{bmatrix}c_{16}&c_{12}&c_{14}&e_{21}\\ c_{66}&c_{26}&c_{46}&e_{26}\\ c_{56}&c_{25}&c_{45}&e_{25}\\ e_{16}&e_{12}&e_{14}&-\kappa_{12}\end{bmatrix},\ \mathbf{T}=\begin{bmatrix}c_{66}&c_{26}&c_{46}&e_{26}\\ c_{26}&c_{22}&c_{24}&e_{22}\\ c_{46}&c_{24}&c_{44}&e_{24}\\ e_{26}&e_{22}&e_{24}&-\kappa_{22}\end{bmatrix} \tag{C.5}$$

Non-trivial solutions to the characteristic equation exist when the determinant of the bracketed matrix is zero.

$$\det\{\mathbf{Q} + p(\mathbf{R} + \mathbf{R}^T) + p^2\mathbf{T}\} = 0 \tag{C.6}$$

This represents an eighth order polynomial for p. It is possible to show that for a material with physically admissible p is always complex. Since the coefficients of the eighth order polynomial are real, the roots appear as complex conjugate pairs. Without loss of generality, we can take,

$$p_5 = \bar{p}_1, \; p_6 = \bar{p}_2, \; p_7 = \bar{p}_3, \; p_8 = \bar{p}_4$$

where $z_I = x + p_I y$, the general solution has the form,

$$\begin{pmatrix} u_i \\ \phi \end{pmatrix} = \sum_{J=1}^{8} \begin{pmatrix} A_{iJ} \\ A_{4J} \end{pmatrix} f_J(z_J) \tag{C.7}$$

For each eigenvalue p_J there is an associated eigenvector (A_{iJ}, A_{4J}). The matrix A is assembled by placing the components of the eigenvectors **a** in the columns.

Mode I: Mode II: Mode III:
Opening   In-plane shear   Out-of-plane shear
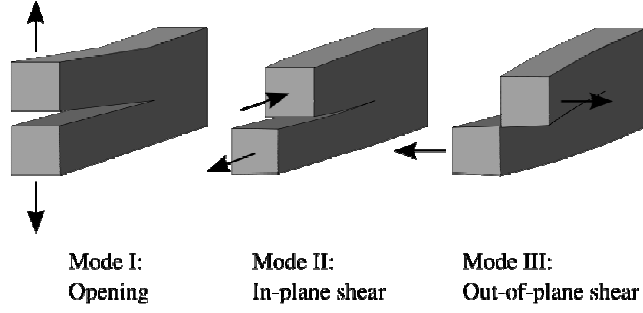
Figure C.1:   A schematic of the crack under mode I, II and III loadings.

Define

$$b_i = c^E_{i2j1}a_j + e_{1i2}a_4 + pc^E_{i2j2}a_j + pe_{2i2}a_4$$
$$b_4 = e_{2i1}a_j - \kappa^\varepsilon_{21}a_4 + pe_{2j2}a_j - p\kappa^\varepsilon_{22}a_4$$

(C.8)

It is possible to write the stresses and electric displacements in vector form as,

$$\begin{pmatrix} \sigma_{i2} \\ D_2 \end{pmatrix} = 2\,\mathrm{Re}\sum_{j=1}^{4}\begin{pmatrix} B_{iJ} \\ B_{4J} \end{pmatrix}f'_J(z_J)$$
$$\begin{pmatrix} \sigma_{i1} \\ D_1 \end{pmatrix} = -2\,\mathrm{Re}\sum_{j=1}^{4}\begin{pmatrix} B_{iJ} \\ B_{4J} \end{pmatrix}p_J f'_J(z_J)$$

(C.9)

The matrix **B** is assembled by placing **b** vectors in the columns. Note that the stress and electric displacement can be derived from a set of stress and electric displacement potential functions as,

$$\begin{pmatrix} \sigma_{i2} \\ D_2 \end{pmatrix} = \begin{pmatrix} \psi_{i,1} \\ \psi_{4,1} \end{pmatrix}, \quad \begin{pmatrix} \sigma_{i1} \\ D_1 \end{pmatrix} = -\begin{pmatrix} \psi_{i,2} \\ \psi_{4,2} \end{pmatrix}$$

(C.10)

The potential functions can then be given in terms of the complex functions as,

129

$$\begin{pmatrix} \psi_i \\ \psi_4 \end{pmatrix} = 2\,\mathrm{Re}\sum_{J=1}^{4}\begin{pmatrix} B_{iJ} \\ B_{4J} \end{pmatrix} f_J(z_J) \tag{C.11}$$

Now take the case of a semi-infinite crack with traction-free and charge-free boundaries. On the plane ahead of the crack tip, $\theta = 0$, and $z_I = x_1 = r$, where r, θ are defined through $z_I = x_1 + p_I x_2 = r_I e^{i\theta_I}$, we have

$$\begin{pmatrix} \sigma_{i2} \\ D_2 \end{pmatrix} = \frac{1}{2\sqrt{r}}\sum_{J=1}^{4}\begin{pmatrix} B_{iJ} + \overline{B}_{iJ} \\ B_{4J} + \overline{B}_{4J} \end{pmatrix} \equiv \frac{1}{\sqrt{2\pi r}}\begin{pmatrix} K_I \\ K_{II} \\ K_{III} \\ K_{IV} \end{pmatrix} \tag{C.12}$$

The definition in (C.12) states that the stress or electric displacement ahead of the crack tip is equal to its corresponding intensity factor K by the square root of $2\pi r$. Here, K_I, K_{II}, K_{III} are the opening loads, in-plane shear loads, and out-of-plane shear loads intensity factors respectively as shown in Figure C.1, and K_{IV} is the electric loading intensity factor which can also be written as K_D. Using this convention and our previous conclusion, we can show,

$$\sum_{J=1}^{4}\begin{pmatrix} B_{iJ} \\ B_{4J} \end{pmatrix} = \begin{bmatrix} B_{11} & B_{12} & B_{13} & B_{14} \\ B_{21} & B_{22} & B_{23} & B_{24} \\ B_{31} & B_{32} & B_{33} & B_{34} \\ B_{41} & B_{42} & B_{43} & B_{44} \end{bmatrix}\begin{pmatrix} 1 \\ 1 \\ 1 \\ 1 \end{pmatrix} = \frac{1}{\sqrt{2\pi}}\begin{pmatrix} K_{II} \\ K_I \\ K_{III} \\ K_{IV} \end{pmatrix} \tag{C.13}$$

Finally, our solutions for the stress and electric displacement potentials and the displacements & electric potential are,

130

$$\begin{pmatrix} \psi_i \\ \psi_4 \end{pmatrix} = 2 \operatorname{Re} \sum_{J=1}^{4} \begin{pmatrix} B_{iJ} \\ B_{4J} \end{pmatrix} \sqrt{z_J} \quad \text{and} \quad \begin{pmatrix} u_i \\ \phi \end{pmatrix} = 2 \operatorname{Re} \sum_{J=1}^{4} \begin{pmatrix} A_{iJ} \\ A_{4J} \end{pmatrix} \sqrt{z_J} \quad (C.14)$$

where

$$(A)_I = (\mathbf{R}^T + p_I \mathbf{T})^{-1} (\mathbf{B})_I$$

and I denotes the Ith column.

The energy release rate associated with an incremental advance of the crack tip can be computed using a crack closure integral,

$$G \delta a = \frac{1}{2} \int_0^{\delta a} \begin{pmatrix} \sigma_{i2}(r) \\ D_2(r) \end{pmatrix}^T \cdot \begin{pmatrix} \Delta u_i(r - \delta a) \\ \Delta \phi(r - \delta a) \end{pmatrix} dr \quad (C.15)$$

where Δu_i and $\Delta \phi$ are the crack opening/sliding displacements and potential jump. The two vectors appearing in the integrand are given as,

$$\begin{pmatrix} \sigma_{12} \\ \sigma_{22} \\ \sigma_{32} \\ D_2 \end{pmatrix} = \frac{1}{\sqrt{2\pi x_1}} \begin{pmatrix} K_{II} \\ K_{I} \\ K_{III} \\ K_{IV} \end{pmatrix} \quad (C.16.a)$$

and

$$\begin{pmatrix} \Delta u_1 \\ \Delta u_2 \\ \Delta u_3 \\ \Delta \phi \end{pmatrix} = 2 \operatorname{Re} \left\{ i \mathbf{A} \mathbf{B}^{-1} \mathbf{B} \cdot \begin{pmatrix} \sqrt{r} \\ \sqrt{r} \\ \sqrt{r} \\ \sqrt{r} \end{pmatrix} \right\} = \underbrace{2 \operatorname{Re}\{i \mathbf{A} \mathbf{B}^{-1}\}}_{\mathbf{H}} \cdot \underbrace{2 \operatorname{Re}\{\mathbf{B}\} \cdot \begin{pmatrix} \sqrt{r} \\ \sqrt{r} \\ \sqrt{r} \\ \sqrt{r} \end{pmatrix}}_{\sqrt{\frac{2r}{\pi}}(K_{II}\ K_{I}\ K_{III}\ K_{IV})^T} = \sqrt{\frac{2r}{\pi}} \mathbf{H} \begin{pmatrix} K_{II} \\ K_{I} \\ K_{III} \\ K_{IV} \end{pmatrix}$$

$$(C.16.b)$$

From (C.15), the closure integral becomes,

$$G = \frac{1}{2\pi\delta a}(K_{II} \quad K_I \quad K_{III} \quad K_{IV}) \bullet \mathbf{H} \bullet \begin{pmatrix} K_{II} \\ K_I \\ K_{III} \\ K_{IV} \end{pmatrix} \int_0^{\delta a} \frac{\sqrt{\delta a - r}}{\sqrt{r}} dr$$

$$= \frac{1}{4}(K_{II} \quad K_I \quad K_{III} \quad K_{IV}) \bullet \mathbf{H} \bullet \begin{pmatrix} K_{II} \\ K_I \\ K_{III} \\ K_{IV} \end{pmatrix}$$

(C.17)

Appendix D: Model of Dielectric Elastomers with Electric Polarization

In this appendix, the form of free energy in the hyperelastic models not only depend on the mechanical displacement and electric field, but also on electric polarization.

(a) Reference State   (b) Current State
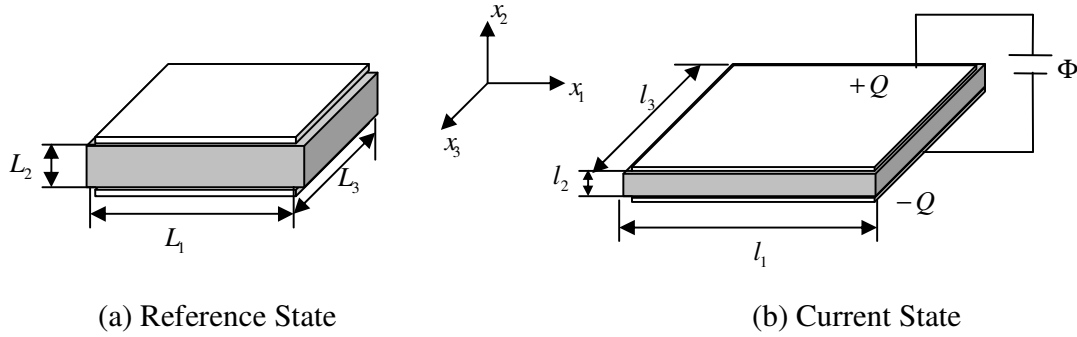
Figure D.1:   A schematic plot of a dielectric elastomer with the dimension $L_1 \times L_2 \times L_3$ at (a) the reference state and with the dimension $l_1 \times l_2 \times l_3$ at (b) the deformed or current state.

Figure D.1 shows a schematic plot of dielectric elastomer with the dimension $L_1 \times L_2 \times L_3$ at (a) the reference state and with the dimension $l_1 \times l_2 \times l_3$ at (b) the deformed or current state. The stretches $\lambda_1, \lambda_2, \lambda_3$ are defined by $\lambda_1 = l_1 / L_1$, $\lambda_2 = l_2 / L_2$, and $\lambda_3 = l_3 / L_3$ respectively.   Suppose P_1, P_2, P_3 are the normal forces in the x_1, x_2, x_3 directions, then the nominal stresses are defined by $s_1 = P_1 / L_2 L_3$, $s_2 = P_2 / L_3 L_1$, and $s_3 = P_3 / L_1 L_2$.

The general form of free energy can be taken as

$$
\begin{aligned}
W &= W(\lambda_1, \lambda_2, \lambda_3, E) \\
&= W_s(\lambda_1, \lambda_2, \lambda_3) + \frac{1}{2} a \tilde{P}_I^2 - \frac{\kappa_{mat}}{2} J F_{Ji}^{-1} F_{Ki}^{-1} \tilde{E}_J \tilde{E}_K - J F_{Ji}^{-1} F_{Ki}^{-1} \overline{E}_J \tilde{P}_K \\
&= W_s(\lambda_1, \lambda_2, \lambda_3) + \frac{1}{2} a (p_k F_{kI})(p_j F_{jI}) - \frac{\kappa_{mat}}{2} J F_{Ji}^{-1} F_{Ki}^{-1} \tilde{E}_J \tilde{E}_K - J F_{Ji}^{-1} F_{Ki}^{-1} \tilde{E}_J (p_l F_{lK}) \\
&= W_s(\lambda_1, \lambda_2, \lambda_3) + \frac{1}{2} a (p_k F_{kI})(p_j F_{jI}) - \frac{\kappa_{mat}}{2} J C_{JK}^{-1} \tilde{E}_J \tilde{E}_K - J C_{JK}^{-1} \tilde{E}_J (p_l F_{lK})
\end{aligned}
$$

$$(D.1)$$

And the nominal stresses can be written as

$$
s_I = \frac{\partial W}{\partial \lambda_I} \tag{D.2}
$$

where $W_s(\lambda_1, \lambda_2, \lambda_3)$ is the energy due to stretch and different for different hyperelastic models, κ_{mat} electrical permittivity of the material, J determinant of gradient deformation tensor, $\tilde{\mathbf{E}}$ electric field in reference state, $\mathbf{P}$ electric polarization in current state, $\tilde{\mathbf{P}}$ electric polarization in reference state, $\mathbf{F}$ deformation gradient tensor, $\mathbf{F}^{-1}$ inverse of deformation gradient tensor and $\mathbf{C}^{-1}$ the inverse of right Cauchy-Green deformation tensor.

With the assumption of generalized plane strain, $\lambda_3 = 1$. For the electric potential loads on the top and bottom surfaces in x_2 direction, the electric field in reference state is $\tilde{E}_I = -\delta_{I2} \frac{\phi}{L_2}$. And the deformation gradient tensors can be written as the functions of the stretches,

$$
\mathbf{F} = \begin{bmatrix} \lambda_1 & 0 & 0 \\ 0 & \lambda_2 & 0 \\ 0 & 0 & 1 \end{bmatrix} \Rightarrow \mathbf{F}^{-1} = \begin{bmatrix} 1/\lambda_1 & 0 & 0 \\ 0 & 1/\lambda_2 & 0 \\ 0 & 0 & 1 \end{bmatrix}
$$

134

The Jacobian determinant $J = \lambda_1 \lambda_2 \lambda_3 = \lambda_1 \lambda_2$. The electric polarizations in the reference state $\tilde{P}_1 = \tilde{P}_3 = 0$. Suppose $\tilde{P}_2 = P$, the energy form reduces to

$$W = W_s(\lambda_1, \lambda_2, 1) + \frac{1}{2} a\lambda_2 P^2 - \frac{\kappa}{2} \frac{\lambda_1}{\lambda_2} \left(\frac{\phi}{L_2} \right)^2 + \lambda_1 \frac{\phi}{L_2} P \qquad (D.3)$$

The electric polarization in equilibrium state can be found from

$$\frac{\partial W}{\partial \lambda_1} = \frac{\partial W}{\partial \lambda_2} = \frac{\partial W}{\partial P} = 0 \qquad (D.4)$$

Solving the set of three equations, the electric polarization at equilibrium is

$$\frac{\partial W}{\partial P} = 0 \implies P = -\frac{\lambda_1}{a\lambda_2^2} \frac{\phi}{L_2} \quad \text{(Analytical)} \qquad (D.5)$$

And λ_1, λ_2 can be derived from $s_1 = \dfrac{\partial W}{\partial \lambda_1} = 0$, $s_2 = \dfrac{\partial W}{\partial \lambda_2} = 0$, depending on different hyperelastic models such as the Neo-Hookean and the Gent models.

For the Neo-Hookean model,

$$W_s = \frac{\mu}{2}(I_1^C J^{-2/3} - 3) + \frac{K}{2}(J - 1)^2 \qquad (D.6)$$

With the different value of the applied electric potential, the numerical calculated electric polarization is compared with the analytic result in (D.5), as shown in Figure D.2.
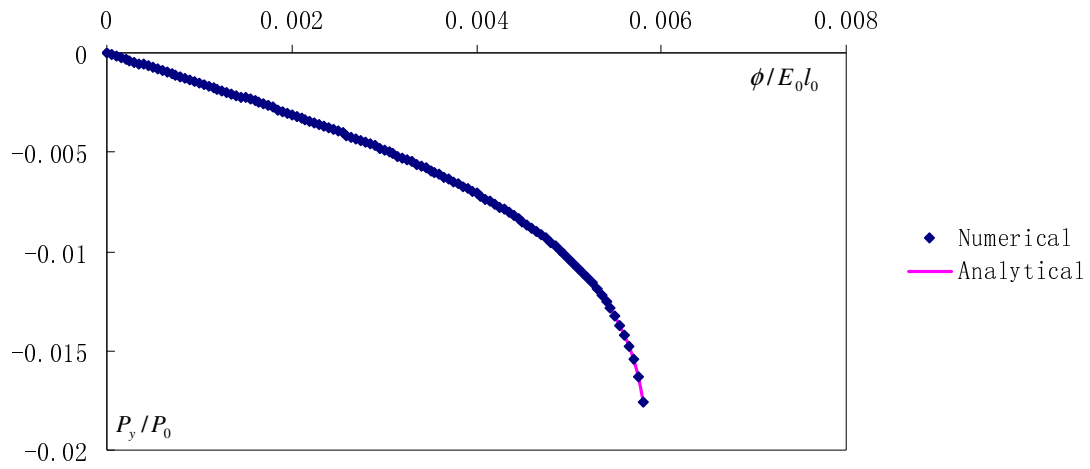
Figure D.2: With the different value of the applied electric potential, the numerical calculated electric polarization is compared with the analytic result. The x-axis represents the normalized electric potential and the y-axis represents the normalized y-component of polarization.

The material properties used here are

$$a = -0.668325 E_0 / P_0,$$

$$E_0 = 2.18247 \times 10^7 \text{ V/m}, \ P_0 = 0.26 \text{ C/m}^2$$

$$\mu = 1.5 \times 10^3 \text{ N/m}^2, \ K = 10^9 \text{ N/m}^2$$

References

H. Allik, and T. J. R. Hughes, 1970. "Finite Element Method for Piezoelectric Vibration", International Journal for Numerical Methods in Engineering, 2, 151-157.

L. Belliache, A. Garcia, and D. Vanderbilt, 2000. "Finite-temperature Properties of $Pb(Zr_{1-x}Ti_x)O_3$ Alloys from First Principles", Physics Review Letters, 84, 5427-5430.

K. Bertoldi, and M. C. Boyce, 2008. "Wave Propagation and Instabilities in Monolithic and Periodically Structured Elastomeric Materials Undergoing Large Deformations", Physical Review B, 78, 184107.

R. C. Buchanan, 1986. "Ceramic Materials for Electronics – Processing, Properties, and Applications", Marcel Dekker, New York.

F. Carpi, D. D. Rossi, R. Kornbluh, R. Pelrine, and P. Sommer-Larsen, 2008. "Dielectric Elastomers as Electromechanical Transducers: Fundamentals, Materials, Devices, Models and Applications of an Emerging Electroactive Polymer Technology", Elsevier.

K. H. Chan and N. W. Hagood, 1994. "Modeling of Nonlinear Piezoceramics for Structural Actuation", Proceedings of SPIE, Smart Structural Materials, 2190, 194.

W. Chen and C. S. Lynch, 1998. "A Micro-electro-mechanical Model for Polarization Switching of Ferroelectric Materials", Acta Materialia, 46, 5303-5331.

R. E. Cohen and H. Krakauer, 1992. "Electronic Structure Studies of Differences in Ferroelectric Behavior of $BaTiO_3$ and $PbTiO_3$", Ferroelectrics, 136, 65-83.

W. F. Deeg, 1980. "The Analysis of Dislocation, Crack and Inclusion Problems in Piezoelectric Solids", Ph.D. Thesis, Stanford University.

A. F. Devonshire, 1954. "Theory of Ferroelectrics", Philosophical Magazine Supplement, 3, 85.

M. L. Dunn, 1994. "The Effects of Crack Face Boundary Conditions on the Fracture Mechanics of Piezoelectric Solids", Engineering Fracture Mechanics, 48, 25-29.

E. Fried, and M. E. Gurtin, 1993. "Continuum Theory of Thermally Induced Phase Transitions Based on an Order Parameter", Physica D, 68, 326-343.

E. Fried, and M. E. Gurtin, 1994. "Dynamic Solid-solid Transitions with Phase Characterized by an Order Parameter", Physica D, 72, 287-308.

M. E. Gurtin, 1996. "Generalized Ginzburg-Laudau and Cahn-Hilliard Equations Based on a Microforce Balance", Physica D, 92, 178-192.

137

T. H. Hao, and Z. Y. Shen, 1994. "A New Electric Boundary Condition of Electric Fracture Mechanics and Its Application", Engineering Fracture Mechanics, 47, 793-802.

J. E. Huber, N. A. Fleck, C. M. Landis and R. M. McMeeking, 1999. "A Constitutive Model for Ferroelectric Polycrystals", Journal of the Mechanics and Physics of Solids, 47, 1663-1697.

S. C. Hwang, C. S. Lynch, and R. M. McMeeking, 1995. "Ferroelectric/ferroelastic Interactions and a Polarization Switching Model", Acta Metallurgica et Materialia, 43, 2073-2084.

S. C. Hwang, J. E. Huber, R. M. McMeeking, and N. A. Fleck, 1998. "The Simulation of Switching in Polycrystalline Ferroelectric Ceramics", Journal of Applied Physics, 84, 1530-1540.

T. Ikeda, "Fundamentals of Piezoelectricity", 1990. Oxford University Press, Oxford.

Q. Jiang, 1994. "The Driving Traction Acting on a Surface Discontinuity within a Continuum in the Presence of Electromagnetic Fields", Journal of Elasticity, 34, 1-21.

F. Jona and G. Shirane, 1962. "Ferroelectric Crystals", Pergamon Press, New York.

M. Kaltenbacher and B. Kaltenbacher, 2011. "Modeling and Numerical Simulation of Ferroelectric Material Behavior Using Hysteresis Operators", Ferroelectrics-Characterization and Modeling, http://www.intechopen.com, 28, 561-586.

M. Kamlah and C. Tsakmakis, 1999. "Phenomenological Modeling of the Non-linear Electromechanical Coupling in Ferroelectrics", International Journal of Solids and Structures, 36, 669-695.

M. Kamlah and Q. Jiang, 1999. "A Constitutive Model for Ferroelectric PZT Ceramics under Uniaxial Loading", Smart Materials and Structures, 8, 441-459.

M. Kamlah, 2001. "Ferroelectric and Ferroelastic Piezoceramics-Modeling of Electromechanical Hysteresis Phenomena", Continuum Mechanics and Thermodynamics, 13, 219-268.

C. M. Landis, 2002a. "Fully Couple, Multi-axial, Symmetric Constitutive Laws for Polycrystalline Ferroelectric Ceramics", Journal of the Mechanics and Physics of Solids, 50, 127-152.

C. M. Landis, 2002b. "A New Finite-element Formulation for Electromechanical Boundary Value Problems", International Journal for Numerical Methods in Engineering, 55, 613-628.

C. M. Landis, 2003. "On the Strain Saturation Conditions for Polycrystalline Ferroelastic Materials", Journal of Applied Mechanics, 70, 470-478.

C. M. Landis, 2004a. "In-plane Complex Potentials for a Special Class of Materials with Degenerate Piezoelectric Properties", International Journal of Solids and Structures, 41, 695-715.

C. M. Landis, 2004b. "Energetically Consistent Boundary Conditions for Electromechanical Fracture", International Journal of Solids and Structures, 41, 6291-6315.

C. M. Landis, J. Wang, and J. Sheng, 2004c. "Micro-electromechanical determination of the possible remanent strain and polarization stats in polycrystalline ferroelectrics and the implications for phenomenological constitutive theories", Journal of ntelligent Material Systems and Structure, 15, 513-525.

C. M. Landis, 2008. "Mechanics of Active Materials", Class notes. http://www.ae.utexas.edu/~landis/Landis/Teaching.html.

W. Li, 2006. "On the Crack Face Boundary Conditions in Electromechanical Fracture and An Experimental Protocol for Determining Energy Release Rates", Master thesis, Rice University.

W. Li, R. M. McMeeking and C. M. Landis, 2008. "On the Crack Face Boundary Conditions in Electromechanical Fracture and An Experimental Protocol for Determining Energy Release Rates", European Journal of Mechanics A/Solids, 27, 285-301.

W. Li and C. M. Landis, 2011. "Nucleation and Growth of Domains Near Crack Tips in Single Crystal Ferroelectrics", Engineering Fracture Mechanics, 78, 1505-1513.

Z. Li, S. K. Chan, M. H. Grimsditch, and E. S. Zouboulis, 1991. "The Elastic and Electromechanical Properties of Tetragonal $BaTiO_3$ Single Crystals", Journal of Applied Physics, 70, 7327-7332.

M. E. Lines and A. M. Glass, 1977. "Principles and Applications of Ferroelectric and Related Materials", Oxford University Press, Oxford.

R. E. Loge, and Z. Suo, 1996. "Nonequilibrium Thermodynamics of Ferroelectric Domain Evolution", Acta Materialia, 44, 3429-3438.

R. M. McMeeking, 1999. "Crack Tip Energy Release Rate for a Piezoelectric Compact Tension Specimen", Engineering Fracture Mechanics, 64, 217-244.

R. M. McMeeking, 2004. "The Energy Release Rate for a Griffith Crack in a Piezoelectric Material", Engineering Fracture Mechanics, 71, 1169-1183.

R. M. McMeeking, and C. M. Landis, 2005. "Electrostatic Forces and Stored Energy for Deformable Dielectric Materials", Journal of Applied Mechanics, 72, 581-590.

A. Mielke and A. M. Timofte, 2006. "Modeling and Analytical Study for Ferroelectric Materials", Mechanics of Advanced Materials and Structures, 13, 457-462.

Y. Motola, and L. Banks-Sills, 2009. "M-Integral for Calculating Intensity Factors of Cracked Piezoelectric Materials Using the Exact Boundary Conditions", Journal of Applied Mechanics, 76, 011004.

Y. Motola, L. Banks-Sills, and V. Fourman, 2009. "Fracture Testing of Piezoelectric Ceramics", International Journal of Fracture, 159, 167-190.

S. Nezamabadi, H. Zahrouni, J. Yvoonet, 2011. "Solving Hyperelastic Material Problems by Asymptotic Numerical Method", Computational Mechanics, 47, 77-92.

J. F. Nye, 1957. "Physical Properties of Crystals", Oxford University Press, Great Britain.

W. S. Oates, 2005. "Heterogeneity influence on electric field induced piezoelectric microfracture", Journal of ntelligent Material Systems and Structure, 16, 733-741.

Y. E. Pak, 1992. "Linear Electro-elastic Fracture Mechanics of Piezoelectric Materials", International Journal of Fracture, 54, 79-100.

V. Z. Parton, 1976. "Fracture Mechanics of Piezoelectric Materials", Acta Astronaut, 3, 671-683.

J. S. Plante, and S. Dubowsky, 2006. "Large-scale Failure Modes of Dielectric Elastomer Acutators", International Journal of Solids and Structures, 43, 7727-7751.

J. Sheng, 2003. "Polarization Saturation Simulation of Ferroelectric Polycrystals", Master Thesis, Rice University.

Y. H. Shin, L. Grinberg, I. W. Chen, and A. M. Rappe, 2007. "Nucleation and Growth Mechanism of Ferroelectric Domain-Wall Motion", Nature, 449, 881-886.

A. S. Sidorkin, 2006. "Domain Structure in Ferroelectrics and Related Materials", Cambridge International Science Publishing, Cambridge.

H. A. Sosa, 1992. "On the Fracture Mechanics of Piezoelectric Solids", International Journal of Solids and Structures", 29, 2613-2622.

Y. Su and C. M. Landis, 2007. "Continuum Thermodynamics of Ferroelectric Domain Evolution: Theory, Finite Element Implementation, and Application to Domain Wall Pinning", Journal of the Mechanics and Physics of Solids, 55, 280-305.

Z. Suo, C. M. Kuo, D. M. Barnett, and J. R. Willis, 1992. "Fracture Mechanics for Piezoelectric Ceramics", Journal of the Mechanics and Physics of Solids, 40, 739-765.

Z. Suo, 2010. "Theory of Dielectric Elastomers", Acta Mechanica Solida Sinica, 23, 549-578.

N. Triantafyllidis, M. D. Nestorovic, and M. W. Schraad, 2006. "Failure Surfaces for Finitely Strained Two-phase Periodic Solids under General In-plane Loading", Journal of Applied Mechanics, 73, 505-515.

J. Valasek, 1921. "Piezo-Electric and Allied Phenomena in Rochelle Salt", Physical Review, 17, 475-481.

J. Wang and C. M. Landis, 2004. "On the Fracture Toughness of Ferroelectric Ceramics with Electric Field Applied Parallel to the Crack Front", Acta Materialia, 52, 3435-3446.

J. Wang, 2006. "Fracture Toughening of Ferroelectric Ceramics under Electro-Mechanical Loading", Ph.D. Dissertation, Rice University.

W. L. Warren, D. Dimos, B. A. Tuttle, R. D. Nasby, and G. E. Pike, 1994. "Electronic Domain Pinning in $Pb(Zr_{1-x}Ti_x)O_3$ Thin Films and Its Role in Fatigue", Applied Physics Letters, 65, 1018-1020.

Y. Xiao, V. B. Shenoy, and K. Bhattacharya, 2005. "Depletion Layers and Domain Walls in Semiconducting Ferroelectric Thin Films", Physical Review Letters, 95, 247603.

F. Xu, S. Trolier-McKinstry, W. Ren, B. Xu, Z.-L. Xie, and K. J. Hemker, 2005. "Domain Wall Motion and Its Contribution to the Dielectric and Piezoelectric Properties of Lead Zirconate Titanate Films", Journal of Applies Physics, 89, 1336-1348.

Y. Xu, 1991. "Ferroelectric Materials and Their Applications", Elsevier Science Publishing Company, New York.

X. Zhang, T. Hashimoto, and D. C. Joy, 1992. "Electron Holographic Study of Ferroelectric Domain Walls", Applied Physics Letters, 60, 784-786.

X. H. Zhao, W. Hong, and Z. Suo, "Electromechanical Coexistent States and Hysteresis in Dielectric Elastomers", Physical Review B, 2007, 76, 134113.

M. Zhenyi, J. I. Scheinbeim, J. W. Lee, and B. A. Newman, 1994. "High Field Electrostrictive Response of Polymers", Journal of Polymer Science Part B: Polymer Physics, 32, 2721-2731.

Vita

Wenyuan Li was born in ShanDong province, China in 1982. She graduated from ZaoZhuang 3rd Middle School in 1998. She entered the Department of Mechanics and Mechanical Engineering at the University of Science and Technology of China, and received the degree of Bachelor of Science in May 2003. In December 2006, she received the degree of Master of Science in Mechanical Engineering from Rice University. In January 2007, she entered the graduate school in the Department of Aerospace Engineering and Engineering Mechanics at the University of Texas at Austin. Her research focused on fracture of ferroelectric ceramics, phase-field modeling of ferroelectric domain evolution, and instabilities of dielectric elastomer composites.

Permanent Address: 2501 Lake Austin Blvd., APT G208, Austin, Texas 78703

This manuscript was typed by the author.